CHARACTERIZATION OF COMBUSTION CHAMBER DEPOSITS FORMED DURING HOMOGENEOUS CHARGE COMPRESSION IGNITION AND THE IMPACT OF A THERMAL BARRIER COATING ON DEPOSIT ACCUMULATION AND HCCI OPERABILITY

by

Mark A. Hoffman

A doctoral dissertation submitted in partial fulfillment
of the requirements for the degree of
Doctor of Philosophy
(Mechanical Engineering)
in The University of Michigan
2012

Doctoral Committee:

Professor Zoran S. Filipi, Co-Chair, Clemson University
Associate Professor Claus Borgnakke, Co-Chair
Professor Volker Sick
Assistant Professor Matthias Ihme
Research Scientist David L. Reuss

Al mio amore – per cent’anni

ACKNOWLEDGMENTS

I would like to thank Prof. Zoran Filipi for the guidance he has provided throughout the years. His passion for this project and persistent pursuit of excellence has been inspirational. Additionally, I would like to extend my gratitude to Prof. Claus Borgnakke, Prof. Volker Sick, Prof. Matthias Ihme and Dr. David Reuss for their exceptional feedback.

This work was made possible through the support of General Motors R&D. Not only was the research sponsored by the GM-UM Collaborate Research Laboratory, but the close interactions with Paul Najt, Orgun Güralp, Tang-Wei Kuo and Nicole Wermuth were invaluable.

A special thanks to my team member Ben Lawler for his assistance with the engine experiments. In addition, the many technical discussions with my autolab compatriots, Josh Lacey, Jason Martz, Ashwin Salvi, Luke Hagen, George Lavoie, and John Hoard, have been extremely useful. I would also like to thank the W.E. Lay Autolab community as a whole for the continuous assistance and for adding levity to this journey.

I thank my family for their unwavering support throughout my entire collegiate career. And finally, I must express a special word of appreciation for my wife, Leah. In her I find my passion and my strength. She has been my most profound discovery.

TABLE OF CONTENTS

DEDICATION.. ii

ACKNOWLEDGMENTS iii

LIST OF FIGURES ix

LIST OF TABLES xvi

ABSTRACT.. xvii

CHAPTER 1 INTRODUCTION, MOTIVATION AND OBJECTIVES........ 1

1.1 Homogeneous Charge Compression Ignition Background 2

1.1.1 Benefits of Homogeneous Charge Compression Ignition 3

1.1.2 Detriments of HCCI.. 7

1.1.3 Thermal Influences on Homogeneous Charge Compression Ignition.. 9

1.2 Combustion Chamber Deposit Background... 13

1.2.1 Combustion Chamber Deposit Formation 13

1.2.2 Influence of Combustion Chamber Deposits on Homogeneous Charge Compression Ignition.. 14

1.2.3 Combustion Chamber Deposit Properties... 18

1.3 Thermal Barrier Coatings... 21

1.3.1 Thermal Barrier Coatings Applied to Engines.................................... 22

1.3.2 Determining the Properties of Thermal Barrier Coatings.................. 22

1.3.3 Effects of Morphology on Thermal Properties of Thermal Barrier Coatings 26

1.4 Project Motivation and Objectives 26

1.4.1 Characterization of Combustion Chamber Deposits........................... 27

1.4.2 Assess the Impact of Thermal Barrier Coatings on Combustion Chamber Deposit Accumulation and Homogeneous Charge Compression Ignition Operability 27

CHAPTER 2 HCCI EXPERIMENTAL APPARATUS AND PROCESSING METHODOLOGY 29

2.1 Engine Apparatus 29

2.2 Heat Flux Probes 38

2.3 Deposit Thickness Measurement 39

2.4 Data Acquisition Systems 40

2.4.1 Time Averaged Data 40

2.4.2 Crank Angle Based Data 40

2.5 Heat Release Analysis 41

2.6 Temperature and Heat Flux 43

CHAPTER 3 THE DYNAMIC RADIATION CHAMBER 45

3.1 Radiation Chamber Overview 46

3.2 Improvements to the Radiation Chamber Data Processing 48

3.3 Dynamic Radiation Chamber Accuracy Evaluation 51

3.3.1 The Impact of a Non-Instantaneous Heat Flux Pulse on Ex-Situ Diffusivity 52

3.3.2 Impact of Sample Thickness and Chopping Wheel Speed on Ex-Situ Diffusivity 58

3.3.3 Impact of Radiation Transparency on Ex-Situ Diffusivity 61

3.3.4 Ex-Situ Diffusivity Accuracy with Ceramic Materials 64

3.3.5 Accuracy Evaluation Conclusions 67

CHAPTER 4 THERMAL DIFFUSIVITY OF COMBUSTION CHAMBER DEPOSITS 68

4.1 Analysis of Combustion Chamber Deposit Accumulation 68

4.2 Ex-situ and In-situ Diffusivities of Combustion Chamber Deposits.......... 73

4.2.1 Ex-situ Combustion Chamber Deposit Diffusivity............................. 73

4.2.2 In-Situ Combustion Chamber Deposit Diffusivity 76

4.3 The Effect of Compressed Air on Combustion Chamber Deposit Diffusivity 79

4.4 The Impact of Fuel on Combustion Chamber Deposit Diffusivity............ 82

4.5 The Impact of Heat Transfer Mode on Combustion Chamber Deposit Thermal Diffusivity... 86

4.5.1 Peak Temperature Phase Delay Analysis 86

4.5.2 Partial Transparency of Combustion Chamber Deposits to Radiation Heat Flux.. 88

4.5.3 Penetration of Radiation into the Morphology of Combustion Chamber Deposits... 92

4.6 CCD Diffusivity Conclusions and Contributions....................................... 97

CHAPTER 5 DIFFUSIVITY OF THE MAGNESIUM ZIRCONATE THERMAL BARRIER COATING 100

5.1 Radiation Transparency of the Magnesium Zirconate Coating................ 101

5.2 Removing the Impact of the Nickel Alloy Stress Relief Layer................ 104

5.3 The Impact of Fuel on Magnesium Zirconate Diffusivity 105

5.4 Penetration of Radiation Heat Flux into the Magnesium Zirconate Coating 107

5.5 Porosity of the Magnesium Zirconate Coating... 109

5.6 Conclusions and Contributions from the Magnesium Zirconate Diffusivity Determination... 109

CHAPTER 6 THE IMPACT OF A MAGNESIUM ZIRCONATE COATED PISTON ON CCD ACCUMULATION AND HCCI OPERATION........... 111

6.1 Impact of a Magnesium Zirconate Coated Piston on Combustion Chamber Deposit Accumulation.. 112

6.1.1 Combustion Chamber Deposit Accumulation on the Piston 112

6.1.2 Combustion Chamber Deposit Accumulation on the Cylinder Head115

6.1.3 Combustion Chamber Deposit Accumulation on the Cylinder Head Heat Flux Probes... 116

6.2 Impact of the Magnesium Zirconate Coated Piston on HCCI Operation. 118

6.2.1 Impact of the Magnesium Zirconate Piston on the Combustion Phasing Variability Induced by Combustion Chamber Deposit Accumulation 118

6.2.2 Impact of the Magnesium Zirconate Piston on HCCI Operability Limits 121

6.3 Conclusions and Contributions of the Magnesium Zirconate Piston Testing 122

6.3.1 The Impact of a Magnesium Zirconate Coated Piston on Combustion Chamber Deposit Accumulation.. 122

6.3.2 The Impact of Magnesium Zirconate Coated Piston on HCCI Operation.. 123

CHAPTER 7 CONCLUSIONS, CONTRIBUTIONS AND RECOMMENDATIONS FOR FUTURE WORK.. 125

7.1 Summary of Conclusions 126

7.1.1 Radiation Chamber Development.. 126

7.1.2 Combustion Chamber Deposit Thermal Diffusivity......................... 126

7.1.3 Characterization of the Magnesium Zirconate Thermal Barrier Coating 127

7.1.4 The Impact of a Magnesium Zirconate Coated Piston on Combustion Chamber Deposit Accumulation 128
7.1.5 Impact of a Magnesium Zirconate Coated Piston on HCCI Operation 128
7.2 Summary of Contributions 129
7.3 Recommendations for Future Work 131
BIBLIOGRAPHY 133

LIST OF FIGURES

Figure 1-1 - Comparison of ideal cycles ($\gamma = 1.3$, CR = 7.0) 6

Figure 1-2 - Effect of HCCI intake temperature on in-cylinder gas temperature [39] 10

Figure 1-3 – Effect of HCCI intake temperature on net heat release rate [39]................ 10

Figure 1-4 - Effect of HCCI coolant temperature on in-cylinder gas temperature [39] ... 11

Figure 1-5 – Effect of HCCI coolant temperature on net heat release rate [39]............... 11

Figure 1-6 – Combustion duration versus ignition for an intake temperature sweep [39] 12

Figure 1-7 – Combustion duration versus ignition for a coolant temperature sweep [39] 13

Figure 1-8 – Advance in HCCI combustion phasing and a decrease in combustion duration attributed to the formation of a CDD layer over time [12]........................ 15

Figure 1-9 – Combustion duration versus ignition for individual cycles during CCD accumulation showing the additional influence of CCD on burn duration beyond the impact of combustion phasing [12]... 15

Figure 1-10 – Effect of increasing CCD thickness on heat flux measured sub-CCD [13]16

Figure 1-11 – Cyclic breakdown of heat flux with a clean and conditioned (CCD present) HCCI combustion chamber [13].. 17

Figure 1-12 – Shift in the HCCI operability range due to CCD accumulation [13]......... 18

Figure 1-13 – Utilization of intake temperature compensation to match the net heat release rate of a conditioned state to that of a clean state [13] 20

Figure 1-14 – Separate trends of CCD diffusivity versus thickness were measured at the cylinder head and the piston [11]... 21

Figure 2-1 – The HCCI piston and cylinder head.. 30

Figure 2-2 – Schematic of the engine sub-systems [39].. 31

Figure 2-3 – Additional lobe of the rebreathe exhaust cam 33
Figure 2-4 – HCCI valve profiles 33
Figure 2-5 – Direct injection spray trajectory schematic [13] 34
Figure 2-6 – HORIBA MEXA-7100DEGR emissions bench 37
Figure 2-7 – Heat flux probe schematic 38
Figure 3.1 – Sectional schematic of the radiation chamber 47
Figure 3.2 – Creation of a pulsed heat flux source via a chopping wheel 47
Figure 3.3 – Conceptual response of the probe surface temperature to a pulsed heat flux source when clean and coated with CCD 48
Figure 3.4 – Normalized residual sum of squares for a temperature trace reconstructed with various harmonic numbers illustrating the automatic harmonic selection process 50
Figure 3.5 – Peak portion of a temperature trace reconstructed with various harmonic numbers where a harmonic number of four was automatically selected 50
Figure 3.6 – Photograph of a zirconium wafer poised for installation over the heat flux probe and via screws on the probe mounting sleeve 52
Figure 3.7 – Diffusivities for aluminum wafers of various thicknesses at different chopping disk speeds where the differing wafers are denoted by their respective thicknesses in micrometers 53
Figure 3.8 – Schematic of the non-instantaneous heat flux pulse (left) produced by the ramp up and ramp down in radiation view factor experienced by the measurement probe as the chopping wheel uncovered and subsequently recovered the line of sight to the graphite element (right) 54
Figure 3.9 – The COSMOS finite element model created of the heat flux probe, mounting sleeve and installed aluminum wafer 55

Figure 3.10 – The heat flux profiles utilized in the COSMOS finite element model and the subsequent response of the heat flux probe when both clean and coated with a 500μm aluminum wafer 56

Figure 3.11 – The heat flux probe temperature profiles predicted by the COSMOS model for aluminum wafer thicknesses of 500μm and 1500μm with heat flux pulse profiles of various shape 57

Figure 3.12 – Impact of increasing the radial cutouts and speed of the chopping wheel by a factor of three on the heat flux pulse profile 58

Figure 3.13 – Diffusivities for aluminum wafers of various thicknesses at different chopping disk speeds 59

Figure 3.14 – Normalized temperature traces of a clean probe and a probe covered with a 500μm aluminum wafer at various chopping disk speeds (in rpm) 60

Figure 3.15 – Normalized temperature trace for a clean probe and sub-wafer temperature traces for various aluminum wafer thicknesses at a constant chopping disk speed of 600 rpm exhibiting the loss of amplitude for large thicknesses 60

Figure 3.16 – Temperature profiles (left) and heat flux profiles (right) of a clean probe and a probe covered with a ceramic wafer exhibiting transparency to the radiation source and minimization of that transparency via the application of aerosol graphite 62

Figure 3.17 – Normalized temperature profiles depicting the influence of graphite aerosol on the response of a clean heat flux probe 63

Figure 3.18 – Clean and sub-wafer temperature traces for like thicknesses of alumina and zirconium ceramic at a constant chopping disk speed of 600 rpm 65

Figure 3.19 – Diffusivities for all thicknesses of the three wafer materials and their sample averages (black dashed lines) relative to the mean of the expected diffusivity range for each material (solid green lines) 65

Figure 3.20 – Ex-situ diffusivities and their standard deviations compared to the mean expected values and the range of expected values as provided by various texts...... 66

Figure 4.1 – Thickness progression on cylinder head heat flux probe #1 70

Figure 4.2 – Thickness progression on cylinder head heat flux probe #2 71

Figure 4.3 – Sectional schematic of the CCD coated cylinder head heat flux probe illustrating gaps in CCD during initial accumulation 72

Figure 4.4 – Ex-situ CCD diffusivity values exhibiting sensitivity to CCD thicknesses less than thirty micrometers 74

Figure 4.5 – Ex-situ CCD diffusivity plotted on a log scale to illustrate the shortcomings of a single power law fit... 75

Figure 4.6 – Comparison of single and piecewise trends describing ex-situ CCD diffusivity 75

Figure 4.7 – Intake temperature compensation technique developed by Güralp et al. [13] 76

Figure 4.8 –Diffusivities calculated from ex-situ and in-situ (firing) testing................... 77

Figure 4.9 – In-situ (firing) and ex-situ temperature and heat flux traces at selected CCD thicknesses illustrating the differences in phasing behavior between ex-situ and in-situ 78

Figure 4.10 – The influence of air filled CCD porosity on effective CCD conductivity . 81

Figure 4.11 – The influence of CCD porosity on effective CCD diffusivity 82

Figure 4.12 – In-situ motoring and in-situ firing temperature and heat flux traces for select CCD thicknesses 83

Figure 4.13 – In-situ motoring, in-situ firing and ex-situ diffusivities plotted on a log scale and illustrating the similarity of in-situ motoring and firing data.................... 84

Figure 4.14 – In-situ motoring, in-situ firing and ex-situ diffusivities plotted on a linear scale and zoomed to highlight the similarity of in-situ motoring and firing data..... 85

Figure 4.15 – In-situ (all) trend produced through combining both in-situ data sets together produces plotted with the individual data sets 85

Figure 4.16 – In-situ firing, in-situ motoring and ex-situ peak temperature phase lag times shown at full scale and zoomed for clarity 87

Figure 4.17 – In-situ and ex-situ peak temperature phase lag times with the in-situ motoring and firing data taken together as a single data set 87

Figure 4.18 – Impact of graphite applied to CCD surface on sub-CCD temperature and heat flux 89

Figure 4.19 – The increase in sub-CCD temperature phase delay caused by minimizing CCD radiation transparency with graphite 90

Figure 4.20 – The shift in ex-situ diffusivity caused by minimizing radiation transparency through the application of graphite to the CCD surface 90

Figure 4.21 – Temperature phase lag with constant impact of transparency applied to ex-situ results 91

Figure 4.22 – CCD diffusivities illustrating the impact of the transparency compensating temperature phasing shift on the ex-situ results.. 92

Figure 4.23 – Influence of initial CCD gaps on radiation pulse 93

Figure 4.24 – CCD accumulation schematic for thicknesses less than ~30μm illustrating the continued impact of the sparse CCD distribution 94

Figure 4.25 – CCD accumulation schematic for thicknesses from 30-40μm where the entire temperature measurement surface is now coated with CCD 94

Figure 4.26 – CCD accumulation schematic for thicknesses >40μm exhibiting the penetration of radiation into the porosity of the CCD 95

Figure 4.27 – Shifting the ex-situ phase delay curve to quantify the penetration of radiation into the CCD 96

Figure 4.28 – Effect of Shifting the Ex-Situ Phase Delay on the Ex-Situ Diffusivity Data 96

Figure 5.1 – Heat flux probes coated with MgZr with a nickel sub-layer (left) and the nickel layer alone (right) 101

Figure 5.2 – Sub-MgZr temperature and heat flux profiles exhibiting radiation transparency 102

Figure 5.3 – Sub-MgZr temperature and heat flux profiles with graphite applied to minimize transparency 103

Figure 5.4 – MgZr ex-situ diffusivity calculated using the combined thickness of both the MgZr and Ni alloy coatings 103

Figure 5.5 – Sub-nickel alloy temperature and heat flux traces illustrating the negligible impact of the nickel alloy stress relief layer on the sub-TBC phased delay 104

Figure 5.6 – Isolation of the MgZr diffusivity by removing the impact of the nickel alloy sub-layer 105

Figure 5.7 – MgZr diffusivities determined during ex-situ, in-situ firing and in-situ motoring operation showing the close agreement between the two in-situ results. 107

Figure 5.8 – Conceptual diagram of the MgZr coating illustrating the penetration of radiation into the surface porosity 108

Figure 6.1 – Piston coated with 100μm MgZr and an intermediate nickel alloy layer for stress relief 112

Figure 6.2 – CCD accumulation on metal and MgZr pistons due to passive conditioning 113

Figure 6.3 – CCD accumulation on the head of the combustion chamber due to passive conditioning tests with metal and MgZr pistons (thicknesses in micrometers)...... 116

Figure 6.4 – CCD accumulation on the head heat flux probes after passive conditioning tests with metal and MgZr pistons 117

Figure 6.5 – Influence of MgZr piston on net heat release during passive conditioning 119

Figure 6.6 – Combustion phasing versus ignition (left) and burn duration versus combustion phasing (right) illustrating the increase in CA50-90 burn duration due to the MgZr piston... 120

Figure 6.7 – HCCI operability range comparison for metal and MgZr pistons in clean and fully conditioned chamber states 122

LIST OF TABLES

Table 2.1 – HCCI engine specifications 30

Table 2.2 – Specifications for the RD3-87 test gasoline 35

Table 3.1 – Wafer thicknesses and standard deviations as measured by the Fischer Dualscope both with and without high conductivity heat sink grease between the wafer and the probe surface 52

Table 3.2 – The impact of heat sink grease sub-layer and graphite surface treatment on installed wafer thicknesses as measured by the Fischer Dualscope 64

Table 4.1 – CCD thicknesses and standard deviations at the various stopping points of the passive conditioning cycle 69

ABSTRACT

Combustion chamber deposits, CCD, have been shown to influence the operational range of homogeneous charge compression ignition, HCCI. CCD insulate the combustion chamber during the intake and compression strokes, preserving enough charge temperature to shift the HCCI operational range to lower loads where the HCCI fuel economy benefit over traditional spark-ignited combustion is at a maximum. However, the drive cycle dependent CCD accumulation and burn-off creates uncontrolled shifting of the HCCI operability range, which must be mitigated in a practical multi-mode engine. Ideally, the beneficial shift of HCCI operation to lower loads provided by CCD could be obtained while avoiding uncontrolled shifting of the operational range.

To provide fundamental insight into CCD properties, CCD thermal diffusivity was non-destructively measured during HCCI combustion (in-situ firing), during engine motoring (in-situ motoring) and in a specially designed radiation chamber (ex-situ). The diffusivity measurement methodology utilized the phase lag in sub-CCD temperature signals and the one dimensional heat diffusion equation. Comparisons of the CCD diffusivity values determined from the different measurement environments allowed the separation of several thermal and morphological CCD characteristics.

The interaction of fuel with the CCD morphology was shown to have no significant impact on the diffusivity of CCD accumulated on the cylinder head. CCD less than thirty micrometers were spatially sparse and contained line-of-sight pathways though which the ex-situ radiation could pass and the in-situ convection could not. Thicker CCD exhibited differential sensitivity to radiation and convection heat transfer modes, which was utilized to quantify the effective porosity of the CCD through a novel radiation penetration factor.

The impact of thermal barrier coatings on CCD accumulation and HCCI operability was assessed by testing a piston coated with magnesium zirconate, MgZr. The radiation penetration factor determined the MgZr coating to have 2.5 times the effective porosity of CCD. Reductions in CCD accumulation resulted from the elevated surface temperature of the MgZr. In addition, reduced cylinder head CCD accumulation was speculatively attributed to interaction between the surface roughness of the MgZr piston and the fuel spray. Overall, the HCCI operability shift due to CCD accumulation was reduced by the MgZr piston.

CHAPTER 1

INTRODUCTION, MOTIVATION AND OBJECTIVES

Worldwide oil consumption is projected to increase 60% by 2020 due, in part, to increasing demand of developing countries [1], [2]. These forecasts of increased demand for the ever dwindling natural resource continually inspire researchers to pursue efficiency gains to help ration the world's oil supply. Additional research impetus is supplied by the ever increasing Corporate Average Fuel Economy (CAFÉ) regulations, which force the development and incorporation of new technology by auto suppliers in order to achieve the government mandated fuel economy targets [3].

Dual mode engines which incorporate both Homogeneous Charge Compression Ignition, HCCI, and spark ignition, SI, represent a research area aimed at achieving greater fuel economy [4]. HCCI promises to deliver fuel economy improvements at low load operation where conventional SI engines are particularly inefficient. Though HCCI technology shows promise, many challenges remain pertaining to the practical control and load range expansion of the HCCI combustion regime [5]-[7].

Thermal management is of paramount importance in a HCCI engine due to the lack of a direct control over mixture ignition. Ignition of the HCCI charge is thermo-kinetically driven [8], which remains the subject of current research efforts [9], [10]. Complete understanding of in-cylinder conditions from the time of charge induction is necessary to predict the state of the fuel/air charge during the compression process. This accurate assessment of charge conditions allows the thermo-kinetic ignition timing to be forecasted and HCCI combustion to be controlled.

The influence of combustion chamber deposits, CCD, on the combustion chamber’s thermal environment, the subsequent shift of the HCCI operability range to lower loads due to CCD formation, and the sensitivity of the CCD layer to differing engine operational conditions have been established [11], [12], [13]. However, relatively little is known about the thermophysical properties of the HCCI CCD and how those properties cause the observed changes in HCCI combustion. To obtain successful HCCI combustion management over the diverse operational transients of an engine, the issues created by CCD must be understood and controlled. This investigation will study the thermophysical properties of both HCCI CCD and other thermal barrier coatings and determine their impact on HCCI combustion.

1.1 Homogeneous Charge Compression Ignition Background

Conventional spark ignition, SI, engines rely on flame propagation through a homogenous mixture of fuel and air. Because spark plugs require a finite range of fuel-air mixtures for proper ignition, conventional SI concepts utilize a homogeneous, stoichiometric mixture and control load with an intake throttle. The intake throttle limits the pressure of the intake air below that of the crank case during part load operation, which creates pumping losses throughout the gas exchange strokes. (While these limitations restrict the thermal efficiency of conventional SI engines, modern direct injection spark ignition, DISI, engine concepts have reduced these losses.) SI emissions are easily kept to modern cleanliness standards via a three way catalyst, making SI combustion a mainstay for personal transportation despite its efficiency limitations.

Compression ignition, CI, combustion strategies utilizes high compression ratios to heat the intake air charge to a point where injected fuel burns as it atomizes. The traditional CI concept does not rely upon a spark plug for ignition and can therefore vary the fuel input to change load (instead of using an intake throttle). The higher compression ratio, lean operation and the lack of a throttle contribute to CI combustion having a higher thermal efficiency than conventional SI engines. However, this thermal efficiency benefit comes at a price. The stratified nature of the fuel/air charge leads to lean, stoichiometric, and rich regions during the combustion process. The end result is a particulate-NO_x emissions tradeoff that remains, at the current juncture, unsolved on a production level [14]. Thus, to meet current stringent emissions regulations requires an increasingly complicated combination of expensive aftertreatment devices.

HCCI is commonly viewed as a marriage between CI and SI combustion technologies and represents an attempt to have one’s cake and eat it too. HCCI combines the high compression ratio, lean operation and unthrottled intake of a CI engine with the premixed charge of a conventional SI engine to achieve high efficiency combustion with low emissions [15]. These advantages make HCCI an attractive concept, but they cannot be obtained without difficulty. The advantages and deficiencies of the HCCI concept will be detailed in the following sections.

1.1.1 Benefits of Homogeneous Charge Compression Ignition

HCCI combustion can provide many benefits over both conventional SI and CI. While its limitations, which will be covered in the next section, prevent it from being a standalone engine concept, it provides some substantial improvements: wide open throttle operation, lean combustion, high compression ratios, rapid burn rates and low soot and NO_x emissions.

Wide Open Throttle Operation

HCCI combustion has a distinct efficiency advantage over conventional SI combustion due to its wide open throttle operation. As the load is decreased in a conventional SI engine, the intake throttle closes and reduces the amount of air drawn into the cylinder. This allows the fuel quantity to be decreased while maintaining a mixture which is spark ignitable. However, at light load conditions, the intake throttle closes far enough to drop the intake manifold pressure below the pressure of the crank case. Because of this adverse pressure gradient, the engine must work to force the piston down during intake, creating what is known as pumping loss [16]. Combustion concepts where equivalence ratio can be varied to alter load avoid the use of intake throttles and their associated pumping losses.

Lean Equivalence Ratios

The lean operation of HCCI combustion has a significant contribution to its high efficiency [16]. The expansion process is commonly modeled as isentropic with the ratio of the working fluid’s specific heats, γ, being used as the isentropic exponent. As the cylinder mixture becomes leaner, the value of γ increases toward 1.4 (the value of γ for pure air). As the isentropic exponent is increased, the amount of work produced via the expansion process increases. This lean operation represents a benefit over traditional SI combustion where the mixture’s equivalence ratio is fixed at stoichiometric.

High Compression Ratio

With flame propagation combustion, i.e. SI combustion, the flame travels across the combustion chamber further compressing and heating the unburned gases beyond the effect of geometric compression. If the fuel-air mixture in the end gas region reaches a high enough thermal state before the flame arrives, the end gas ignites on its own or knocks. Knock causes extreme pressure rise rates and peak pressure values which can damage the engine components. The compression ratios of conventional SI engines are limited to avoid this phenomenon. HCCI engines, however, are not burdened by a knock constraint on their compression ratios and, since fuel conversion efficiency increases with increasing compression ratio [16], HCCI engines realize an efficiency benefit over conventional SI engines.

Rapid Burn Rates

Constant volume combustion, CV, is characterized by instantaneous heat release at top dead center and has a higher efficiency than both limited pressure, LP, and constant pressure, CP, combustion methods [16]. SI combustion heat release is controlled by flame propagation and is therefore best approximated by the LP combustion model. The discernable combustion duration allows the piston to begin moving downward thereby reducing the peak cylinder pressure and the cycle efficiency.

The bulk of compression ignition, CI, combustion occurs while the piston is in its downward motion, being resisted by a constant force. Therefore, CI combustion is approximated by the CP model and has the lowest efficiency of the three models at the same compression ratio and γ. CI gains its advantage over SI when peak cylinder pressure is used as the constraining factor. Per unit of peak pressure, the CP cycle produces more work than the LP and CV cycles. Figure 1-1 illustrates these points.

With HCCI, the homogenous mixture ignites at multiple locations within the cylinder simultaneously whenever local conditions are favorable to ignition [17]. HCCI combustion occurs as a rapid sequence of autoignition which cascades through the cylinder contents [18]. Thus, HCCI represents a step towards the CV model from the LP model. Therefore, the HCCI combustion method enjoys a higher efficiency per unit compression ratio than both the CI and SI combustion methods.

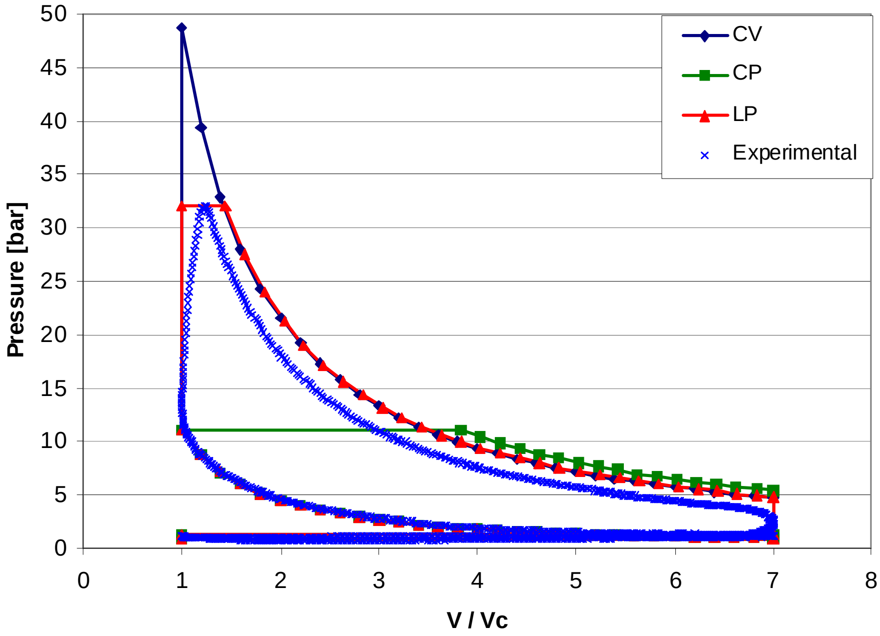

Figure 1-1 - Comparison of ideal cycles ($\gamma = 1.3$, CR = 7.0)

Emissions Benefits

The lean nature of the HCCI fuel-air charge also leads to reduced NO_x formation [20], [21], [22]. The lean conditions translate to low combustion temperatures, preventing the formation of NO_x via the Zeldovich mechanism [16], [19]. The stoichiometric nature of the fuel-air charge in conventional SI combustion leads to relatively high combustion temperatures, resulting in high NO_x production via the Zeldovich mechanism. As the mixture is expanded and the charge temperature decreases, the chemistry of the reverse molecular reactions freeze and a net formation of NO_x results. A similar phenomenon occurs in the stoichiometric regions of the heterogeneous CI charge where combustion temperatures reach levels that activate the Zeldovich mechanism. Thus, the low NO_x formation of HCCI combustion provides an advantage over both conventional SI and CI.

HCCI combustion produces significantly less soot than CI. The heterogeneous fuel-air mixture utilized in CI combustion contains rich regions in which soot is formed due to the partial oxidation and then condensation of hydrocarbon, HC, molecules [16]. The lean, homogenous nature of the HCCI charge ensures that its soot emissions remain low when compared to CI [23].

1.1.2 Detriments of HCCI

The efficiency and emissions advantages that HCCI provides come with shortcomings. This section will cover the detriments and challenges provided by HCCI: ignition control, load limitations, and higher hydrocarbon and carbon monoxide emissions than some combustion concepts.

Ignition Control

There is no direct control of the ignition process in an HCCI engine. With CI combustion, the timing and duration of the fuel injection event can be altered to instigate ignition as desired. In SI combustion, the spark timing can be altered to obtain control over ignition. HCCI utilizes extremely early injection timings to obtain homogeneity of the lean fuel-air mixture. Therefore, the CI strategy cannot be employed because it would compromise the mixture homogeneity. Additionally, the lean nature of the homogeneous mixture renders spark plugs an ineffective ignition source. Thus, controlling HCCI ignition poses a problem to researchers because the last user input to the HCCI combustion process is hundreds of crank angle degrees before ignition is desired. With no external input, HCCI ignition is controlled by the chemical kinetics of the auto ignition process. The chemical kinetics can be characterized through the Arrhenius rate expression [19], which is temperature dependent. Thus, the important factors for HCCI auto ignition are charge temperature history, equivalence ratio and mixing.

Load Limitations

Because the contents of the entire cylinder auto ignite nearly simultaneously with HCCI, the burn rates and associated rate of pressure rise can quickly exceed the limits of present engine materials. Thus, a maximum load limit must be established to avoid excessive peak pressures and rates of pressure rise [24]. Efforts have been made to expand the operability range of HCCI combustion while avoiding excessive rates of pressure rise through thermal stratification of the charge, compositional stratification of the charge, and active control of intake and coolant temperatures [25], [26], [28]-[35].

In order to obtain the required thermal energy to auto ignite the lean homogeneous mixture, HCCI engines often rely on large quantities of exhaust gas recirculation, EGR. However, as the load is decreased the thermal energy within the EGR decreases and the new fuel-air charge cannot obtain the necessary amount of thermal energy to promote auto ignition. This misfire condition establishes a low load limit for HCCI operation [27].

Emissions Shortcomings

HCCI suffers from increased hydrocarbon, HC, and carbon monoxide, CO, emissions compared to conventional SI combustion [34]. With HCCI, a thermal boundary layer region exists near the cylinder walls where temperatures remain low due to heat transfer with the cylinder walls [35]. Within this region, temperatures can be low enough that the chemical kinetics of the mixture never activate. This prevents combustion in the thermal boundary layer and results in CO unburned HC emissions which exceed that of conventional SI combustion [16], [35].

1.1.3 Thermal Influences on Homogeneous Charge Compression Ignition

Since HCCI does not utilize a user input as the trigger for autoignition, the temperature history of the fuel/air mixture must be closely monitored to ensure proper combustion phasing. Phasing too advanced may lead to material failures while phasing too retarded will lead to misfire. Intake temperature and the temperature of the combustion walls have significant impacts upon the temperature history of the fuel/air mixture and have therefore been a subject of recent research efforts to extend the operational range of HCCI [28] - [33].

The Effect of Intake Temperature

Changing the intake air temperature alters the thermal energy available to the fuel-air mixture and therefore has a significant effect on the chemical reactions which control the early stages of HCCI combustion via the Arrhenius rate expression [8], [18], [19]. It has been shown that intake temperature can be increased to maintain constant burn rates while leaning out the fuel-air mixture [36].

A study on the combined effects of intake air temperature, compression ratio and coolant temperature on the start of heat release in HCCI combustion concluded that HCCI ignition is more sensitive to changes in intake temperature than changes in equivalence ratio at the same compression ratio [37]. Higher intake temperatures allow HCCI operation over a wider equivalence ratio range and can help extend that range for a large variation of speed [38].

Chang et al [39] showed that intake charge temperature affects the cylinder mixture’s core gas temperature and thus the ignition timing of the mixture, see Figure 1-2. Altering the intake charge temperature can be used to control the peak burn rate by controlling the net heat release rate of the HCCI mixture shown in Figure 1-3 [36] - [39].

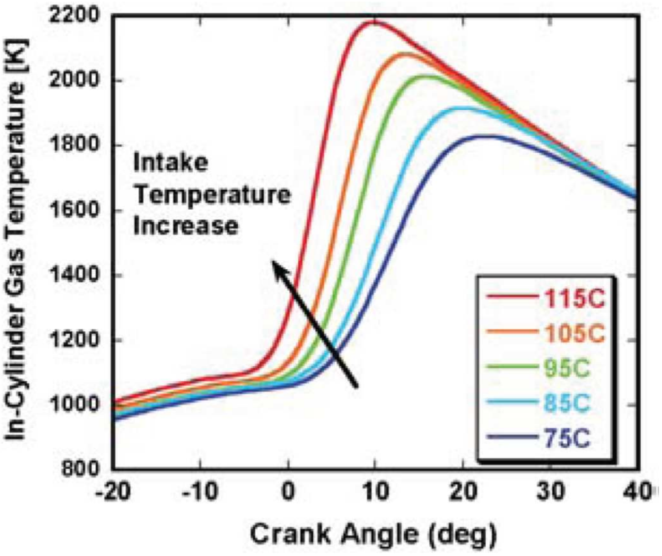

Figure 1-2 - Effect of HCCI intake temperature on in-cylinder gas temperature [39]

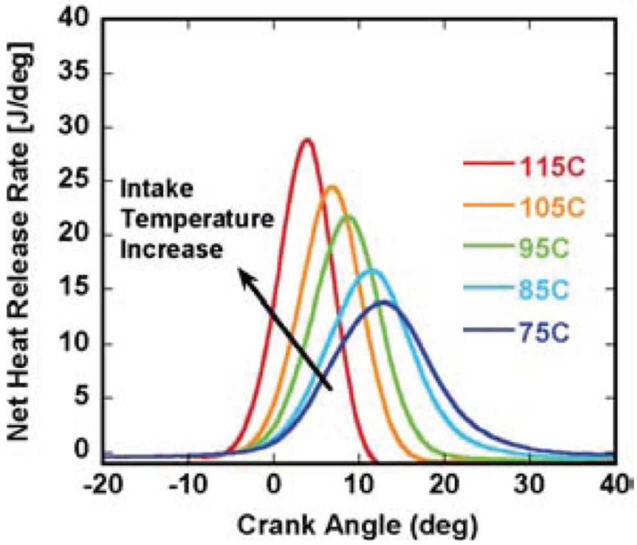

Figure 1-3 – Effect of HCCI intake temperature on net heat release rate [39]

Effect of Wall/Coolant Temperature

Coolant temperature can also be used for burn rate control in HCCI combustion [31], [33], [37], [39]. Chang et al [39] utilized alterations in coolant temperature to induce variances in cylinder wall temperature. Although Iida et al [37] noted that the start of heat release “becomes earlier” with higher coolant temperatures, Figure 1-4 and Figure 1-5

[39] show that the impact of coolant temperature on the in-cylinder gas temperature and the net heat release rate occurs after combustion has begun.

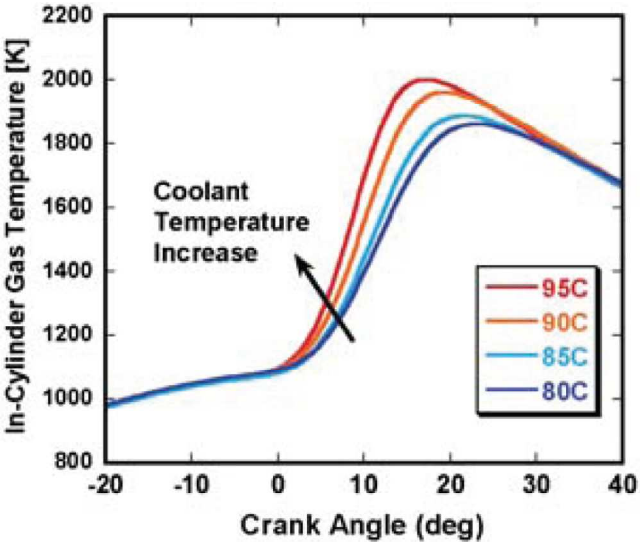

Figure 1-4 - Effect of HCCI coolant temperature on in-cylinder gas temperature [39]

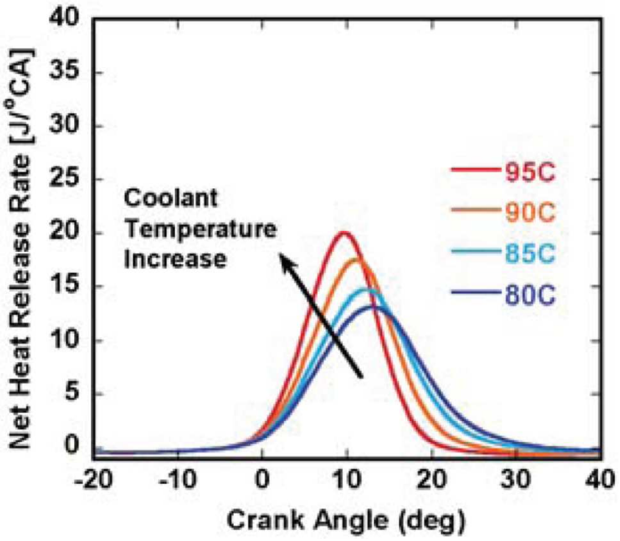

Figure 1-5 – Effect of HCCI coolant temperature on net heat release rate [39]

Comparing the Effects of Coolant and Intake Temperature

It was found that HCCI burn rates respond in a stronger fashion to changes in wall temperature than changes in intake temperature. A 15°C change in coolant temperature produced the same net mean effective pressure variation that required an intake temperature change of 40°C [39].

Further investigation [39] showed that the effect of coolant temperature on HCCI combustion differed from that of intake temperature. Analysis of individual cycles showed that changes in burn duration during a sweep of intake temperature depended solely on the point of ignition, Figure 1-6. The trend of combustion duration versus ignition for a coolant temperature sweep saw an additional change in duration beyond what solely an advance of ignition would dictate, hence the weaker R^2 correlation for that duration versus ignition trend, Figure 1-7. This effect was attributed to the coolant temperature varying the size of the near-wall thermal boundary layer and thereby influencing the near wall burn (50-90% mass fraction burn) more than the core gas burn (10-50% mass fraction burn).

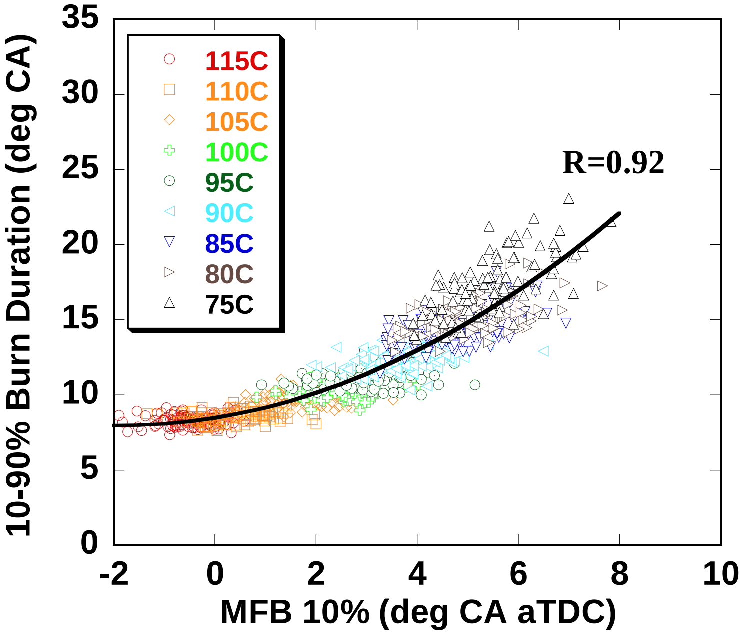

Figure 1-6 – Combustion duration versus ignition for an intake temperature sweep [39]

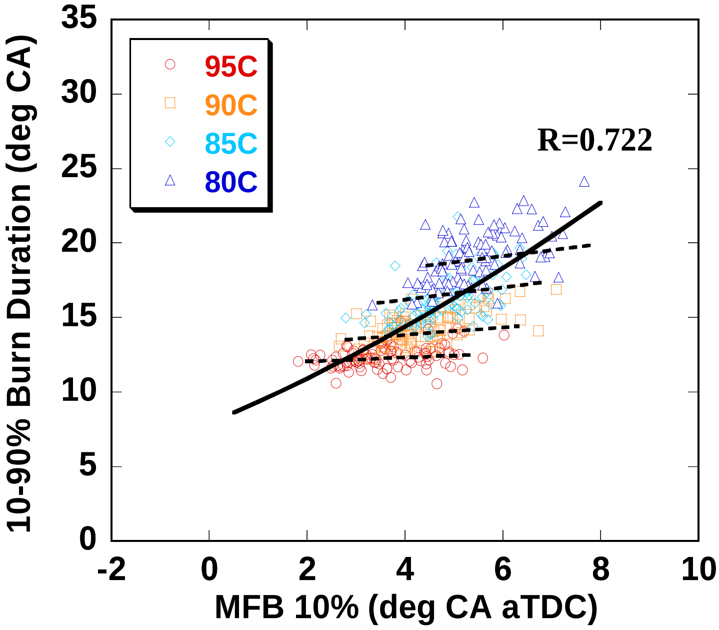

Figure 1-7 – Combustion duration versus ignition for a coolant temperature sweep [39]

1.2 Combustion Chamber Deposit Background

A large body of work has been devoted to the study of CCD. The majority of this work deals with CCD formation in SI and CI engines while work with HCCI CCD has seemingly just begun. Discrepancies arise when the dominant influence of CCD is discussed. Many researchers believe CCD predominantly have a thermally insulative effect on combustion while others contest that the physical properties of the CCD layer's microstructure play the larger role. A systematic separation of these different CCD properties will be necessary to end this debate.

1.2.1 Combustion Chamber Deposit Formation

There is general agreement that the formation of CCD is a condensation of partially burned fuel and oil on the combustion chamber surfaces. Composition of the combustion charge and the temperature of the chamber surfaces are therefore important parameters for CCD accumulation. However, the dominant thermophysical property of

CCD (the property which most strongly controls the effect of CCD on combustion) remains unproven.

The temperature dependence of CCD formation has been studied for conventional combustion modes [40], [41] and [42]. CCD growth increased at lower combustion chamber wall temperatures and decreased as the chamber wall temperature rose. The independent studies defined a threshold combustion chamber wall temperature of 310-320°C above which no further CCD accumulated. The concept of a threshold wall temperature was in agreement with the stabilization of the CCD layer thickness noted by several researchers [12], [13], [41], and [42]. In these studies, the CCD accumulation halted once its insulating effect elevated the CCD surface temperature to the point where the rate of CCD deposition equaled that of CCD burn-off.

Several researchers argue the shortsightedness of viewing CCD as purely a thermal insulator [44], [45], [46]. They suggest that both the surface roughness and porosity of the CCD layer interact with the fuel-air mixture during combustion. Their claim is that these CCD morphological properties alter local mixing characteristics and thereby affect combustion.

1.2.2 Influence of Combustion Chamber Deposits on Homogeneous Charge Compression Ignition

Spark ignition engines generally experience an octane requirement increase, ORI, with increased deposit growth. Because the CCD layer helps prevent heat loss from the combustion chamber, the end gas regions become more prone to engine knock. Since HCCI combustion utilizes compression triggered autoignition, the insulating effect of the CCD layer makes HCCI combustion more robust. Güralp, [12] and [13], showed that CCD cause HCCI ignition to advance and the combustion duration to decrease, Figure 1-8.

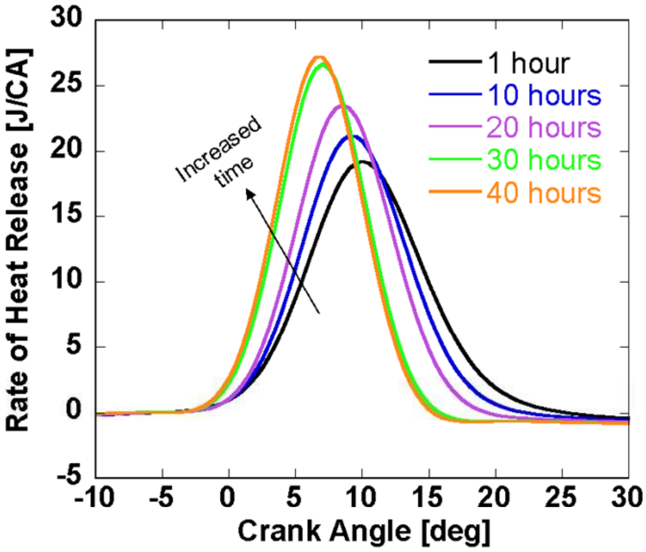

Figure 1-8 – Advance in HCCI combustion phasing and a decrease in combustion duration attributed to the formation of a CDD layer over time [12]

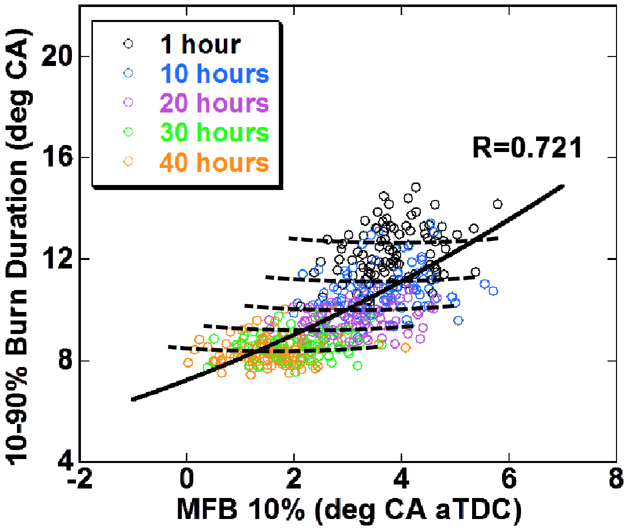

Figure 1-9 – Combustion duration versus ignition for individual cycles during CCD accumulation showing the additional influence of CCD on burn duration beyond the impact of combustion phasing [12]

The accumulation of a CCD layer yielded a larger decrease in combustion duration than would be attributed to a mere advance in combustion phasing, Figure 1-9. This effect is similar to the aforementioned impact of coolant temperature changes presented earlier in Figure 1-7, i.e. CCD affect near-wall burning to a greater extent than a simple change to the core gas temperature at the end of compression. Recent work has reinforced the impact of wall temperatures on thermal stratification throughout the chamber [47]. Thus, CCD accumulation has the potential to impact both HCCI ignition and burn duration.

Effect of Combustion Chamber Deposits on Heat Transfer

Güralp [13] also showed that, as CCD thickness increased over time, in-situ thermocouple measurements became insulated. This insulating effect materialized as a reduction in measured temperature and heat flux accompanied by a phasing retard of those signals, Figure 1-10. Although the peak instantaneous heat transfer was reduced and retarded, the cumulative heat loss measured at each location for the entire cycle changed very little due to CCD formation, correlating well with the work of Ishii [43].

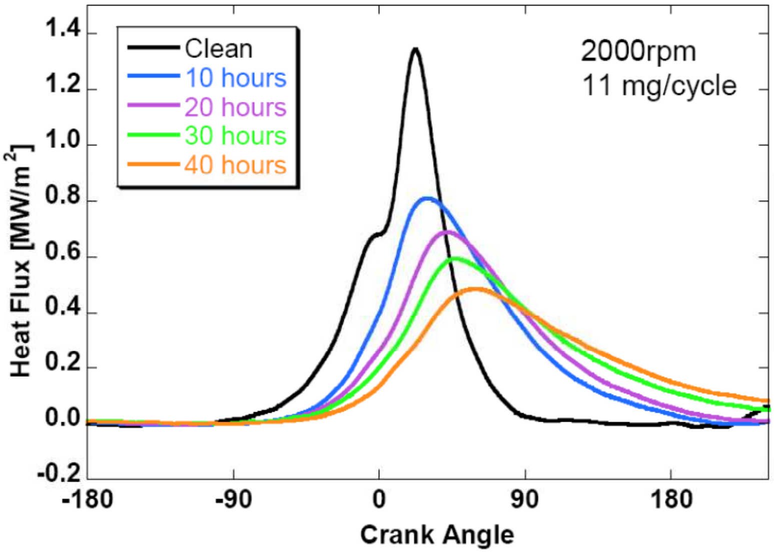

Figure 1-10 – Effect of increasing CCD thickness on heat flux measured sub-CCD [13]

However, there was a significant shift in the phasing of the heat loss with the presence of CCD, Figure 1-11 [13]. The CCD layer was shown to reduce heat loss during compression which led to advanced ignition and higher heat release rates (refer back to

Figure 1-8). Heat was only momentarily held in the chamber by the CCD layer, allowing for more robust late burn and an increase in heat flux during the expansion stroke. However, cumulative heat loss remained the same with and without CCD. Thus, the phasing of the heat loss caused by the diffusivity of the CCD layer changed the HCCI combustion characteristics.

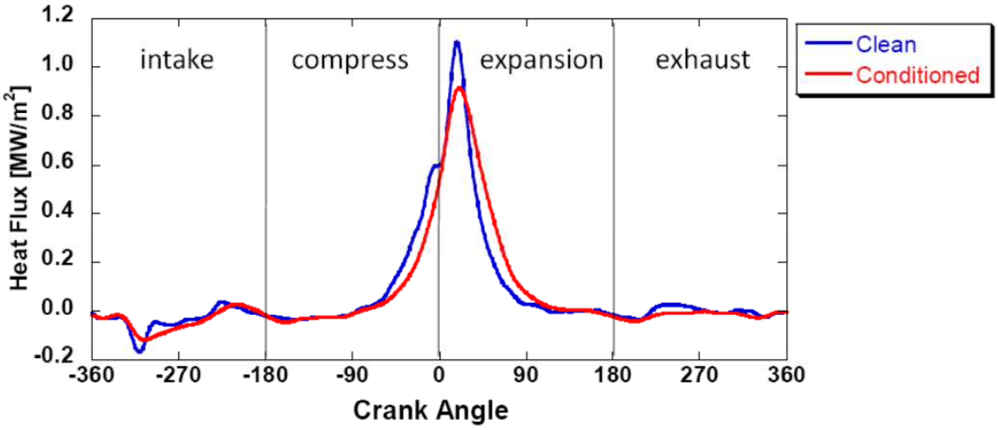

Figure 1-11 – Cyclic breakdown of heat flux with a clean and conditioned (CCD present) HCCI combustion chamber [13]

Impact of Combustion Chamber Deposits on Homogeneous Charge Compression Ignition Operability Limits

The aforementioned alterations to the phasing and duration of the HCCI burn characteristics caused by CCD accumulation altered the operability range of a practical HCCI engine. Güralp et al [13] showed that CCD formation advanced ignition and created a more rapid rate of heat release, shifting the entire HCCI load regime towards lower loads, Figure 1-12. In their work, the high load limitation was defined by a pressure rise rate of 50bar/msec, which is the threshold for creation of an audible ringing noise [24]. The low load limit was defined by a coefficient of variation, COV, in indicated mean effective pressure, IMEP, of 3%. This CCD-caused shift in operation range represented the HCCI operational variability associated with CCD.

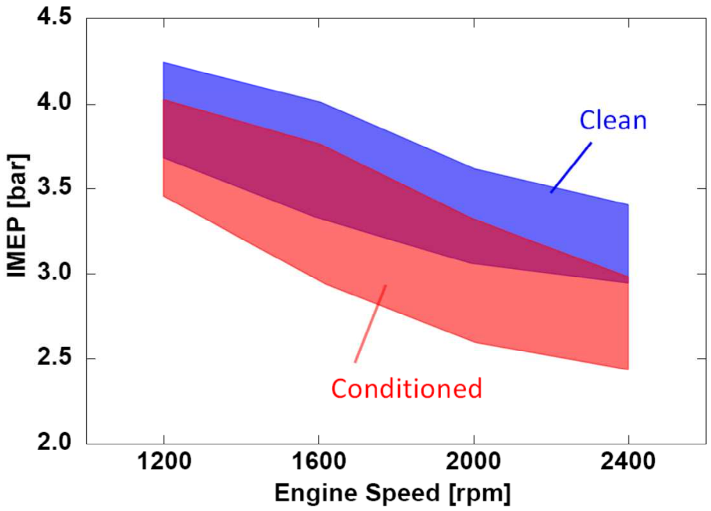

Figure 1-12 – Shift in the HCCI operability range due to CCD accumulation [13]

1.2.3 Combustion Chamber Deposit Properties

Attempts have been made to measure and calculate the properties of CCD. The fragility of the CCD layer renders many well established techniques for characterizing properties of a substance ineffective. (Some of the traditional techniques for thermal property evaluation will be covered later in this document.) Several novel methods have been developed to circumvent this problem. Nishiwaki [48] used laser radiometry in a specialized chamber attached to a motoring engine. Under these conditions, diffusivities on the order of 1.2×10^{-6} - 2.8×10^{-6} m^2/s for and SI engine and 2.0×10^{-6} – 3.4×10^{-6} m^2/s for a diesel engine were derived from measurements of CCD thickness and penetration time. Their simplification of one dimensional, unsteady heat flow is expressed in Equation (1.1) where s is CCD thickness and τ is penetration time.

$$\alpha = \frac{s^2}{6\tau} \tag{1.1}$$

Thermal conductivities were calculated through an iterative application of one dimensional heat conduction. The sub CCD temperature trend was measured and the CCD surface temperature was inferred by a radiometer. Conductivity values were tried by guess with the measured thickness, diffusivity, and deposit wall interface temperature until the error between calculated CCD surface temperature and measured CCD surface temperature was minimized. Values of conductivity ranged from 1.06 – 1.24 W/(mK) in and SI engine and from 1.14 – 1.84 W/(mK) in a diesel engine. The main fault with this methodology was the fact that CCD properties were measured at motoring conditions and not subjected to levels of heat flux that represent combustion.

Hopwood et al [49] developed a technique to measure diffusivity in-situ which relied upon measurements of both the CCD thickness and the phase delay of the sub-CCD peak temperature measured at the combustion chamber wall. Hopwood determined that the diffusivity of the CCD layer, α, could be given by Equation (1.2) where x is the deposit thickness, t_0 represents the cycle period for the 4-stroke engine cycle, and Δt is the delay in the peak temperature signal due to deposit buildup. Diffusivities for an SI engine were reported as $0.85 – 4.2\text{x}10^{-7}$ m^2/s with "significant variation between tests".

$$\alpha = \left(\frac{x}{\Delta t} \frac{\left(1+\sqrt{2}\right)}{6} \right)^2 \frac{t_0}{\pi} \tag{1.2}$$

While the Hopwood methodology provides a measure of CCD properties at combustion conditions, the in-situ measurements are subject to many thermal and morphological effects at the same time. Not only are the thermal properties of the CCD layer insulating the heat flux probes, creating a phase lag, and reducing peak temperature, but the porous nature of the deposits may be providing a dynamic effect by absorbing and releasing fuel droplets and vapor [44]-[46]. The simultaneous effects of both the thermal and fuel-CCD morphological interactions may be confusing the determination of the CCD layer's effective thermal properties. Separation of these effects will be necessary for full understanding of the CCD effect on combustion.

The methodology of Hopwood was adopted at the University of Michigan for the in-situ determination of the thermal diffusivity of the CCD layer [11]-[13]. Güralp noted that the effect of increased burn rates due to the advance in combustion must be negated by intake temperature compensation to determine the true effect of CCD on combustion, Figure 1-13. Once heat release rates were matched to clean phasing, the remaining effects seen in the sub-CCD temperature measurements were due to CCD properties.

CCD diffusivities were calculated at a variety of CCD thicknesses for locations on the cylinder head and piston surfaces. Two distinct trends emerged. One trend corresponded to the piston measurements and the other to the cylinder head measurements, Figure 1-14 [13]. The distinct separation of these two trends based on the area of the chamber where the CCD accumulated was attributed to differences in CCD morphology between the locations. Again, this asserts the need to separate and quantify the individual properties of CCD layers to fully understand their impact on combustion.

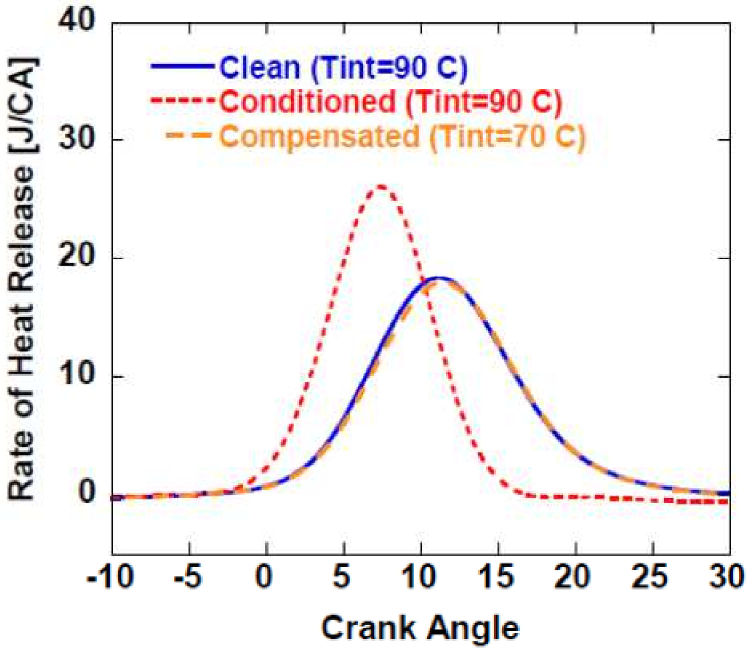

Figure 1-13 – Utilization of intake temperature compensation to match the net heat release rate of a conditioned state to that of a clean state [13]

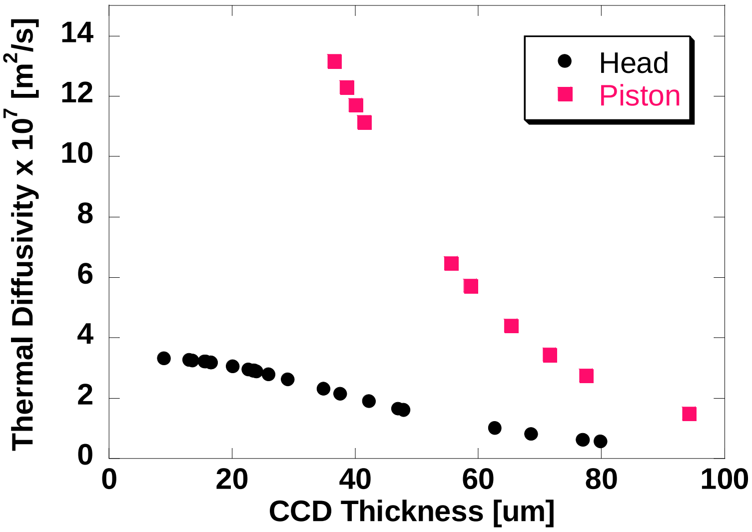

Figure 1-14 – Separate trends of CCD diffusivity versus thickness were measured at the cylinder head and the piston [11]

1.3 Thermal Barrier Coatings

Thermal barrier coatings have been used in the gas turbine industry on turbine blades and combustor parts to increase the temperature resistance of those components. Some studies [50], [52] and [53], and, have indicated that application of thin ceramic coatings with select thermophysical properties can improve emissions and reduce heat loss without reducing volumetric efficiency.

Since CCD accumulation is sensitive to the chamber wall temperatures, the thickness of the CCD layer becomes drive-cycle dependent. CCD accumulation and subsequent burn-off introduces variability through uncontrolled shifting of the HCCI operability map. The larger the operability shift between clean and conditioned chamber states, the harder the HCCI engine will be to control. Thus, HCCI combustion would benefit from the consistent wall temperature that an applied thermal barrier coating can provide. The thermal barrier coating could elevate the combustion chamber surface temperatures and limit CCD growth, effectively reducing the shift in operability introduced by CCD accumulation. However, the thermal and morphological properties of

HCCI CCD must be determined so that a TBC can be designed for use in the HCCI engine.

1.3.1 Thermal Barrier Coatings Applied to Engines

Assanis [50] sprayed thin TBC (0.13mm on the piston, in particular) on an SI engine and noticed improvements in brake specific fuel consumption (BSFC) of around 5% during part load operation. The TBC retrofitted engine also produced brake torque output between eight and eighteen percent higher and showed minimal deposit formation over 40 hours of testing.

Similar results were seen in a diesel engine [51]. A 0.5mm coating resulted in generally improved performance especially at lower rpm, which was attributed to a reduction in heat loss. Thermal efficiency gains of 10% were noted. Thicker TBC were also tested, but resulted in diminished performance compared to the baseline metal engine.

Emission results vary based upon the specific engine and coating configuration. However, some researchers are in general agreement that TBC have the potential to reduce unburned hydrocarbon emissions [52], [53].

1.3.2 Determining the Properties of Thermal Barrier Coatings

There are well established techniques for determining the properties of TBC. In the majority of cases, the TBC materials are of robust construction and can be subjected to a variety of classic methods for determining porosity, density, and heat capacitance. Thermal diffusivity can be calculated by a variety of methods including: the flash method, the 3ω method and the photoacoustic method. And, once the diffusivity of a TBC is known, conductivity is a simple multiplication of diffusivity by both coating density and heat capacitance.

Taylor performed a comparison of the various property determination methodologies [55]. The laser flash, 3ω, and photoacoustic techniques all yielded accurate diffusivity results within their specified setup conditions. The laser flash method shows a particular advantage when testing thermal properties at elevated temperatures. However, the flash technique relies critically on measurements of the coating thickness while the other methods do not.

This section outlines established methods for determining the thermal properties of a TBC. The effective application of TBC to a HCCI engine requires the design of the TBC to closely duplicate the properties of CCD. Thus, the TBC might provide the operational shift created by CCD without their associated the operational variability. Ideally, the selected method for determining TBC properties would also be applicable to testing CCD to preserve a basis of comparison between results. Although the methods presented here work well for TBC, they are inapplicable to fragile CCD.

Flash Method

The flash method was establish by Parker et al [56], and has grown in popularity to account for nearly half of all TBC diffusivity calculations. The method involves subjecting one face of a TBC sample, which is thermally insulated, to a very quick pulse of heat energy and measuring the temperature change on the opposite face. (The front surfaces of the samples were coated with camphor black to increase energy absorption.) Diffusivity, α, could then be calculated through Equation (1.3), where L is the thickness of the sample, and $t_{1/2}$ is the time necessary for the backside surface temperature to reach half of its maximum value.

$$\alpha = 1.38\frac{L^2}{\pi^2 t_{1/2}} \tag{1.3}$$

This method works under the following conditions: i.) The heat exposure time is negligibly short compared to the sample's thermal diffusion time, which is a function of sample thickness. ii.) The heat is applied uniformly to the specimen surface. iii.) The sample is adiabatic after exposure to the heat source and while the measurement is being made. iv.) The sample is homogenous.

If the amount of energy absorbed by the front face of the specimen, Q, is known, then the product of the density, ρ, and the heat capacity of the material, C, are given by Equation (1.4) where T_M is the maximum temperature of the specimen's rear surface [56].

$$\rho C = \frac{Q}{LT_M} \tag{1.4}$$

Then the sample's conductivity, K, can be found from Equation (1.5).

$$K = \alpha\rho C \tag{1.5}$$

The method established by Parker [56] has since been utilized by other researchers [57], [58], [59] who constructed laser pulse apparati for measuring thermal properties of insulated substances at high temperatures. These researchers agree that Parker's technique is adequate for diffusivity measurements made at less than 1500K sample temperature.

The use of calorimeters for determination of sample heat capacities was more widely utilized than measurements of total heat input to the sample and subsequent use of Equations (1.4) and (1.5). Density was determined in a variety of methods from cross sectional image analysis to simple volume and mass measurements. However, both of these methodologies cannot be implemented with a fragile CCD coating.

3-Omega Method

The 3ω method was developed to determine conductivity of dielectric solids as thin as tens of microns [61]. A thin line of metal was deposited on the surface of the specimen and a current at angular frequency ω was passed through the metal line and heated the sample at 2ω. As the temperature of the pure metal line was increased, the resistance increased and had a small alternating component that oscillated at 2ω. When this resistance oscillation was multiplied with the original current, it resulted in a small oscillation of voltage across the line at 3ω. The slope of the in-phase temperature fluctuation versus the logarithm of the heater frequency gave the thermal conductivity.

Unfortunately, this method requires the deposition of metal onto the surface of the specimen, rendering it inadequate for use with CCD due to the fragility of the CCD microstructure.

Photoacoustic Method

As a specimen is subjected to chopped monochromatic light an acoustic signal is produced. If the sample is thermally insulated and placed in a chamber with a sensitive microphone, the analog signal can be applied to a tuned amplifier and the output will be recorded as a function of the incident light [62]. The observed acoustic signal corresponds to the periodic heat flow from the solid to the surrounding gas. The boundary layer of air nearest the specimen’s surface can be considered a vibratory piston, responding to the periodic heat flow and producing the periodic pressure fluctuations picked up by the microphone. Rosencwaig determined that the photoacoustic signal is governed by the thermal diffusion length of the solid. The diffusivity of the sample is determined from the phase lag between the heat source and the acoustic wave [55].

Again, this method cannot be applied to CCD. The specimen needs to be placed on a thermally insulated substrate and the removal of CCD from our combustion parts would destroy the morphology of the layer.

1.3.3 Effects of Morphology on Thermal Properties of Thermal Barrier Coatings

There is a general agreement that TBC thermal properties are dependent on the morphology of the layer. Conductivity, in particular, has a direct dependence upon the porosity and crack geometry of the layer’s morphology [55], [63] - [66]. In fact, not only is pore density an important parameter in determination of the layer’s conductivity, but orientation of the cracks, pores and pore shape can play a significant role [65] - [67].

Cracks which run perpendicular to the direction of heat flux reduce conductivity. Sevostianov concluded that the overall porosity plays a secondary role and that the pores can be idealized as cracks. Effective properties can be expressed in crack parameters (density and orientation) and porosity would play a correctional role for porosities under 15% [66].

Conductivity values can increase significantly due to heating [55]. The sintering of interlamellar cracks and minor changes in the crystal lattice account for this increase in conductivity [63]. Zhang tested eliminated phase transformation as a possible cause for conductivity increase by not exceeding the phase transformation temperature during the heating process. Thus, the conductivity increase was attributed to the evolution of pores due to sintering [64].

Careful examination of TBC before and after being subjected to HCCI combustion will be necessary to ensure complete understanding of and noted combustion phenomena. If the properties of the TBC are found to have changed during a specific round of testing, that effect will have to be taken into account.

1.4 Project Motivation and Objectives

Two issues, which are critical to the commercial application of HCCI, provide motivation for research aimed at developing a comprehensive understanding of the effect of thermal boundary conditions, CCD and artificial TBC on HCCI combustion: (i) The expansion of the HCCI operational range in a dual-mode DI gasoline engine is desired, particularly the low-load limit where the fuel economy benefit over normal SI operation is at a maximum. (ii) Solutions for the robust management of the operational variability imposed by CCD accumulation and burn-off in a practical HCCI engine must be generated.

1.4.1 Characterization of Combustion Chamber Deposits

This work aims to provide further insight into the mechanisms responsible for the effect of CCD on HCCI burn-rates through detailed study of CCD thermal and physical properties both in the engine environment (in-situ) and in a specially constructed thermal radiation chamber (ex-situ) [60].

The radiation chamber was designed to provide a non-destructive environment for quantification of CCD and TBC thermal diffusivities due to lack of an established technique which was applicable to both TBC and CCD [60]. While the radiation chamber has been constructed and initial testing has established the feasibility of ex-situ diffusivity measurements, this work will develop the ex-situ calculation methodology and evaluate the accuracy of the ex-situ diffusivity measurement technique.

Diffusivity values measured in the radiation chamber will be compared to diffusivities obtained within the engine to promote an understanding of the mechanisms responsible for the observed effects of CCD on HCCI combustion. In particular, the comparison will isolate any morphological impact of fuel absorption/desorption into the pores of the CCD layer from the purely thermal effect of the CCD layer.

1.4.2 Assess the Impact of Thermal Barrier Coatings on Combustion Chamber Deposit Accumulation and Homogeneous Charge Compression Ignition Operability

A portion of this research will evaluate the potential of thermal barrier coatings to minimize the uncontrolled shifting of the HCCI operability domain due to CCD formation and subsequent burn-off. The HCCI engine piston top will be covered with a ceramic layer. Then, engine experiments will be combined with an ex-situ investigation of TBC properties to provide comprehensive insight into the magnitude and nature of the TBC's impact on HCCI combustion. In addition, the impact of the TBC on CCD accumulation will be explored.

CHAPTER 2

HCCI EXPERIMENTAL APPARATUS AND PROCESSING METHODOLOGY

Testing with an HCCI engine is a significant portion of this work. The following chapter serves to familiarize the reader with the HCCI experimental apparatus and the associated data processing methodology.

2.1 Engine Apparatus

The engine utilized for this investigation was provided by General Motors as part of the General Motors – University of Michigan Collaborative Research Lab. The crank case used was a Ricardo L850 Hydra. The jug, bore, crank, piston and cylinder head components are based on the GM 2.2 liter four cylinder Quad 4 engine. Table 2.1 lists the dimensions and specifications for the major engine components where 0ºCA is at TDC compression.

Figure 2.1 shows the aluminum head and piston used for this investigation. The head is a four valve pent-roof configuration with a central spark plug, side injector, pressure transducer access and two instrumentation ports, H1 and H2, which can accommodate heat flux probes for this investigation. The aluminum piston is a shallow bowl type with a substantial squish region between the piston and head probe location H1.

Engine	4 valve single cylinder
Bore / Stroke	86.0 / 94.6mm
Displacement	0.5495 liter
Connecting Rod Length	152.2 mm
Piston Pin Offset	0.8mm
Compression Ratio	12.5
IVO / IVC	346° ATDC / 128° BTDC*
Main EVO / EVC	130° ATDC / 352° BTDC*
2nd EVO / EVC	326° BTDC / 189° BTDC*
Injector Type	Bosch 70° Spray Cone Angle with 20° Offset

Table 2.1 – HCCI engine specifications

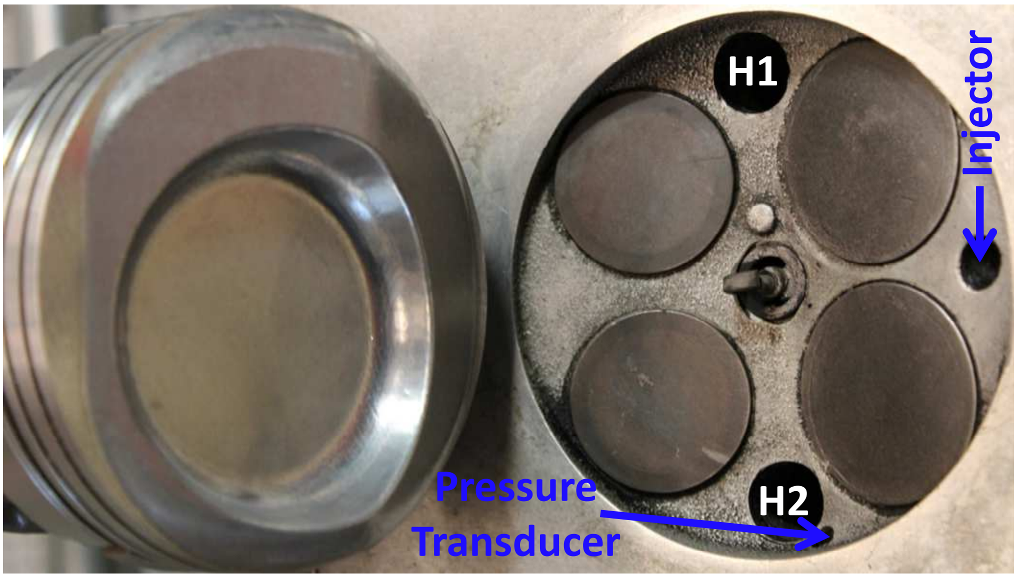

Figure 2-1 – The HCCI piston and cylinder head

A schematic of the engine and its associated sub-systems is shown in Figure 2-2 [39]. This remainder of this section outlines the main features of these sub-systems.

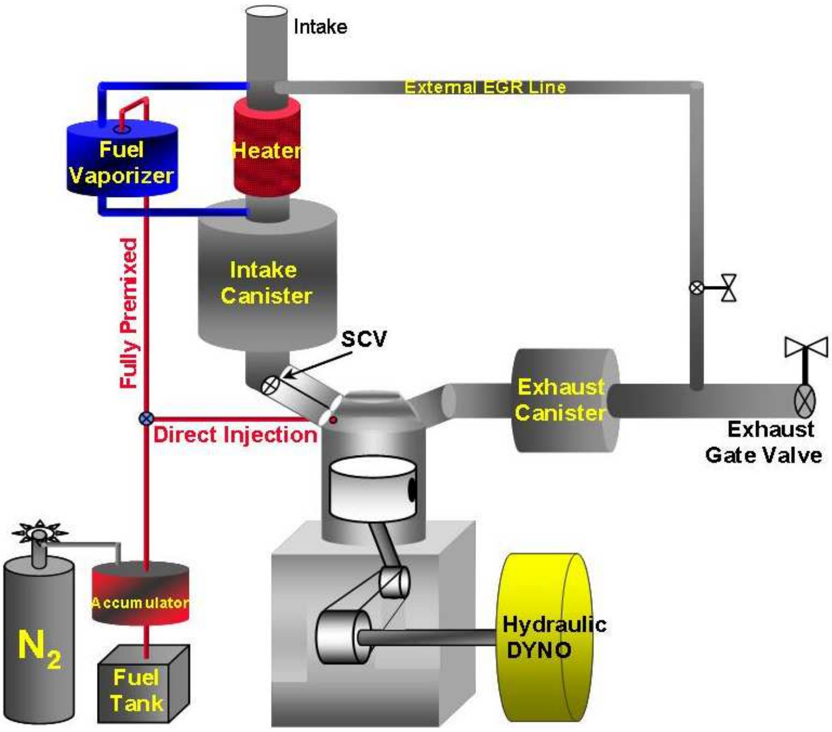

Figure 2-2 – Schematic of the engine sub-systems [39]

Intake Air System

Compressed shop air was controlled with a pneumatic regulator to atmospheric pressure for engine operational. The air passed through a Fox Thermal Instruments FT2 flowmeter, which provided the mass air flow measurements for this investigation. The accuracy of the meter is defined as +/-0.1% of the reading or +/-0.2% of full scale [70]. For this investigation, the error in air flow is +/-0.1 g/s.

The air was then routed into a plenum to dampen pressure oscillations. The air was heated inside the intake plenum to provide an intake temperature of 90ºC by means of flexible silicone heaters wrapped around the plenum. The air temperature was controlled by Omega PID controllers utilizing an intake temperature measured in the runner.

The intake runner divides into two discrete streams to supply air to both the intake valves. A swirl control butterfly valve is located in one of the runner streams to control the relative amounts of air flow going through each intake port, altering the swirl conditions in the chamber. For this investigation, the swirl control valve, SCV, was set to fully open.

Exhaust System

An additional lobe on the exhaust cam profile, shown in Figure 2-3, was utilized in combination with a fixed back pressure of 1.05bar to provide hot internal residual and supply the thermal energy necessary for HCCI combustion. The back pressure was obtained through adjustment of a gate valve placed on the downstream side of the oscillation dampening exhaust plenum.

Figure 2-4 shows the valve lift profiles obtained from this hardware and illustrates the secondary exhaust lift, which allows internal residual to be re-breathed with the help of elevated exhaust backpressure. The backpressure forces exhaust gases into the chamber through the open exhaust valves during the intake stroke.

An ETAS LA4 Lambda Meter is installed in the exhaust plenum to provide real-time air to fuel ratio measurements. The device is capable of measuring air to fuel ratios in the range of 0.7 - 32.767 with an accuracy of +/-1.5% or O_2 concentrations from 0-24.41% with a 2ms response time [71].

An unheated external exhaust gas recirculation loop branches from the exhaust after the plenum but before the backpressure controlling gate valve to transport pressurize exhaust gases back to the intake stream. Although the induction of cool exhaust residuals through the intake stream is a useful to for limiting pressure rise rates during combustion, no external exhaust gas recirculation was used in this study.

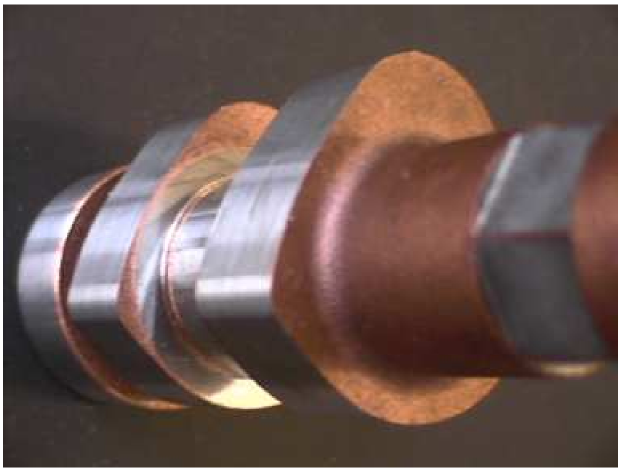

Figure 2-3 – Additional lobe of the rebreathe exhaust cam

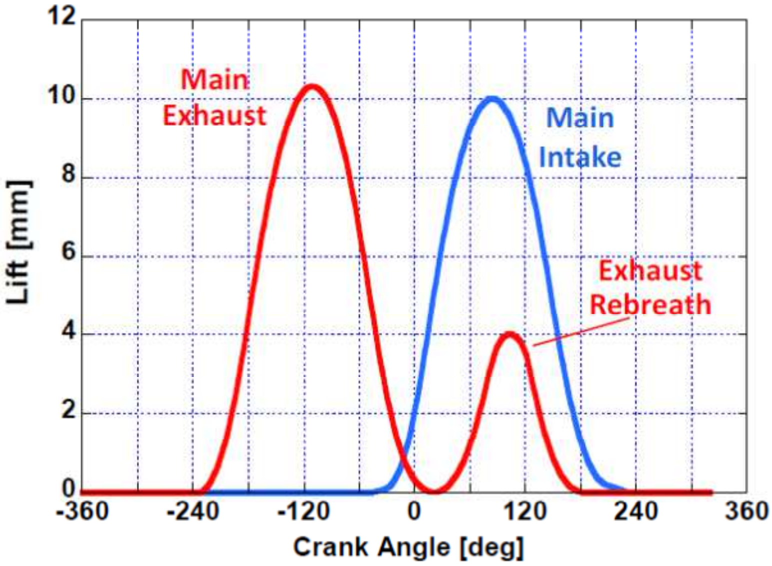

Figure 2-4 – HCCI valve profiles

Ignition System

The HCCI operation scheme for this engine utilizes a large quantity of hot internal residual from the exhaust rebreathe valve scheme. The use of rebreathed residual necessitated the utilization of a spark for the first few cycles until the internal residual became hot enough to sustain combustion when combined with the heated intake stream. The spark timing and dwell were controlled with the PCESC setpoint controller provided by General Motors. For the purpose of this investigation, the spark was left on during all testing. The use of spark during HCCI combustion has been previously shown to have no measureable impact on combustion within the operability range of interest [13].

Fuel System

The fuel vaporizer shown in Figure 2-2 is utilized to evaporate the fuel mass before induction into the intake plenum during fully premixed charge preparation. However, for this investigation the fuel was delivered to the combustion chamber by means of direct injection. As shown in Table 2.1, the injector used in the study was a single nozzle Bosch with a 70º cone angle and a 20º offset from the body axis to the center of the spray cone. This offset was necessary due to the side mounting location of the injector within the cylinder head. Figure 2-5 shows a schematic of the spray trajectory relative to the piston and cylinder head [13].

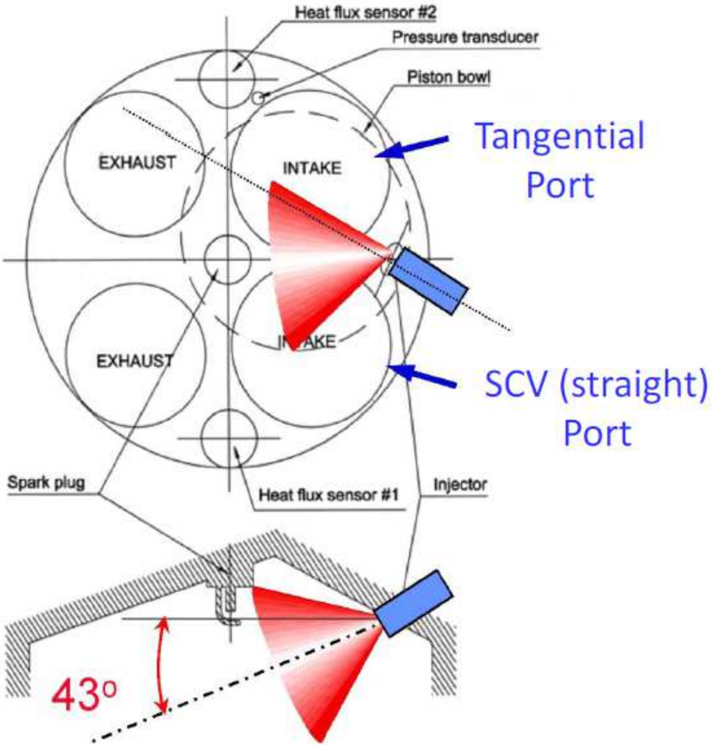

Figure 2-5 – Direct injection spray trajectory schematic [13]

The fuel is pressurized with nitrogen to 10.5MPa via a bladder accumulator system designed by Lee [70]. The injection timing and duration are controlled by the GM PCESC setpoint controller and the Bosch driver.

Test Fuel

The fuel used during the HCCI engine experiments was a controlled research fuel intended to represent 87 octane, non-oxygenated gasoline in a repeatable manner. The RD3-87 fuel was manufactured by Chevron-Phillips to the specifications listed in Table 2.2.

Note that this fuel is completely free of detergents, which is not a realistic representation of commercial gasoline. The majority of commercially available fuels contain solvents to maintain proper fuel flow through injectors. Techron, a solvent manufactured by Chevron-Phillips, was used in a concentration of 0.1ounce/gallon of fuel to replicate commercial levels of solvent in gasoline.

Specific Gravity	0.7373
Carbon [wt%]	85.56
Hydrogen [wt%]	13.64
Oxygen [wt%]	0.0
Molecular Weight	13.9242
Hydrogen Type [Vol. %]	Aromatics 22.5 Olefins 4.1 Saturates 73.4
Research Octane Number	90.8
Motor Octane Number	83.4
Antiknock Index	87.1
Low Heating Value (net)	44.37 MJ/kg
High Heating Value (gross)	47.26 MJ/kg
Stoichiometric A/F	14.6415

Table 2.2 – Specifications for the RD3-87 test gasoline

Dynamometer

The dynamometer used was a MICRO-DYN35 hydraulic dynamometer built by the Electro-Mechanical Associates. The dynamometer could either motor or fire the engine by controlling the pressure differential across a low inertia pump mounted to the engine flywheel.

External Oil and Coolant

The test cell is equipped with stand alone oil and coolant systems. These systems maintain oil and coolant at a temperature of 95ºC via Omega PID controllers which receive temperature feedback from the associated fluid streams. Each system consists of heaters, controllers and heat exchangers, which control the temperature of the working fluid with cold water from the building.

Emissions

Emissions measurements are taken from the exhaust plenum with a HORIBA MEXA-7100DEGR exhaust gas analyzer, Figure 2-6. This system measures CO, CO_2, O_2, HC and NO_x. The exhaust measurements are used in several ways: to provide raw emissions data, to calculate combustion efficiency and to calculate lambda. The calculation methodologies for combustion efficiency and lambda are in accordance with the GM Automotive Test Code Book [73].

The accuracies of the respective HORIBA analyzers are as follows [74]: CO and CO_2 are measured by HORIBA AIA-722 non-dispersive infrared detectors with respective ranges of 2.0vol% and 20.0vol%. The stated uncertainty of these analyzers is +/-1.0% of full scale, which equates to uncertainties of +/-0.02vol% and +/-0.2vol% for CO and CO_2, respectively. O_2 is measured by a MPA-720 magnophneumatic detector with a range of 25vol%. The uncertainty of this analyzer is specified as +/-1.0% of full scale, which translates to an O_2 uncertainty of +/-0.25 vol%. HC are measured by a FIA-725A flame ionization detector, FID, with a range of 6000 ppmC. The stated uncertainty of the FID is +/-1.0% of the full range, giving the HC measurement an uncertainty of 60ppmC. The NO_x is measured by a CLA-720MA chemiluminescence detector with a range of 400ppm. The uncertainty of the NO_x analyzer is +/-2.0% of full scale, which provides a NO_x uncertainty of +/-8ppm.

Figure 2-6 – HORIBA MEXA-7100DEGR emissions bench

2.2 Heat Flux Probes

The crank angle resolved heat flux probes are the same design as implemented in previous studies at the University of Michigan [11]-[13], [39], [69], [79]. The heat flux probes have two coaxial J-type thermocouple junctions and are constructed by Medtherm Corporation, Figure 2-7. One thermocouple junction is created by a vacuum deposited plating of constantan over a thin wire of iron, creating a measurement surface flush with the combustion chamber. The second or backside junction, which is not shown in the figure, is located 4mm behind this surface junction, enabling heat flux calculations.

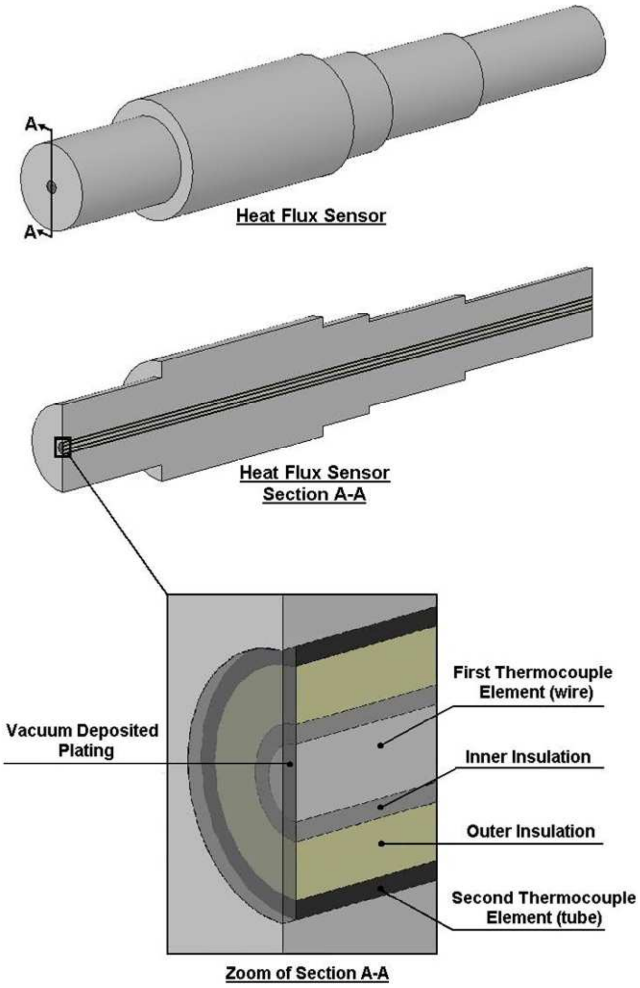

Figure 2-7 – Heat flux probe schematic

The temperature measurement surface of the heat flux probe has very little thermal inertia and a measured response time of less than 10 microseconds [75]. At the engine speeds utilized for this study and a measurement resolution of 0.5CA, the data acquisition acquires a measurement approximately every 40 microseconds. Thus, the response time of the heat flux probes is four times faster than the measurement resolution. Additionally, Güralp [13] showed that the 10 microsecond temperature response time was more than adequate to measure 98% of a step change in temperature within one measurement step (0.5 CA at 2000rpm) with less than 2% error [80].

The accuracy of the heat flux probes is controlled by ISA standards for J-type thermocouples [80], which are met by the Medtherm Corporation during the heat flux probe manufacturing process. The specified maximum error for J-type thermocouples is 2.2ºC or 0.75%, whichever is greater. Since the wall temperatures of the HCCI engine do not exceed 150ºC for the operating conditions of this study [13], the error of the heat flux probes is assumed to be 2.2ºC or ~1.5% of the expected temperature values.

2.3 Deposit Thickness Measurement

Accurate and non-destructive measurement of CCD thickness is vital to the proposed research goals. The thickness is used for the determination of CCD diffusivity and will be great importance in comparing CCD accumulation with and without thermal barrier coatings. Based on the work of Hopwood [49] and Güralp [11]-[13], a Fischer Dualscope MP20 [76] was used to measure the CCD thickness.

For ferrous substrates, the Dualscope utilizes a EGA2H probe, which measures the strength of a magnetic field induced on the substrate material beneath the sample of interest. The strength of this field depends on the distance between the probe and the substrate, allowing determination of the sample thickness. The accuracy of this probe was specified as +/-0.25μm for materials measuring 0-50μm and +/-0.5% for materials measuring 50-500μm [76]. This ferrous probe is used to measure CCD and TBC thicknesses on the steel heat flux probes.

For nonferrous substrates, the Dualscope utilizes a ETA3.3H eddy current probe. As the nonferrous probe is brought near a conductive substrate, the alternating magnetic field establishes an eddy current on the substrate's surface. The distance from the conductive substrate influences the magnitude of the eddy currents. The non-ferrous probe has specified accuracies of +/-0.25μm for materials measuring 0-50μm and +/-0.5% for materials measuring 50-800μm [76]. The non-ferrous probe is utilized to measure CCD and TBC thicknesses on the aluminum piston and cylinder head.

2.4 Data Acquisition Systems

There are two separate data acquisition systems utilized to collect the various signals during engine operation. While some signals can be collected temporally, others must be collected on a crank angle basis.

2.4.1 Time Averaged Data

Signals used to characterize the HCCI operating point or calculate emissions are taken on a time average basis. The time averaged signals include: intake and exhaust manifold pressures, intake and exhaust temperatures, coolant and oil temperatures, air flow, fuel flow, equivalence ratio, and exhaust emissions measurements. All of these signals are received and saved by a LabVIEW data acquisition program that samples at 1Hz. Each data point records the average of 100 consecutive measurements.

2.4.2 Crank Angle Based Data

Several signals must be measured on a crank angle resolved basis to obtain the desired measurement resolution and link the time stamp of each measurement point to a specific crank angle and, therefore, a specific engine volume. The cylinder pressure and heat flux probe signals are all taken at 0.5CA resolution by a14 bit AVL Indiset utilizing IndiCom 2.0 software.

Cylinder pressure is measured by a Kistler 6125A piezo-electric pressure transducer which is guarded from thermal shock by a flame shield. The sensor produces a charge signal that is sent through an AVL Micro IFEM where the signal is converted to a voltage. The Kistler 6125A has a range of 0-250 bar. However, the sensor was calibrated for a more applicable 0-50 bar range using a Kistler Quasistatic Calibrator - Type 6907B. The calibration determined the sensitivity and linearity of the 6125A sensor to be 15.56pC/bar and +/-0.05%, respectively [77].

The heat flux probes measure the surface and backside temperatures in millivolts, requiring amplification by an AVL IFEM before being sent to the data acquisition, DAQ.

2.5 Heat Release Analysis

The general approach used for heat release analysis mirrors that of the project sponsor, General Motors R&D. This approach was based on the work of Gatowski [78] and has been previously employed in investigations by Chang and Güralp [11]-[13], [39], [69], [79].

The basic concept of the HCCI heat release analysis is the treatment of the control volume during the closed portion of the cycle as a single homogenous zone. This assumption allows the chemical heat release to be equated with the internal energy, work, heat loss and mass flow of the control volume as shown in Equation 2.1.

$$\frac{dQ_{chem}}{dt} = \frac{dU_{cv}}{dt} + \frac{dW_{cv}}{dt} + \frac{dQ_{loss}}{dt} + \sum h \frac{dm}{dt} \qquad (2.1)$$

Since the valves are closed during the portion of the cycle for which this analysis is applied, the mass flow term equals zero. Further simplification of Equation 2.1

transforms the internal energy and work terms into expressions utilizing the cylinder wide gamma as shown in Equation 2.2.

$$\frac{dQ_{chem}}{dt} = \frac{1}{\gamma - 1}\left[V\frac{dP}{dt} + \gamma P\frac{dV}{dt}\right] + \frac{dQ_{loss}}{dt} \tag{2.2}$$

The ratio of specific heats, γ, used is this analysis is calculated from the National Institute of Standards and Technology JANAF tables based on the cylinder composition. For this analysis, the residual mass is estimated by a combination of the ideal gas law and a partial pressure analysis, Equation 2.3 where the subscript *IVC* denotes intake valve closing, *int* denotes intake and $T_{residual}$ is the exhaust temperature.

$$m_{residual} = \frac{P_{residual}V_{IVC}}{RT_{residual}} = \frac{V_{IVC}}{RT_{residual}}\left(P_{IVC} - \frac{m_{\mathrm{int}}RT_{\mathrm{int}}}{V_{IVC}}\right) \tag{2.3}$$

The heat loss term of Equation 2.2 was calculated using the HCCI heat transfer correlation developed for this engine by Chang [79]. In order to apply this model, the heat loss term must be expressed as Equation 2.4

$$\frac{dQ_{loss}}{dt} = hA\frac{dT}{dt} \tag{2.4}$$

Chang’s correlation is an adaptation of the Woschni heat transfer correlation and utilizes Equations 2.5 and 2.6.

$$h(t) = \alpha_{scaling}L(t)^{-0.2}P(t)^{0.8}T(t)^{-0.73}v_{tuned}(t)^{0.8} \tag{2.5}$$

$$v_{tuned}(t) = C_1\bar{S}_p + \frac{C_2}{6}\frac{V_dT_r}{P_rV_r}\left(P - P_{motor}\right) \tag{2.6}$$

These variables have the following units: h [W/m^{2}K], L [m], P [kPa], T [K], v [m/s], S_p [m/s], V_d [m^3], T_r [K], V_r [m^3] and P_{motor} [kPa]. The constants are C_1=2.28 and C_2=0.00324 m/s-K. The scaling constant, $\alpha_{scaling}$, is used to ensure that the integrated heat release matches the energy content of the fuel, as calculated from the fuel mass and the lower heating value of the RD3-87. An $\alpha_{scaling}$ value of 11.1 is common for this study.

2.6 Temperature and Heat Flux

The heat flux probes mentioned earlier provide crank angle resolved signals, which are routed out of the engine and into an ice box. The ice box serves as a 0ºC cold junction where the thermocouple signals are transitioned from the iron and constantan wires to copper before being sent to the DAQ for voltage amplification.

The heat flux probe voltage signals have a spurious nature as the original signals were in millivolts. Rather than filter the data, the high frequency noise is removed by application of a Fourier transform. The transform is applied to each individual cycle.

The voltages are converted to temperature and the average found. A separate array is constructed which contains the waveform of the temperature signal by subtracting the average from the temperature at each crank angle. A Fourier transform is then completed using the Fourier coefficients A_n and B_n, the angular velocity, ω, and the harmonic number, n, in Equation 2.7.

$$T_S(t) = \overline{T_S} + \sum_{n=1}^{N} \left[A_n \cos(n\omega t) + B_n \sin(n\omega t) \right] \tag{2.7}$$

Chang [69] determined an appropriate harmonic number for temperature trace reconstruction without CCD accumulation is 40.

The surface temperature, T_S, can then be used with the temperature of the backside junction, T_B, to compute the instantaneous heat flux through each cylinder head probe with Equation 2.8, where k is the conductivity of the heat flux probe (57 W/m-K) and δ is the 4mm distance between the front and backside junctions. Note that the first term on the right hand side is the steady heat flux driven by the difference between average surface and backside temperatures while the second term is the unsteady contribution.

$$\begin{aligned} q_S(t) &= \frac{k}{\delta}\left(\overline{T_S} - \overline{T_B}\right) \\ &\quad + k\sum_{n=1}^{N}\sqrt{\frac{n\omega}{2\alpha}}\left\{A_n\left[\cos(n\omega t) - \sin(n\omega t)\right] + B_n\left[\cos(n\omega t) + \sin(n\omega t)\right]\right\} \end{aligned} \tag{2.8}$$

CHAPTER 3

THE DYNAMIC RADIATION CHAMBER

During in-situ testing, the combustion chamber gases are subject to the thermal impact of CCD while experiencing contact with the CCD morphology. The thermal properties of the CCD layer insulate the heat flux probes, creating a phase lag and reducing the measured sub-CCD peak temperature. In addition, the porous nature of the deposits may provide an additional effect by absorbing and releasing fuel droplets and vapor as porosity has been shown to wield a significant impact on the properties of thermal barrier coatings [55], [63]-[67]. In order to isolate the thermal diffusivity from these morphological effects, the CCD must be tested in a more controlled environment than the engine can provide.

Ex-situ techniques for determining a material's diffusivity such as the flash, 3-omega, and photoacoustic methods [56]-[59], [61], [62] all necessitate the removal of the CCD from the combustion chamber parts. Due to the fragility of the CCD layer, removal from the combustion parts destroys the morphology of the layer, eliminating the basis of comparison between the ex-situ and in-situ diffusivity results. Thus, in order to maintain the integrity of the CCD layer and perform controlled ex-situ testing for thermal properties, a new device and methodology were created [60].

3.1 Radiation Chamber Overview

Throughout this investigation, ex-situ diffusivity testing was conducted within a radiation chamber, which was previously designed [60]. While the construction of the device was not the subject of this work, a brief overview of the chamber’s design, capabilities and its diffusivity measurement principle are included here to assist discussion in future chapters.

The radiation chamber utilizes a 22kW transformer to power a graphite heating element, which serves as a blackbody emitter capable of producing heat flux in the 0.25–1.0 MW/m^2 range as previously measured during HCCI combustion [11]- [13], [39], [69], [79]. The graphite element is enclosed within an inert atmosphere to prevent oxidation/ablation of the graphite [81] and [82]. The design of the graphite element’s resistive path limits the electrical current flow and restricts the graphite temperature to ~2000ºC to avoid the formation of poisonous cyanogen gas [83] and [84].

Following CCD accumulation, the heat flux probes are removed from the cylinder head of the in-situ environment and installed in the wall of the radiation chamber orthogonal to the graphite emitter. A rotating wheel with radial cutouts is positioned between the graphite element and the temperature measurement probes such that the probes are exposed to a pulsed step input of heat flux, Figure 3.1 and Figure 3.2. To ensure the structural stability of this chopping wheel, ex-situ measurement runs are limited to a total time of ~90 seconds depending on the desired wheel rpm. This time includes a 30-40 second element warm up period, which is followed by the collection of data from the impingement of 400 consecutive heat flux pulses on the CCD coated probes at the rate of two pulses per chopping wheel revolution.

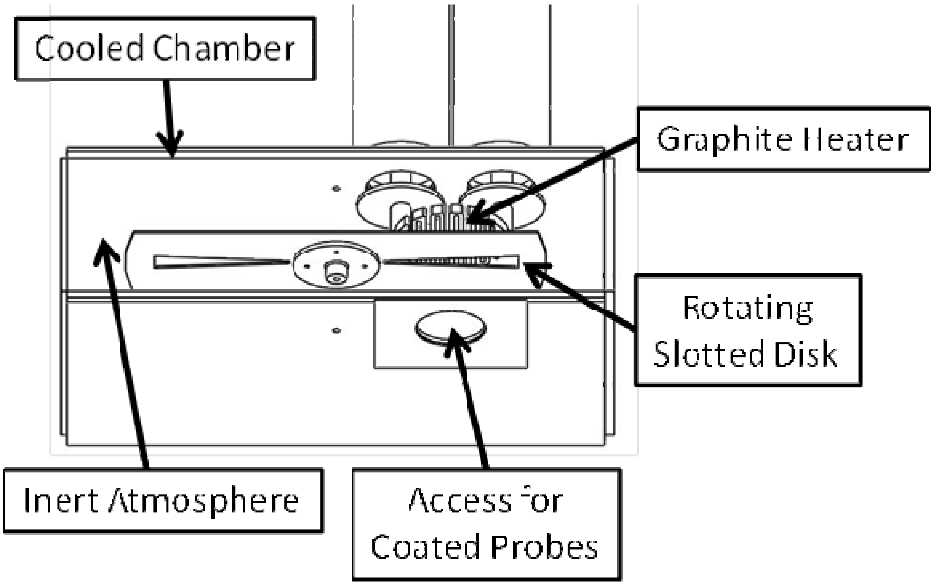

Figure 3.1 – Sectional schematic of the radiation chamber

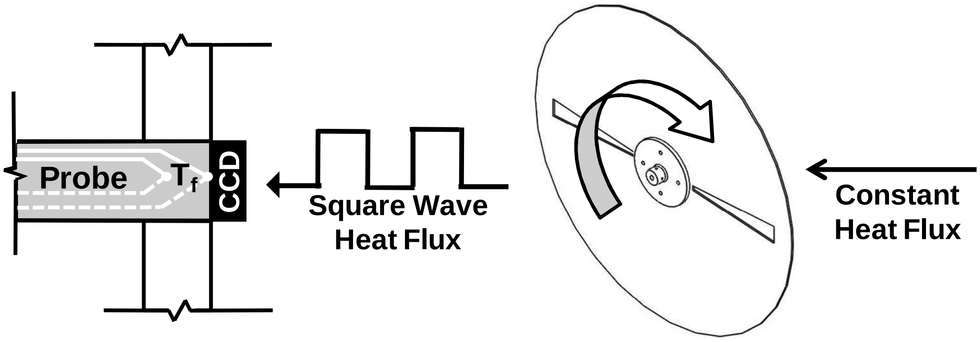

Figure 3.2 – Creation of a pulsed heat flux source via a chopping wheel

Figure 3.3 shows the conceptual response of the temperature probe to the pulsed heat flux. The shape of the temperature response curves are based upon results found by [60] and [86]-[87]. To provide the highest level of comparison to in-situ tests, the ex-situ heat flux and diffusivity calculations utilize the same methodology [49]. This diffusivity measurement methodology compares the temperature response of the clean probe to that of the CCD covered probe, utilizing the sub-CCD peak temperature phase lag in conjunction with the thickness of the CCD layer to determine the thermal diffusivity of the CCD.

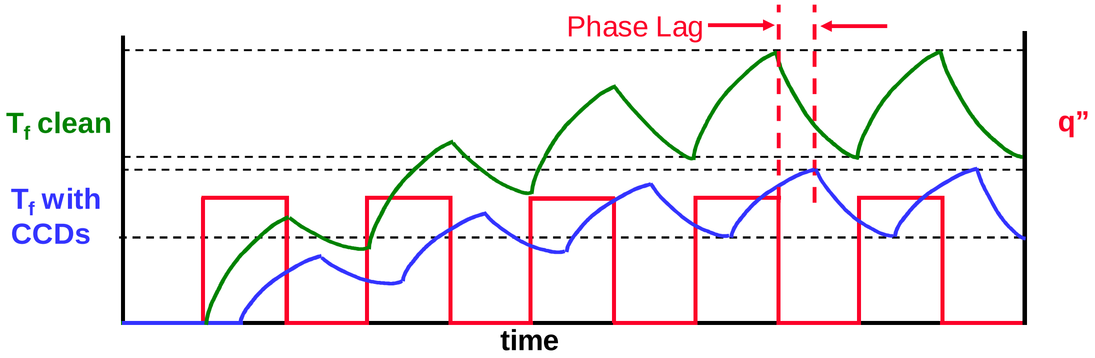

Figure 3.3 – Conceptual response of the probe surface temperature to a pulsed heat flux source when clean and coated with CCD

The design of the radiation chamber allows the ex-situ CCD thermal diffusivity to be compared to the CCD diffusivity determined during in-situ engine operation. The ex-situ and in-situ testing are differentiated by their measurement environments. Comparison of in-situ and ex-situ diffusivity values permits the impacts of the differing environmental factors to be separated from the thermal properties of the CCD layer.

3.2 Improvements to the Radiation Chamber Data Processing

A portion of this work was spent refining the ex-situ data processing methodology. This section addresses the processing of the temperature signals via a Fourier transform with an automated harmonic number selection process designed to protect the ex-situ results from operator bias.

As mentioned earlier, a Fourier transform is applied and the temperature trace is then reconstructed using the inverse Fourier using Equation 2.7, which has been reproduced for convenience here as Equation 3.1. T_{ave} represents the average temperature over the measurement period, A_n and B_n are the Fourier coefficients, ω is the angular velocity, t is time and n is the harmonic number.

$$T(t) = T_{ave} + \sum_{n=1}^{N}[A_n \cos(n\omega t) + B_n sin(n\omega t)] \tag{3.1}$$

Chang [69] found an optimized harmonic number of 40 for in-situ testing, which worked well for reconstructing the sharp features of the clean ex-situ temperature traces. However, due to the attenuated temperature swing and smooth features of temperature traces which are insulated from the heat flux pulse by CCD or any thermal barrier, a harmonic number of 40 replicates too much of the undesired experimental noise.

To determine the best harmonic number for the inverse Fourier reconstruction of the sub-CCD temperature traces, the normalized residual sum of squares has been utilized to indicate the degree of fit at each harmonic number. Equation 3.2 shows the calculation of the residual sum of squares, SS_{err}, for the reconstruction of a temperature trace where T_{raw} is the raw temperature data and $T_{Fourier}$ is the temperature via the inverse Fourier reconstruction.

$$SS_{err} = \sum_{i} \left(T_{raw_i} - T_{Fourier_i}\right)^2 \tag{3.2}$$

Figure 3.4 shows a sample trend of normalized residual sum of squares as the temperature trace is reconstructed using various harmonic numbers. The harmonic number which correlates to the maximum change in slope of the residual sum of squares represents the minimum harmonic number necessary to achieve an adequate temperature reconstruction, Figure 3.5. Increasing the harmonic number beyond this yields ever diminishing returns in terms of degree of fit and increases the amount of noise reintroduced in the temperature reconstruction.

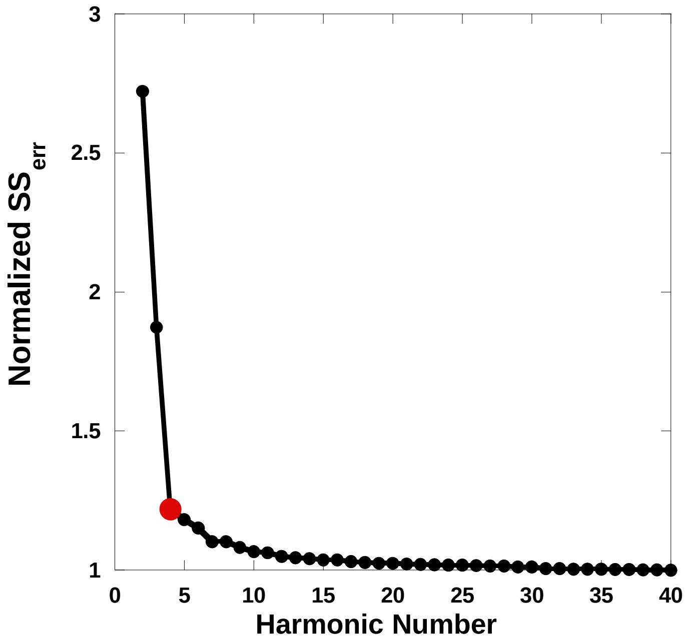

Figure 3.4 – Normalized residual sum of squares for a temperature trace reconstructed with various harmonic numbers illustrating the automatic harmonic selection process

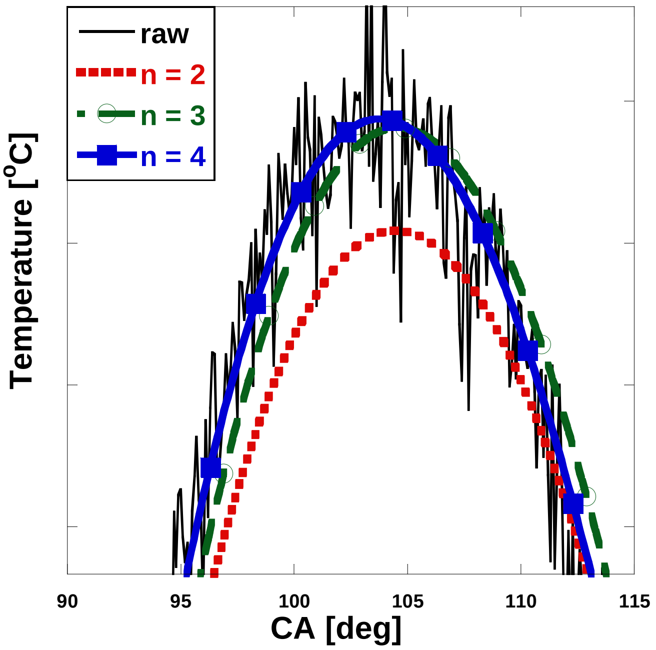

Figure 3.5 – Peak portion of a temperature trace reconstructed with various harmonic numbers where a harmonic number of four was automatically selected

3.3 Dynamic Radiation Chamber Accuracy Evaluation

To evaluate the accuracy of the ex-situ device and methodology, wafers were constructed from alumina, 6061-T6 aluminum, and zirconium for installation over the fast response cylinder head temperature probes used in in-situ studies [11]-[13], [39], [69], [79]. Accepted values of 6061-T6 aluminum diffusivity range by source from 4.84 - $6.9\text{x}10^{-5}$ m^2/s [89]-[91], while the alumina and zirconium wafers have supplier dictated diffusivity ranges of $0.93\text{-}1.08\text{x}10^{-5}$ and $0.7\text{-}1.2\text{x}10^{-6}$ m^2/s, respectively [88]. These diffusivity values overlap with the range of CCD diffusivities previously calculated during HCCI engine studies [11] and with CCD diffusivities calculated during motored laser radiometry experiments for a spark ignition engine [48].

The thermal properties of porous, flame sprayed thermal barrier coatings have been shown to depend on the porosity fraction due to the gas permeability of the porosity [92] and the differences between the thermal properties of the substrate and the material occupying the pores [93]-[95]. The ceramic samples were machined from monoliths to minimize the complications imposed by material porosity.

Multiple thicknesses of each wafer type were constructed to analyze the impact of specimen thickness on measurement accuracy. The wafers were installed over the temperature measurement junction of the heat flux probes via screws in the mounting sleeve surrounding the heat flux probe, Figure 3.6.

During installation, heat sink grease [96] was applied between the wafer and the probe surface to minimize contact resistance. On average, application of the heat sink grease increased the measured thickness of the installed wafer by two micrometers, Table 3.1. The thicknesses and standard deviations displayed for each wafer in Table 3.1 were calculated from twelve measurements using the Dualscope.

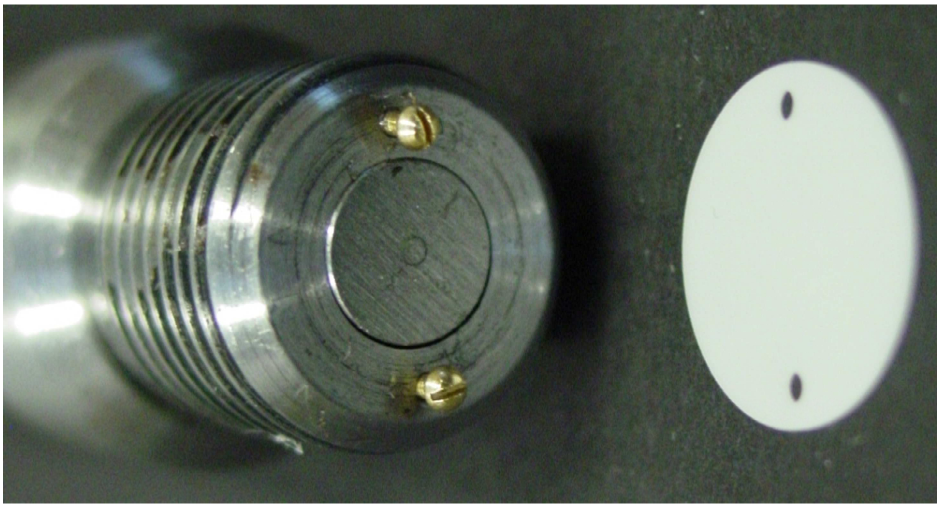

Figure 3.6 – Photograph of a zirconium wafer poised for installation over the heat flux probe and via screws on the probe mounting sleeve

	Thickness/Std Dev [μm]	
Material	**Plain**	**Grease**
Aluminum	544/10	541/14
	1029/17	1024/21
	1595/8	1593/19
	2174/12	2179/12
Zirconium	104/4	108/8
	168/8	172/12
	225/10	224/15
	277/15	282/17
Alumina	104/2	109/7
	167/6	169/11
	223/9	224/15
	274/11	279/16

Table 3.1 – Wafer thicknesses and standard deviations as measured by the Fischer Dualscope both with and without high conductivity heat sink grease between the wafer and the probe surface

3.3.1 The Impact of a Non-Instantaneous Heat Flux Pulse on Ex-Situ Diffusivity

Figure 3.7 shows diffusivity results produced by three thicknesses of aluminum wafer. Three data points are displayed for each wafer thickness at each chopping wheel rpm. Each of these data points is the average of 400 diffusivities individually calculated from the sub-wafer temperature delay of 400 consecutive heat flux pulses. These initial tests with aluminum wafers yielded diffusivity exhibited accuracies which were thickness dependent, and the thinnest wafer specimens experienced the greatest error from the expected value.

During these initial tests, the accuracy of thinner wafers suffered due to the non-instantaneous delivery of the heat flux pulse. The graphite emitter was not a point source emitter of heat flux. As such, the wafer covered probe was exposed to a ramp up in view factor as the radial cutout of the chopping wheel gradually exposed the probe to a greater percentage of element area. More importantly, the probe also experienced a ramp down in view factor as the chopping wheel gradually covered a greater percentage of the graphite element at the end of the pulse event, Figure 3.8.

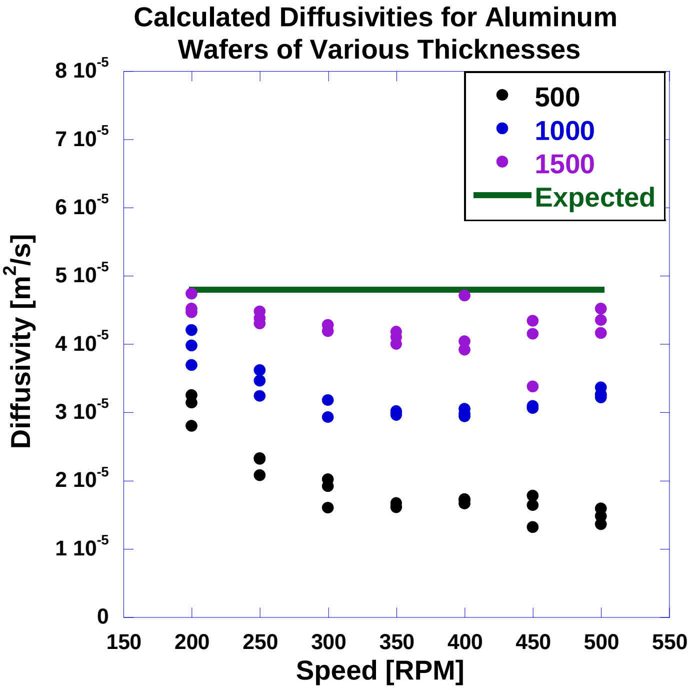

Figure 3.7 – Diffusivities for aluminum wafers of various thicknesses at different chopping disk speeds where the differing wafers are denoted by their respective thicknesses in micrometers

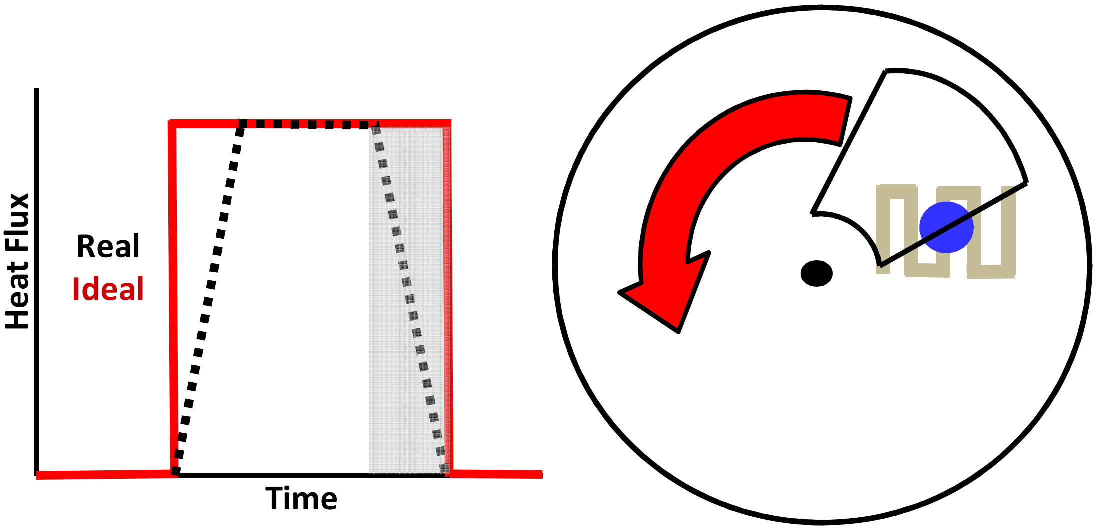

Figure 3.8 – Schematic of the non-instantaneous heat flux pulse (left) produced by the ramp up and ramp down in radiation view factor experienced by the measurement probe as the chopping wheel uncovered and subsequently recovered the line of sight to the graphite element (right)

To quantify the impact of the non-instantaneous nature of the heat flux pulse, a COSMOS finite element model of the heat flux probe, mounting sleeve and installed aluminum wafer was created, Figure 3.9. For this model, contact resistance between the various thicknesses of aluminum wafer and the temperature measurement surface of the heat flux probe was neglected. The cooling provided by the radiation chamber walls was modeled by holding both the outer cylindrical face and angular sealing seat of the mounting sleeve at a constant temperature of 50ºC. The use of a constant temperature on these surfaces was justified by the fact that the cooled wall of the radiation chamber comprised a much larger thermal mass than the probe itself and the selected surfaces were in contact with the wall. Additionally, 50ºC was the mean probe temperature experimentally measured during these initial studies.

The surface of the aluminum wafer was subjected to heat flux profiles of varying shapes each having a peak magnitude consistent with experimental measurements, 0.4 MW/m^2. The three different heat flux profiles utilized in the COSMOS model and their subsequent impact on the response of a bare heat flux probe (“clean”) and a probe covered by an aluminum wafer of 500μm (“500”) are displayed in Figure 3.10. A true square wave heat flux pulse was used as a control while the subsequent heat flux profiles had ramping view factors whose time duration matched 5CA and 10CA of the chopping wheels rotation at 300rpm.

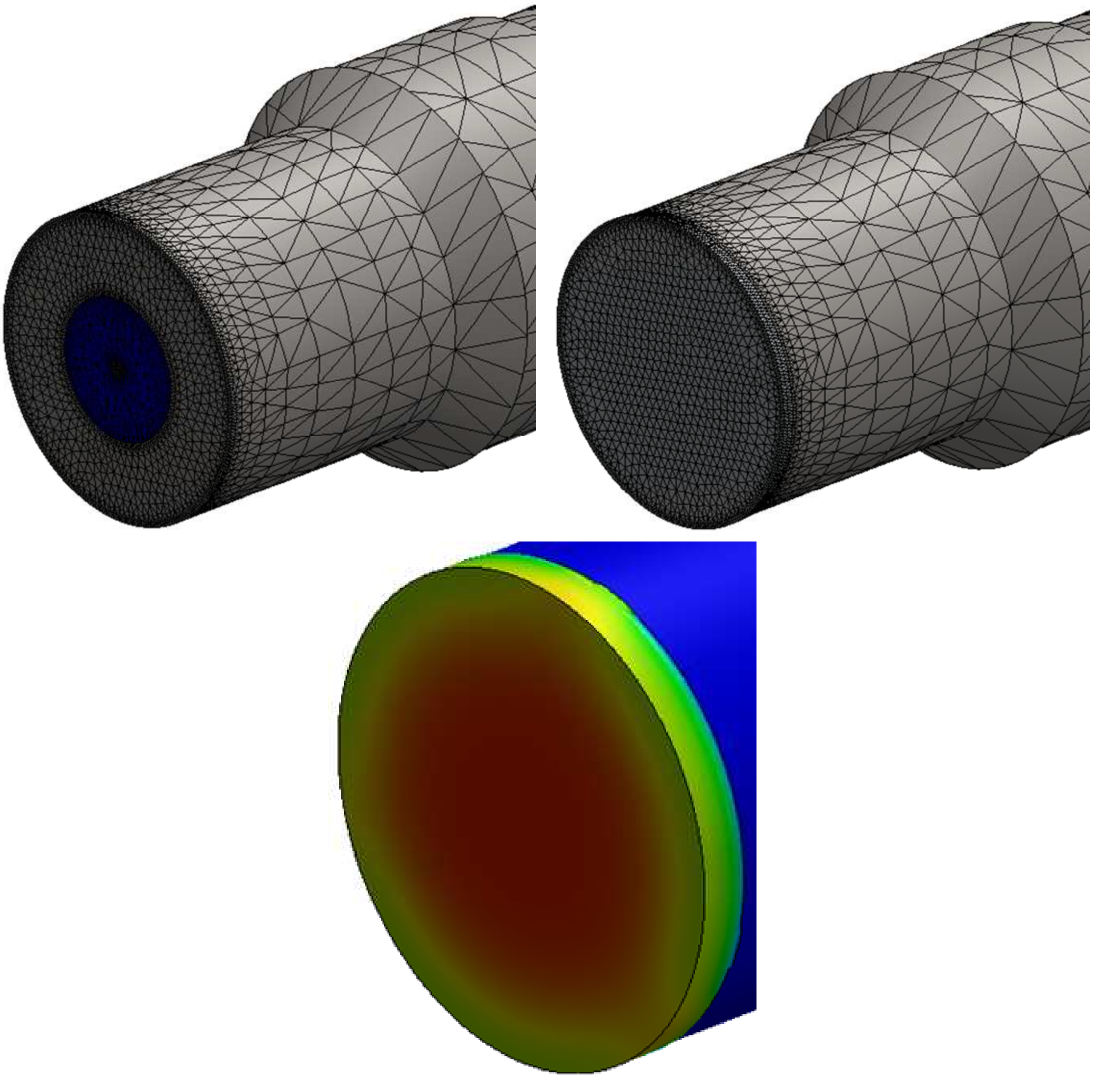

Figure 3.9 – The COSMOS finite element model created of the heat flux probe, mounting sleeve and installed aluminum wafer

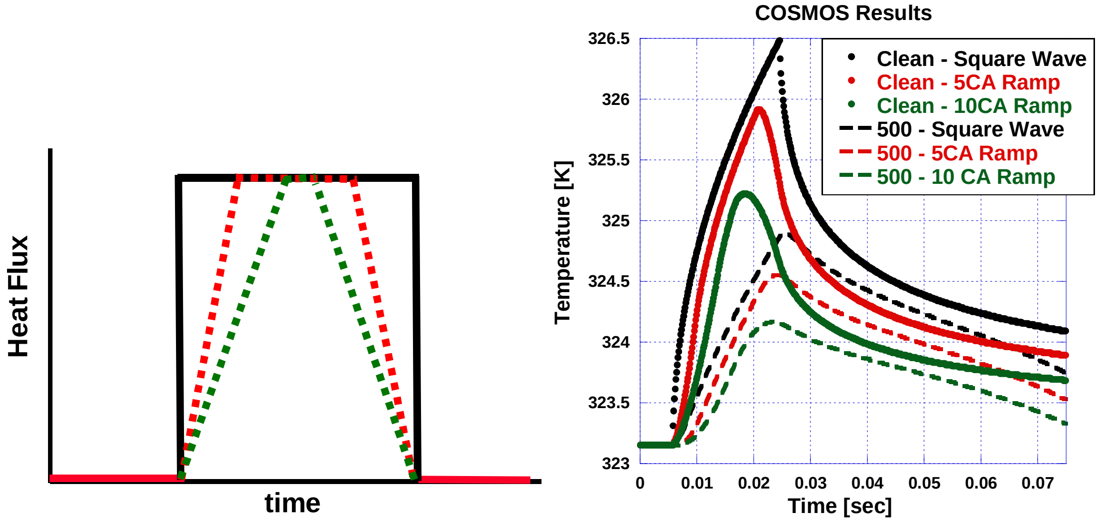

Figure 3.10 – The heat flux profiles utilized in the COSMOS finite element model and the subsequent response of the heat flux probe when both clean and coated with a 500µm aluminum wafer

Both the clean and sub-wafer temperature profiles advanced with increasing heat flux ramp duration. The clean temperature profiles advanced 3.6 and 6.1ms for heat flux profiles with 5CA and 10CA ramps, respectively. However, the respective sub-wafer temperatures advanced only 1.4 and 2.2ms. The result was an increasing phase delay between the clean and sub-wafer temperature profiles producing progressively lower wafer diffusivity values as the heat flux ramp time was increased.

Although the absolute advances in phasing caused by the ramped heat flux profiles were small, 2.2 and 3.9ms for the 5CA and 10CA ramps, respectively, they were large compared to the phase delay of the 500µm wafer when utilizing the square wave heat flux pulse, 0.85ms. The magnitude of diffusivity reductions calculated from the sub-wafer phase delays with the 5CA and 10CA duration ramps applied to the heat flux profiles were 260% and 460%, respectively. Therefore, the impact of a non-instantaneous heat flux pulse accounted for the absolute level of error experimentally observed with the 500µm aluminum wafer.

Thicker aluminum wafers were also tested with the COSMOS model utilizing the same heat flux pulse profiles shown in Figure 3.10. The sub-wafer temperature profiles predicted by the COSMOS model for aluminum wafer thicknesses of 500 and 1500µm are shown in Figure 3.11.

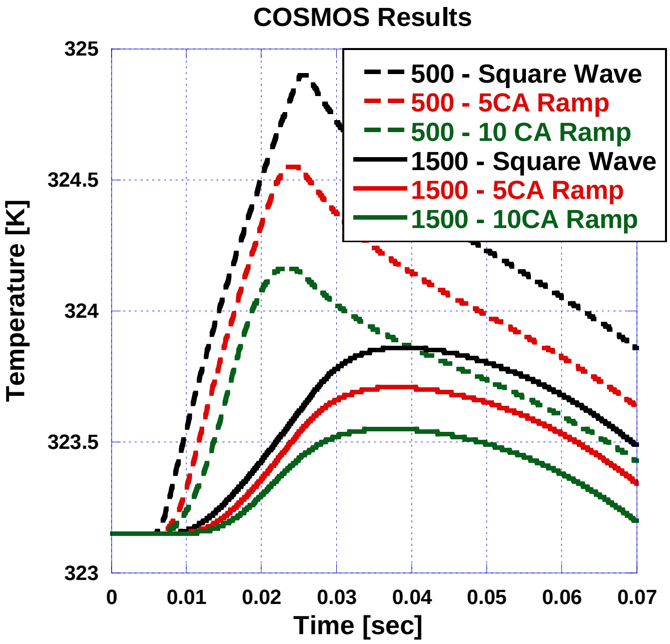

Figure 3.11 – The heat flux probe temperature profiles predicted by the COSMOS model for aluminum wafer thicknesses of 500µm and 1500µm with heat flux pulse profiles of various shape

The sub-wafer temperature profile of 1500µm aluminum wafer also experienced an increase in phasing advance from 1.1 to 1.9ms as the view factor induced ramp time of the heat flux profile increased from 5CA to 10CA, respectively. When combined with the aforementioned advance in the response of the clean probe to ramped heat flux profiles, the phase delay associated with the 1500 µm aluminum wafer increased by 2.5ms for the 5CA ramp and 4.2ms for the 10CA heat flux ramps. While these changes to the absolute phase delay of the 1500µm wafer are greater than those experienced by the 500µm wafer, the ideal phase delay of the 1500µm aluminum wafer, as determined by the COSMOS model with an ideal square wave heat flux profile, was 14.5ms, seventeen times that of the 500µm wafer. Accordingly, the diffusivity reductions associated with the non-instantaneous nature of the heat flux pulses with the 1500µm wafer were only 17% and 30%, respectively, for the 5CA and 10CA heat flux ramps. Thus, COSMOS modeling of the non-instantaneous heat flux pulse has matched the experimental behavior of Figure 3.7 in both the absolute level of diffusivity underprediction and the trend of decreasing diffusivity error with increasing wafer thickness.

To minimize the impact of the non-instantaneous heat flux pulse on the ex-situ results, the radial cutouts of the chopping wheel were tripled in size and the wheel was spun at three times the previous speeds, Figure 3.12. This hardware alteration maintained the heat flux pulse duration while reducing the time domain duration of the view factor ramp up and ramp down process. All ex-situ testing reported in the subsequent sections of this work utilized this upgraded hardware.

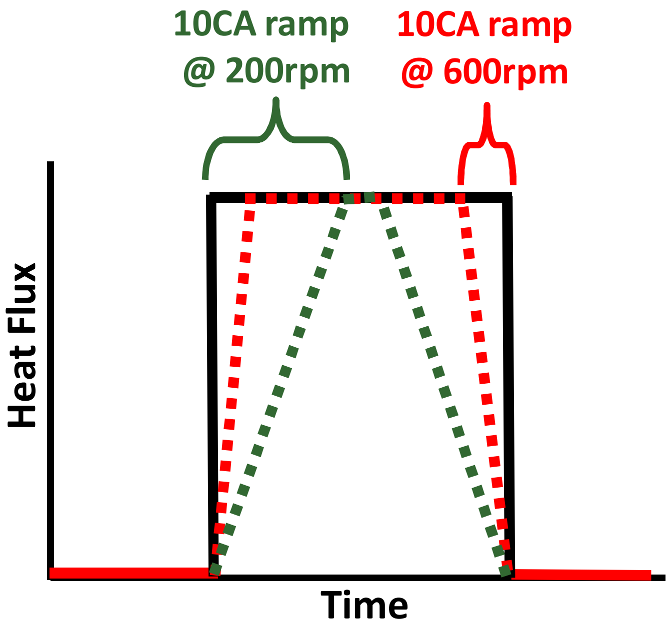

Figure 3.12 – Impact of increasing the radial cutouts and speed of the chopping wheel by a factor of three on the heat flux pulse profile

3.3.2 Impact of Sample Thickness and Chopping Wheel Speed on Ex-Situ Diffusivity

The five different thicknesses of 6061-T6 aluminum produce an average diffusivity value of $4.7\text{x}10^{-5}$ m^2/s, three percent less than the lower bound of the expected range ($4.84\text{x}10^{-5}$ m^2/s) and twenty percent less than the mean of the expected range ($5.87\text{x}10^{-5}$ m^2/s) . Figure 3.13 shows the calculated diffusivities for all five aluminum wafer thicknesses. The ex-situ diffusivity values exhibit no dependence on sample thickness. Each data point in Figure 3.13 represents the average of 400 individually calculated diffusivity values. There are three 400 pulse data points displayed for each wafer thickness at each chopping disk speed. The average of the ~38000 diffusivity values calculated with the aluminum wafers has been plotted as horizontal line and shown relative to the mean of the expected range.

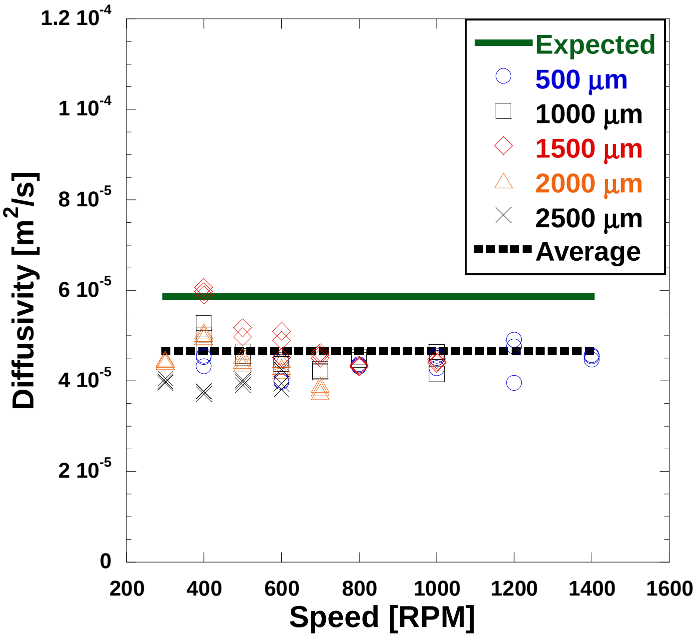

Figure 3.13 – Diffusivities for aluminum wafers of various thicknesses at different chopping disk speeds

Higher rotational speeds equate to shorter heat flux exposure times and temperature swings of lower amplitude. The relative flatness of the temperature profile for short heat flux pulse durations hampers the selection of a maximum temperature, Figure 3.14. In addition, increasing wafer thickness at any one speed further reduces the sub-wafer temperature swing, Figure 3.15. Thus, measurements with thick samples at high speed are avoided as selection of a maximum temperature becomes difficult.

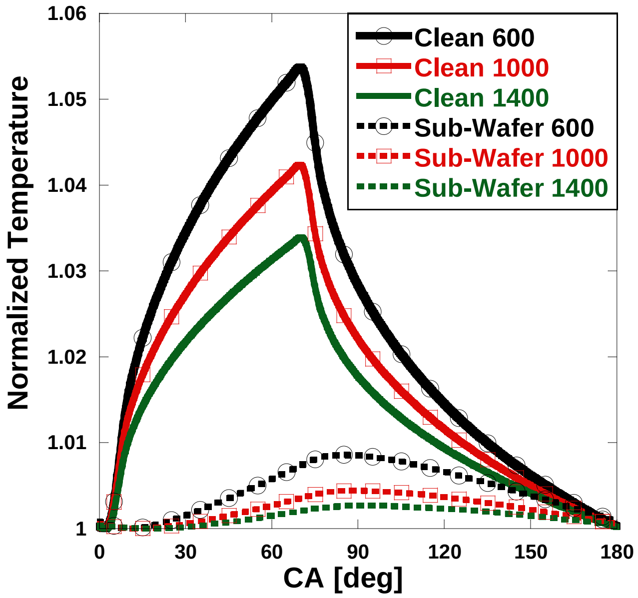

Figure 3.14 – Normalized temperature traces of a clean probe and a probe covered with a 500µm aluminum wafer at various chopping disk speeds (in rpm)

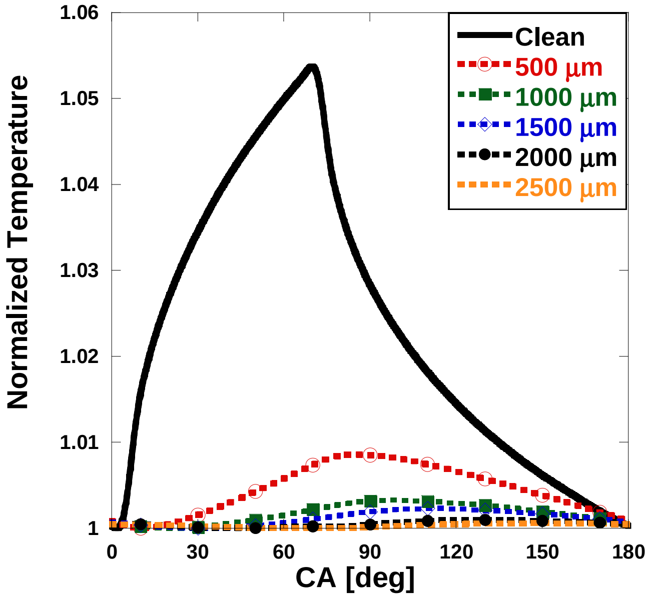

Figure 3.15 – Normalized temperature trace for a clean probe and sub-wafer temperature traces for various aluminum wafer thicknesses at a constant chopping disk speed of 600 rpm exhibiting the loss of amplitude for large thicknesses

3.3.3 Impact of Radiation Transparency on Ex-Situ Diffusivity

Initial tests with the alumina and zirconium wafers revealed a partial transparency of these materials to the radiative heat flux. The sub-wafer temperature profile shown in Figure 3.16 had no measurable phase delay relative to the clean temperature signal. Additionally, the heat flux profiles of clean and wafer covered probes exhibited nearly identical phasing, Figure 3.16. Other researchers have noted the semi-transparent behavior of similar ceramics [96]-[99].

Pores within a ceramic layer can significantly alter the heat transfer behavior of a coating by absorbing the transmitted radiation and acting as internal radiation sources, increasing the total heat transfer through the coating [100]. However, the monolithic construction of the calibration wafers used in this study minimizes the included porosity. In addition, internal radiation within a ceramic layer has been proven minimal at temperatures below 400ºC by [100] and [101]. Thus for the temperature ranges of this work, the ex-situ radiation pulse transfers heat directly through the wafer sample without graphite, and the influence of porous absorption and re-radiation is negligible.

Application of a graphite aerosol [100] to the surface of the ceramic wafers created an opaque layer which minimized transmission and reflection of the incident radiation. Figure 3.16 shows sub-wafer temperature and heat flux traces with the graphite aerosol applied. A clear phase delay is now present in both the sub-wafer temperature and heat flux profiles suggesting that transmission has been reduced.

The mean sub-wafer temperature increased by 7.5ºC from 78.2 to 85.7ºC due to graphite application, creating the higher peak heat transfer exhibited by the “sub-wafer with graphite” heat flux trace in Figure 3.16. While ceramics have been shown to exhibit a decrease in reflectivity as temperatures increase beyond 1300K [100] and [102], the ex-situ environment kept the ceramic temperatures under 400K, well below the 1300K temperature threshold. Therefore, the 33% increase in absorbed radiation with graphite applied was attributed to reduced reflectivity at the ceramic surface due to the graphite application and not to changes in the optical properties of the ceramic itself.

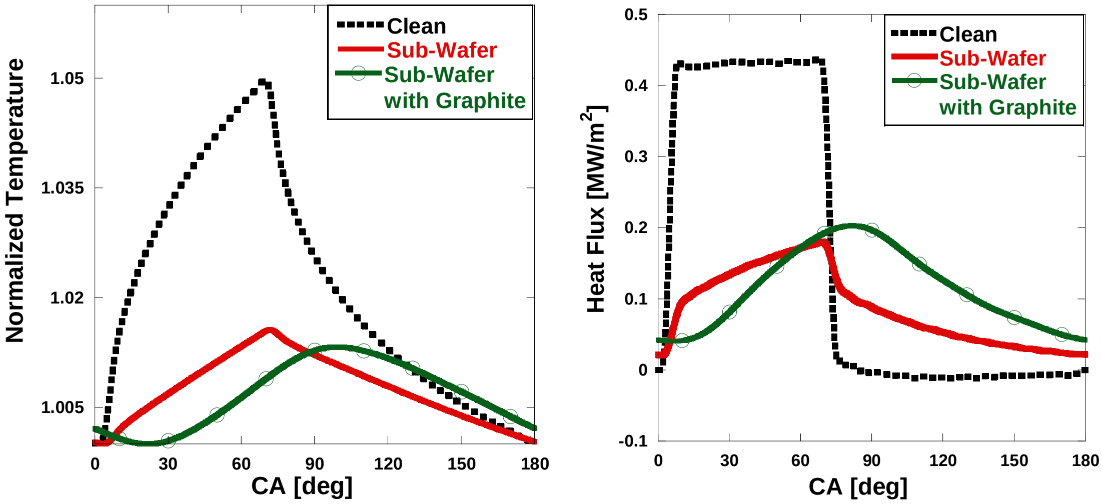

Figure 3.16 – Temperature profiles (left) and heat flux profiles (right) of a clean probe and a probe covered with a ceramic wafer exhibiting transparency to the radiation source and minimization of that transparency via the application of aerosol graphite

The influence of aerosol graphite on the response of a bare heat flux probe (a probe without a wafer covering the junction) was also tested. Figure 3.17 shows the measured temperature traces for a bare heat flux probe and a probe coated with aerosol graphite. The graphite coated probe experienced a larger temperature swing due to increased radiation absorption of the probe surface. No phasing change was measured due to the graphite application indicating that the phasing of the graphite coated temperature trace is within 12µs of the phasing of the bare temperature trace. (The temporal resolution for a chopping wheel speed of 1400rpm with 0.1CA resolution is 12µs.) For the comparison shown in Figure 3.16 and throughout this work, the traces named “clean” denote the response of a heat flux probe with aerosol graphite applied to its surface but without a calibration wafer, CCD or thermal barrier coating covering the temperature measurement junction.

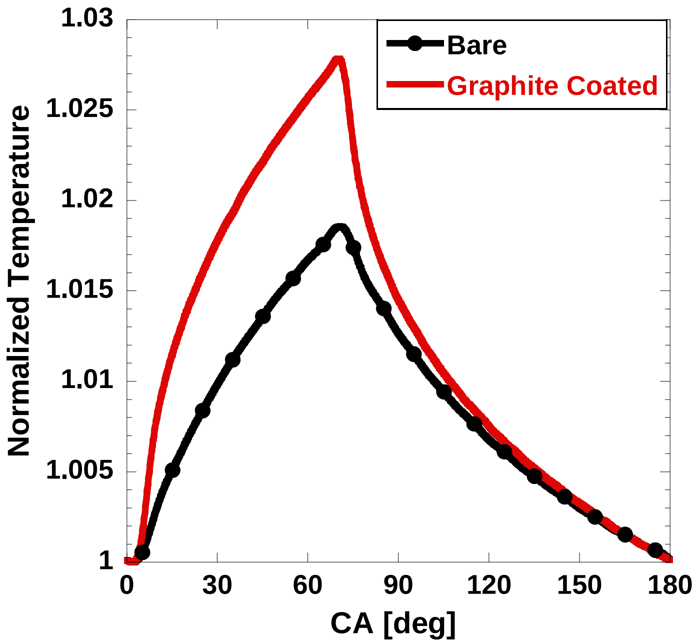

Figure 3.17 – Normalized temperature profiles depicting the influence of graphite aerosol on the response of a clean heat flux probe

The application of the graphite to the surface of a bare heat flux probe accumulates an average thickness of 0.8µm with a standard deviation of 0.5µm from a sample of twelve Dualscope thickness measurements. Additionally, the impact of graphite application on the measured wafer thicknesses is shown in Table 3.2. The average thicknesses and standard deviations displayed for each wafer are from twelve Dualscope thickness measurements. On average, the application of graphite to the wafer surface adds 3µm to the measured wafer thickness.

	Thickness/Standard Deviation [μm]		
Material	**Plain**	**Grease**	**Grease and Graphite**
Aluminum	544/10	541/14	551/12
	1029/17	1024/21	1039/21
	1595/8	1593/19	1595/21
	2174/12	2179/12	2174/14
Zirconium	104/4	108/8	108/9
	168/8	172/12	172/11
	225/10	224/15	228/17
	277/15	282/17	279/16
Alumina	104/2	109/7	109/8
	167/6	169/11	170/12
	223/9	224/15	227/16
	274/11	279/16	282/17

Table 3.2 – The impact of heat sink grease sub-layer and graphite surface treatment on installed wafer thicknesses as measured by the Fischer Dualscope

3.3.4 Ex-Situ Diffusivity Accuracy with Ceramic Materials

The alumina and zirconium wafers were fabricated with nominal thicknesses of 100, 150, 200, and 250μm. The sub-wafer temperature traces for like wafer thicknesses at the same speed are compared in Figure 3.18. As the diffusivity of the wafer material decreases, the sub-wafer temperature swing decreases and limits the ability to ascertain the peak temperature. Thus, materials with lower diffusivities have a lower speed threshold for accurate measurements.

The diffusivities obtained for all three wafer materials are shown in Figure 3.19. The different shapes and colors of the points plotted for any one material correspond to different wafer thicknesses. (There are five thicknesses of aluminum wafer and four thicknesses each for alumina and zirconium.) Each point plotted is obtained from 400 individual diffusivity values calculated from 400 sequential temperature traces.

The average diffusivities of each material are shown as horizontal dashed lines and were computed from the individual pulse diffusivities at all thicknesses and all speeds. For comparison purposes, the solid lines show the mean diffusivity of the expected range for each material.

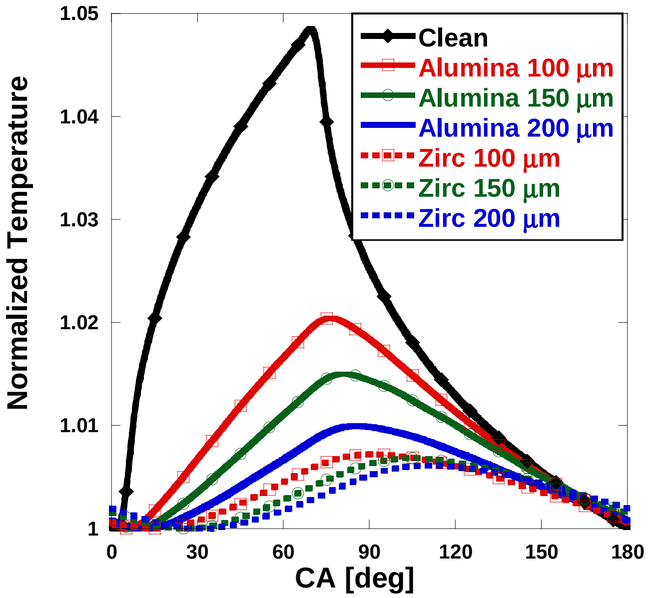

Figure 3.18 – Clean and sub-wafer temperature traces for like thicknesses of alumina and zirconium ceramic at a constant chopping disk speed of 600 rpm

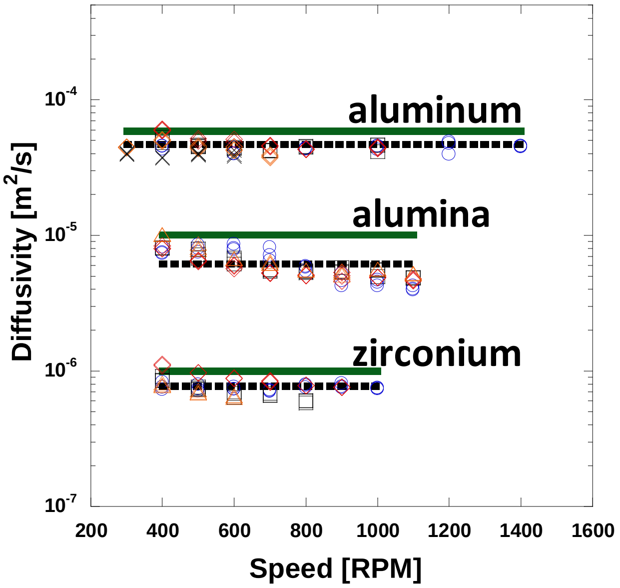

Figure 3.19 – Diffusivities for all thicknesses of the three wafer materials and their sample averages (black dashed lines) relative to the mean of the expected diffusivity range for each material (solid green lines)

The ex-situ diffusivity values show no trend with sample thickness for any material tested. The radiation chamber underpredicts the average diffusivities for aluminum, alumina and zirconium. The sample average diffusivity for zirconium is 0.80×10^{-6} m^2/s which is fourteen percent greater than the lower bound of the expected range (0.70×10^{-6} m^2/s) but sixteen percent lower than the mean of the expected range (0.95×10^{-6} m^2/s). The alumina results fared worse on a comparative basis due to the relatively narrow range of expected value for the alumina wafers. The sample average diffusivity value, 6.4×10^{-6} m^2/s, is thirty one percent below the lower bound of the expected range (9.3×10^{-6} m^2/s) and thirty six percent below the mean of the expected range (1.0×10^{-5} m^2/s). Figure 3.20 illustrates the comparison of the sample averages calculated from the radiation chamber with the expected diffusivity values. The error bars on the radiation chamber results represent the standard deviation of the ~38000 individual diffusivities calculated for each material while the error bars on the expected data depict the extremes of the expected value range for each material.

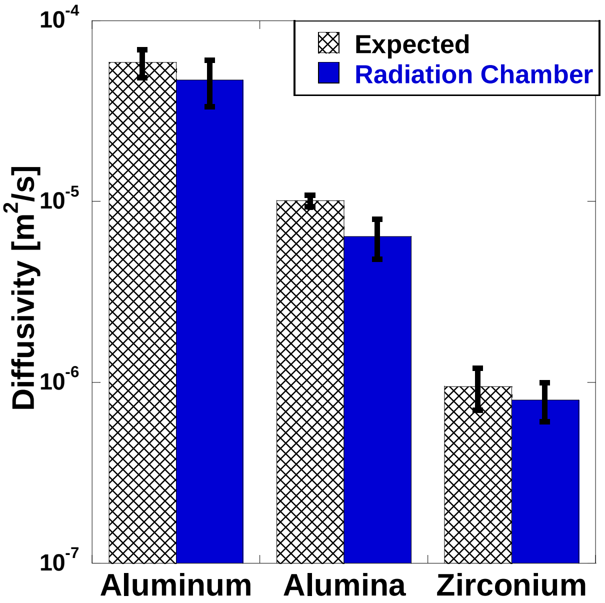

Figure 3.20 – Ex-situ diffusivities and their standard deviations compared to the mean expected values and the range of expected values as provided by various texts

While the heat sink grease promotes consistent contact at the wafer-probe interface and minimizes air gaps, the conductivity of the thermal grease is only 0.75 W/mK [96], which is less than the conductivity for all the wafer materials [88]. Thus, the thin layer of grease beneath each wafer (2μm on average) increases the measured temperature phase lag and creates a consistent diffusivity underprediction for all wafers.

3.3.5 Accuracy Evaluation Conclusions

A thermal radiation chamber has been developed for the non destructive determination of CCD thermal diffusivity. To demonstrate the accuracy of the device and methodology, wafers of various thicknesses were fabricated from materials of known thermal properties and installed over the surface temperature measurement junction of a heat flux probe. Measures were taken to minimize contact resistance, surface reflection, and radiation transparency of the calibration materials.

The thickest calibration wafers yielded smaller data sets during sweeps of heat flux pulse duration due to the increasing difficulty in ascertaining the peak temperatures as the heat flux impulse durations were shortened. Likewise, materials of lower diffusivity reduce the temperature swing measured beneath the material and limit the sample size during pulse duration sweeps.

With these tendencies as guidelines for data collection, the diffusivities calculated by the device and methodology proved to be independent of material thickness. The wafer diffusivities exhibited a slight but consistent underprediction for all three materials tested. Residual contact resistance remaining after application of the heat flux grease at the wafer-probe junction increases the measured temperature phase lag, decreasing the diffusivities of all the calibration wafers.

CHAPTER 4

THERMAL DIFFUSIVITY OF COMBUSTION CHAMBER DEPOSITS

The improvements to the dynamic radiation chamber's measurement technique and the establishment of its accuracy in the previous chapter allow confident collection of ex-situ CCD diffusivity data for various sample thicknesses during a passive conditioning cycle. The environmental differences between the ex-situ and in-situ setups can then be exploited to examine the impact of CCD morphology on the diffusivity of CCD through a comparison of the ex-situ and in-situ diffusivity values.

4.1 Analysis of Combustion Chamber Deposit Accumulation

A passive conditioning cycle was conducted by allowing the engine to operate at a single point within the HCCI operational space (11mg$_{fuel}$, 20:1 A/F, WOT, 90°C T$_{intake}$, 95°C T$_{oil}$ and T$_{coolant}$) with the RD3-87 reference fuel described in Chapter 2. This passive operation allows analysis of CCD accumulated over time, which have not been subjected to the drive cycle dependent impact of burn-off and re-accumulation.

During the passive conditioning cycle, the cylinder head heat flux probes were periodically removed and tested within the radiation chamber to determine the ex-situ diffusivity. Table 4.1 shows the points of stoppage during the passive conditioning cycle and the corresponding CCD thicknesses on each cylinder head probe as measured by the Fischer Dualscope. Twelve thickness measurements were obtained in a circular pattern on the probe area immediately surrounding the measurement surface and averaged. The standard deviation of these measurements is also reported in Table 4.1.

Obtaining thickness measurements directly on the temperature measurement surfaces of the cylinder head heat flux probes was intentionally avoided to protect this crucial portion of CCD morphology from contact with the Fischer Dualscope. However, the thicknesses averaged from the immediately surrounding area of the probe housing have low standard deviations, providing sufficient confidence that the CCD thickness at the measurement junction has been accurately represented.

Engine Run Time [hours]	Probe Location	Combustion Chamber Deposit Thickness [μm]	Std. Dev. [μm]	Std. Dev. [%]
10	H1	24	4	17
10	H2	23	3	13
14	H1	28	5	18
14	H2	25	4	16
18	H1	29	3	10
18	H2	27	2	7
22	H1	31	4	13
22	H2	31	3	10
26	H1	33	4	12
26	H2	41	6	15
30	H1	40	5	13
30	H2	48	3	6
33	H1	42	3	7
33	H2	64	5	8
35	H1	50	3	6
35	H2	66	6	9

Table 4.1 – CCD thicknesses and standard deviations at the various stopping points of the passive conditioning cycle

Figure 4.1 and Figure 4.2 show the CCD accumulation at each of the stopping points within the passive conditioning cycle. The initial stage of CCD growth (through ~30μm) generates a visually sparse CCD layer with round nodules protruding from the surface. This protruding topography is yellow-brown in color when compared to the typically grey-black CCD and can most clearly be seen in the 25, 27, and 31μm photos within Figure 4.2.

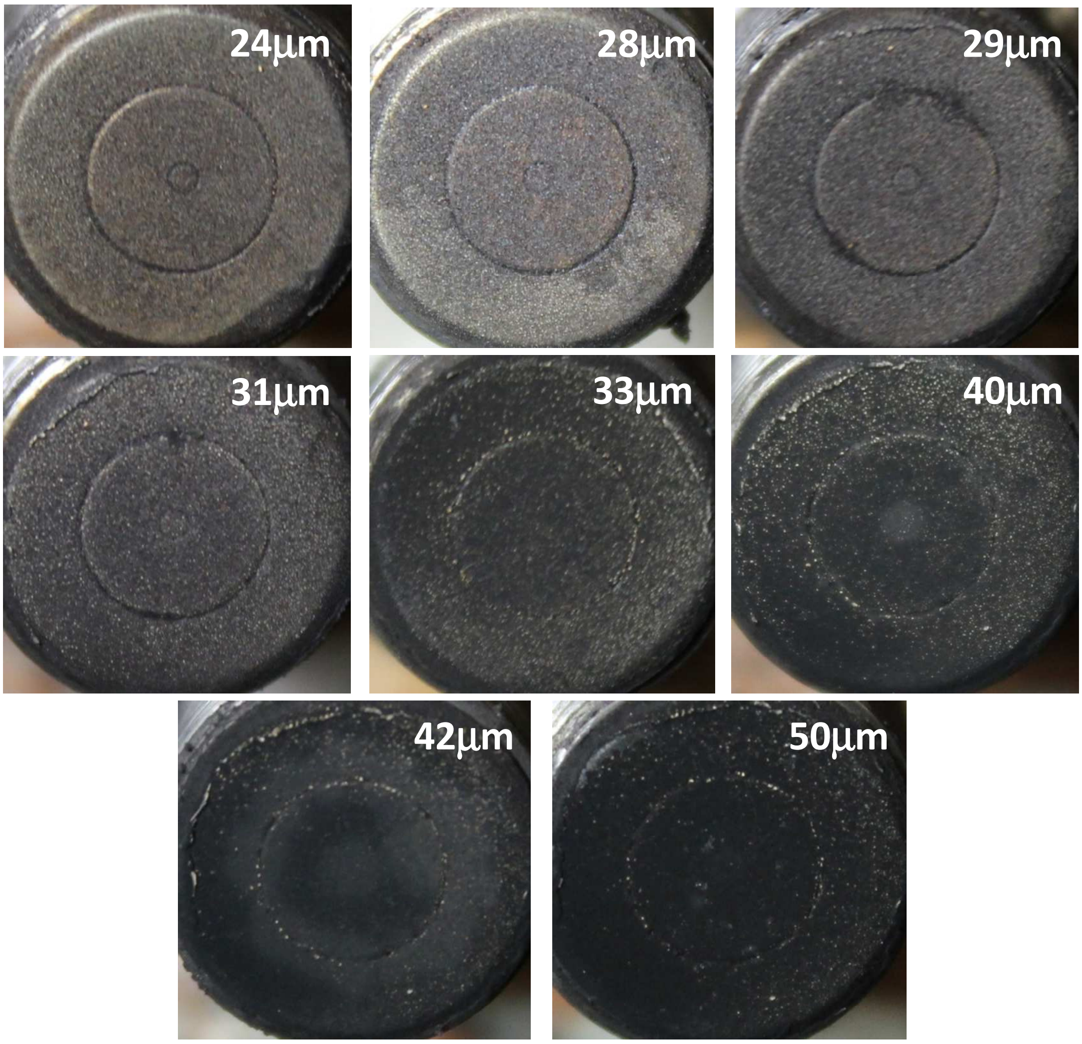

Figure 4.1 – Thickness progression on cylinder head heat flux probe #1

CCD accumulation is denoted “sparse” for thicknesses less than 30μm due to the visibility of the temperature measurement surface through the CCD layer. The temperature measurement surface is the smallest of the concentric circles shown in Figure 4.1 and Figure 4.2. In addition, for CCD thicknesses less than 30μm, the fluorescent light source used to illuminate the CCD surface for photographic purposes reflects back to the camera from the steel of the probe body and mounting sleeve. These observations are qualitative indications that line-of-sight pathways exist, which pass directly through the CCD layer for CCD thicknesses less than ~30 µm.

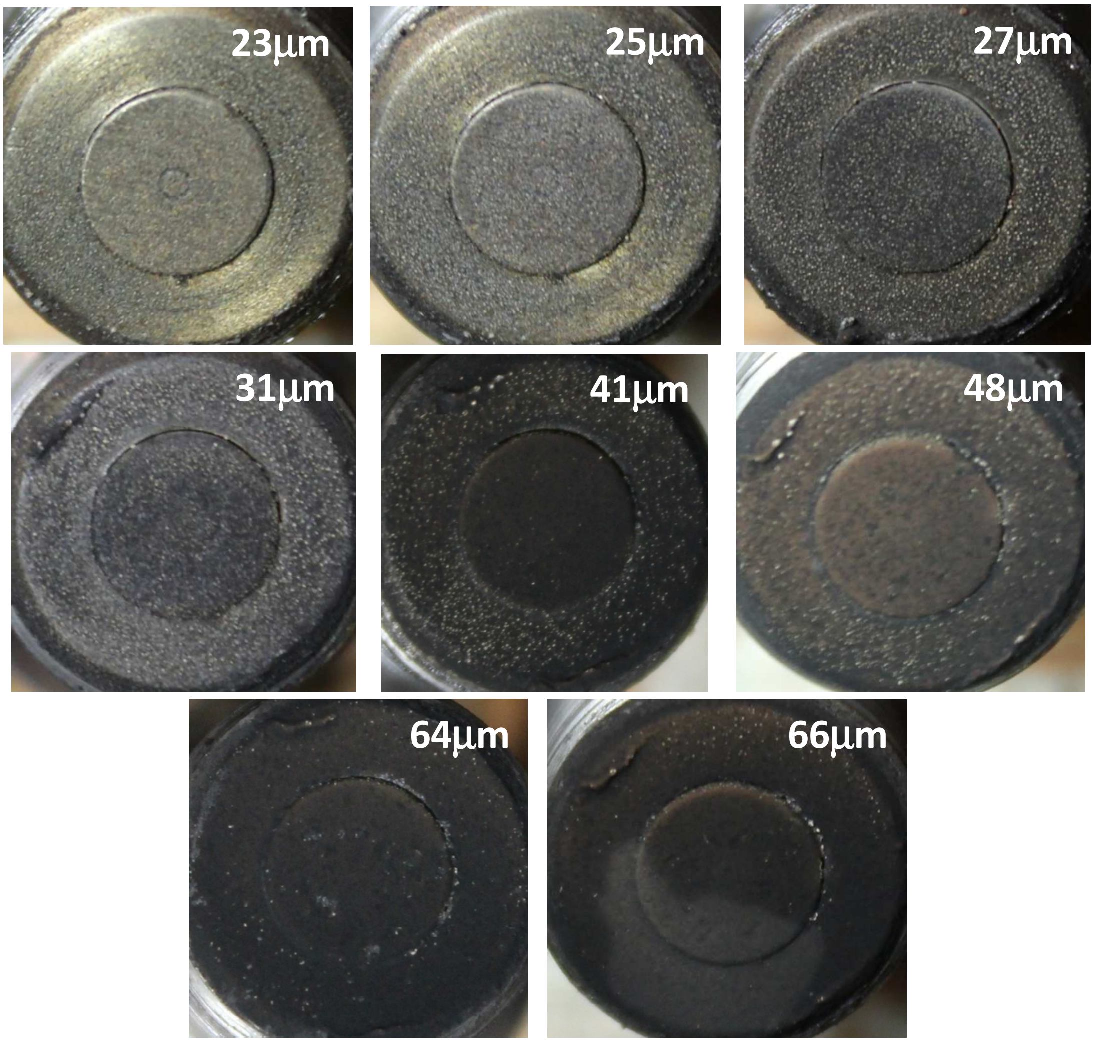

Figure 4.2 – Thickness progression on cylinder head heat flux probe #2

The temperature measurement surfaces of the cylinder head heat flux probes become completely obstructed from the camera view by between 30 and 40µm of CCD accumulation. CCD thicknesses greater than 40µm are black in color with very few yellow colored topographical features, starkly contrasting the appearance of CCD layers less than 30µm in thickness.

The gaps between CCD clumps give CCD layers of less than 30µm (“thin” CCD layers) their sparse appearance. However, the standard deviations of the CCD thickness measurements shown in Table 4.1 are insensitive to CCD thickness for the entire range of CCD thickness accumulation. This fact illustrates that the sparse nature of CCD layers less than 30µm in thickness does not impact the Fisher Dualscope measurements. If the gaps were larger than the Dualscope’s probe tip, the Dualscope would slip into these gaps during some of the multiple thickness measurements, making the standard deviation of the thickness measurements very large for the sparsely distributed CCD of less than 30µm. Instead, the Dualscope probe spans the gaps of the CCD layer during the thickness measurement process, see Figure 4.3. The physical dimensions of the Dualscope probe tip provide a maximum width for the gaps in the thin CCD layer. Accordingly, the gaps which provide a line-of-sight through the CCD layer for CCD thicknesses less than 30µm are assuredly less than 0.050” (1.27mm) in width.

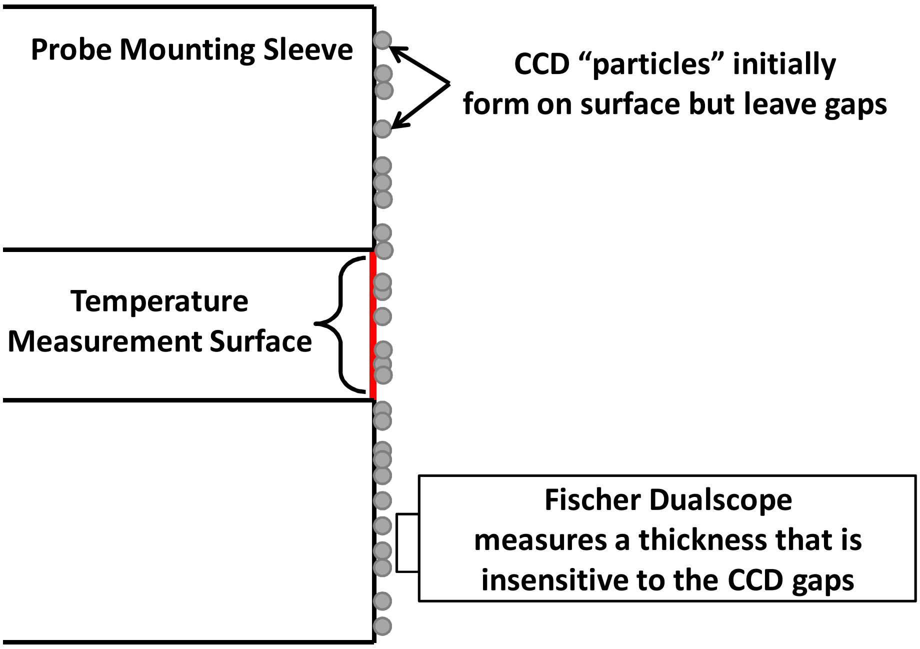

Figure 4.3 – Sectional schematic of the CCD coated cylinder head heat flux probe illustrating gaps in CCD during initial accumulation

4.2 Ex-situ and In-situ Diffusivities of Combustion Chamber Deposits

The ex-situ radiation chamber has been specifically designed to duplicate the in-situ environment in the magnitude of duration of the heat flux to which the CCD coated probes are exposed. If the in-situ impact of CCD is purely thermal, then the ex-situ and in-situ diffusivities will be the same. This section will introduce both the ex-situ and in-situ diffusivity results, both their similarities and differences.

4.2.1 Ex-situ Combustion Chamber Deposit Diffusivity

At each of the stopping points during the passive conditioning cycle, the cylinder head heat flux probes were tested in the radiation chamber to determine the ex-situ diffusivity of the CCD. Figure 4.4 shows the ex-situ diffusivity trend versus thickness on a linear scale. Each data point is an average of 2400 diffusivity values each calculated from an individual heat flux pulse. The ex-situ diffusivity data was taken in sets of 400 pulses at six different heat flux pulse durations (creating different amplitude temperature swings beneath the CCD). The vertical error bars represent the standard deviation of the 2400 individual pulses at each CCD thickness while the horizontal error bars represent a standard deviation of the twelve thickness measurements taken with the Fisher Dualscope.

Progressing toward thinner CCD from the right along the ex-situ data trend, the measured sub-CCD temperature phase lags for CCD samples quickly drop orders of magnitude from $2x10^{-3}$ seconds for 40μm CCD to $4x10^{-5}$ seconds for 28μm CCD. Temporal measurement resolution for the radiation chamber ranges from $2.1x10^{-5}$ seconds per measurement at a chopping wheel speed of 800 rpm to $1.2x10^{-5}$ seconds per measurement at 1400 rpm. Thus, for CCD samples less than 30μm, the measured phase lag of the CCD is close to the measurement resolution of the radiation chamber, creating large standard deviations in the diffusivity values.

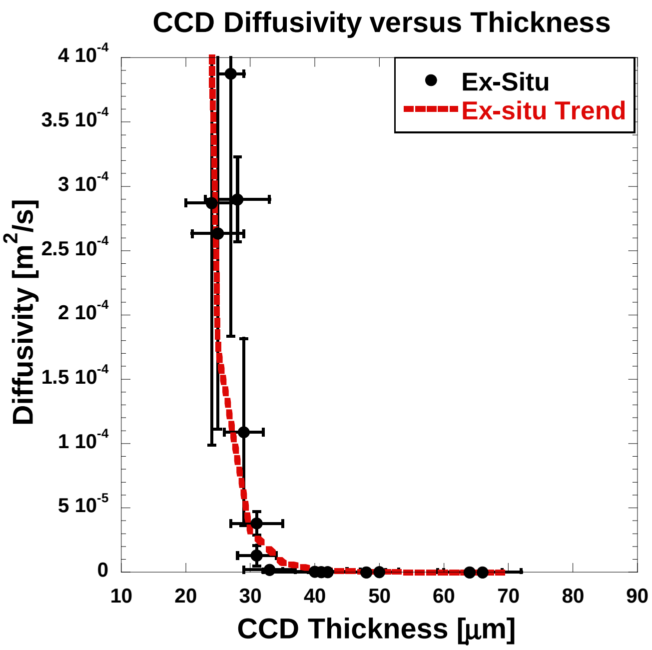

Figure 4.4 – Ex-situ CCD diffusivity values exhibiting sensitivity to CCD thicknesses less than thirty micrometers

A power law trend line has been fit through the data similar to the method utilized by Güralp [11], [13]**.** Initially, this trend appears to describe the raw data well, but when viewed on a log scale, Figure 4.5, shortcomings of this fit become obvious.

Because the ex-situ diffusivity values span nearly four orders of magnitude, the regression calculation used to determine the power fit is more sensitive to the accuracy of the higher order diffusivity values. Residual values can be large on a percentage basis for the lower order diffusivity values (at large CCD thicknesses) and still add little to the sum squared of residuals in the overall regression calculation. To avoid this quagmire, two separate fits have been employed in Figure 4.6.

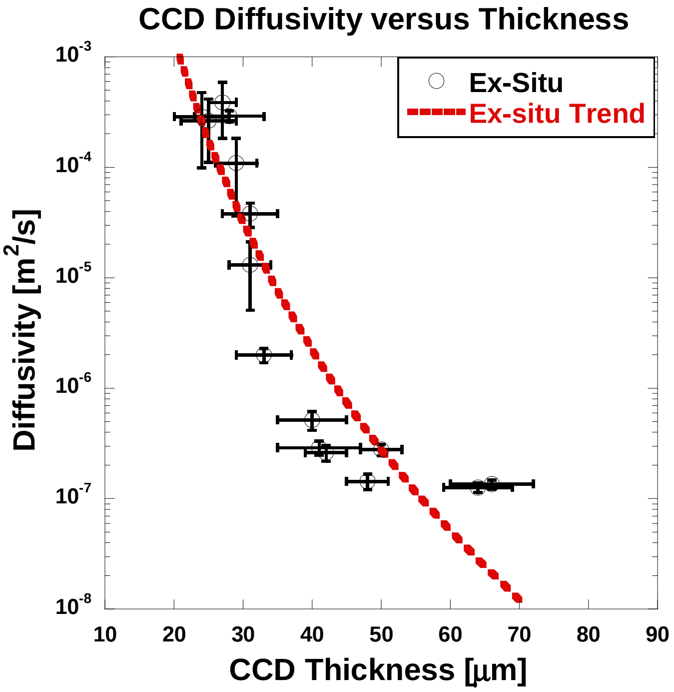

Figure 4.5 – Ex-situ CCD diffusivity plotted on a log scale to illustrate the shortcomings of a single power law fit

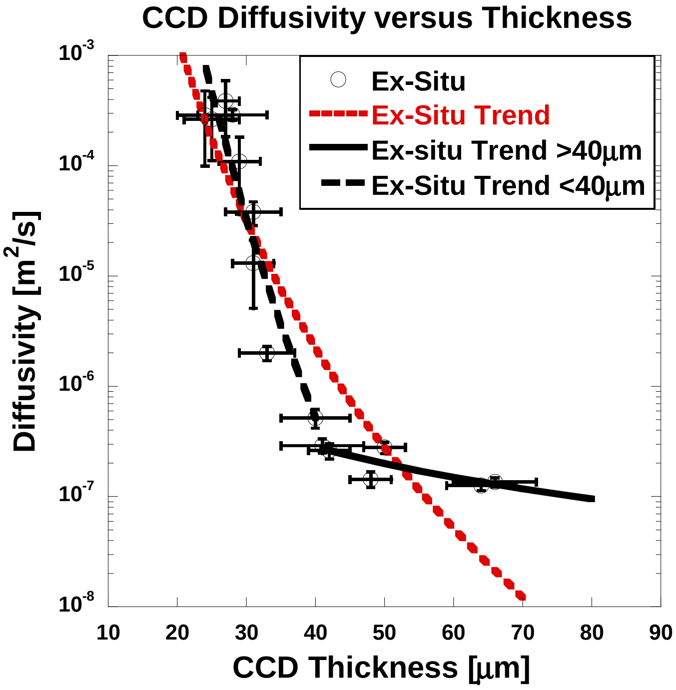

Figure 4.6 – Comparison of single and piecewise trends describing ex-situ CCD diffusivity

4.2.2 In-Situ Combustion Chamber Deposit Diffusivity

The ex-situ diffusivity values for CCD of lower thicknesses are orders of magnitude higher than those seen in-situ by previous researchers [11], [49], whose calculated diffusivities fell between 0.8 - 4.5x10^{-7} m^2/s. This investigation also measured in-situ diffusivity at each stopping point during the passive conditioning cycle. During the in-situ measurements, the engine was operated with reduced intake temperature to counteract the phasing advance caused by CCD accumulation, Figure 4.7. By removing the advance in combustion caused by CCD accumulation, it becomes a certainty that any remaining phase delay seen in the sub-CCD temperature traces is due only to the insulating effect of the CCD. This compensation technique was previously employed by [11], [13], and allows the utilization of the aforementioned diffusivity calculation methodology and calculation of in-situ CCD diffusivity via Equation 1.2.

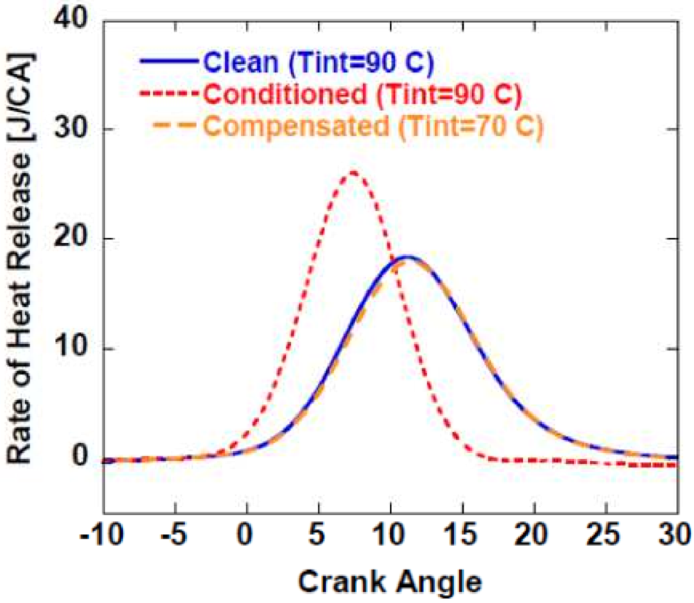

Figure 4.7 – Intake temperature compensation technique developed by Güralp et al. [13]

The in-situ trend of CCD diffusivity taken at these compensated firing points is shown in Figure 4.8. The temperature phasing delay for each probe at each CCD thickness was calculated by comparing the temperature traces recorded with a clean combustion chamber to the temperature traces recorded during intake temperature compensated operation before each stopping point. Temperature traces from two hundred consecutive engine cycles are recorded for both the clean and CCD coated cases.

While the engine combustion at each stopping point was phased to be equivalent to that of the clean chamber for the ensemble average pressure trace, the ensemble based compensation does not guarantee that the heat transfer each probe is subjected to at each individual cycle is identical for the clean and CCD coated cases. Instead of calculating diffusivities based on the phasing difference between individual clean and CCD coated temperature traces, the ensemble averages of the clean and CCD coated temperature traces are utilized. Therefore, the in-situ CCD diffusivity error bars are omitted. This technique has been previously employed by Güralp et al [13].

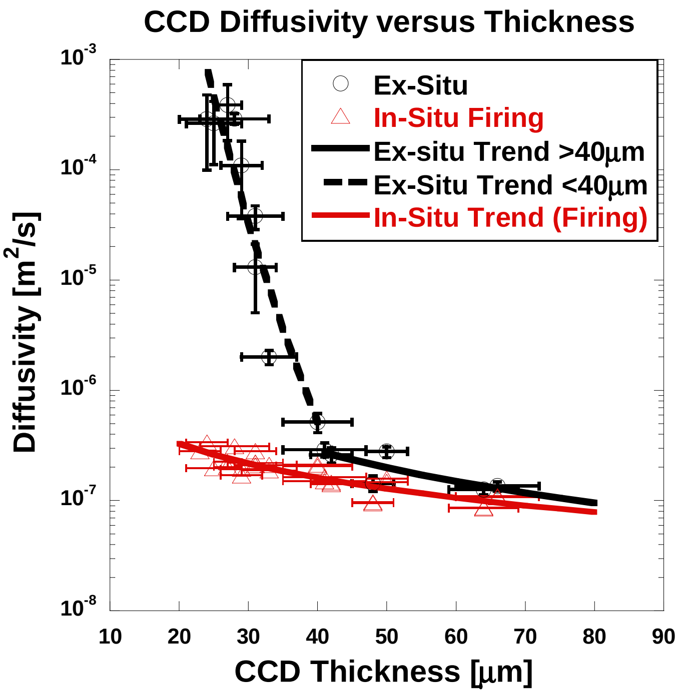

Figure 4.8 –Diffusivities calculated from ex-situ and in-situ (firing) testing

The ex-situ and in-situ firing diffusivity trends are divergent for CCD thicknesses less than 40μm. The divergence of the two data sets is not related to the assumption of the diffusivity calculation methodology because the behavior is apparent in the measured temperature and calculated heat flux traces, Figure 4.9.

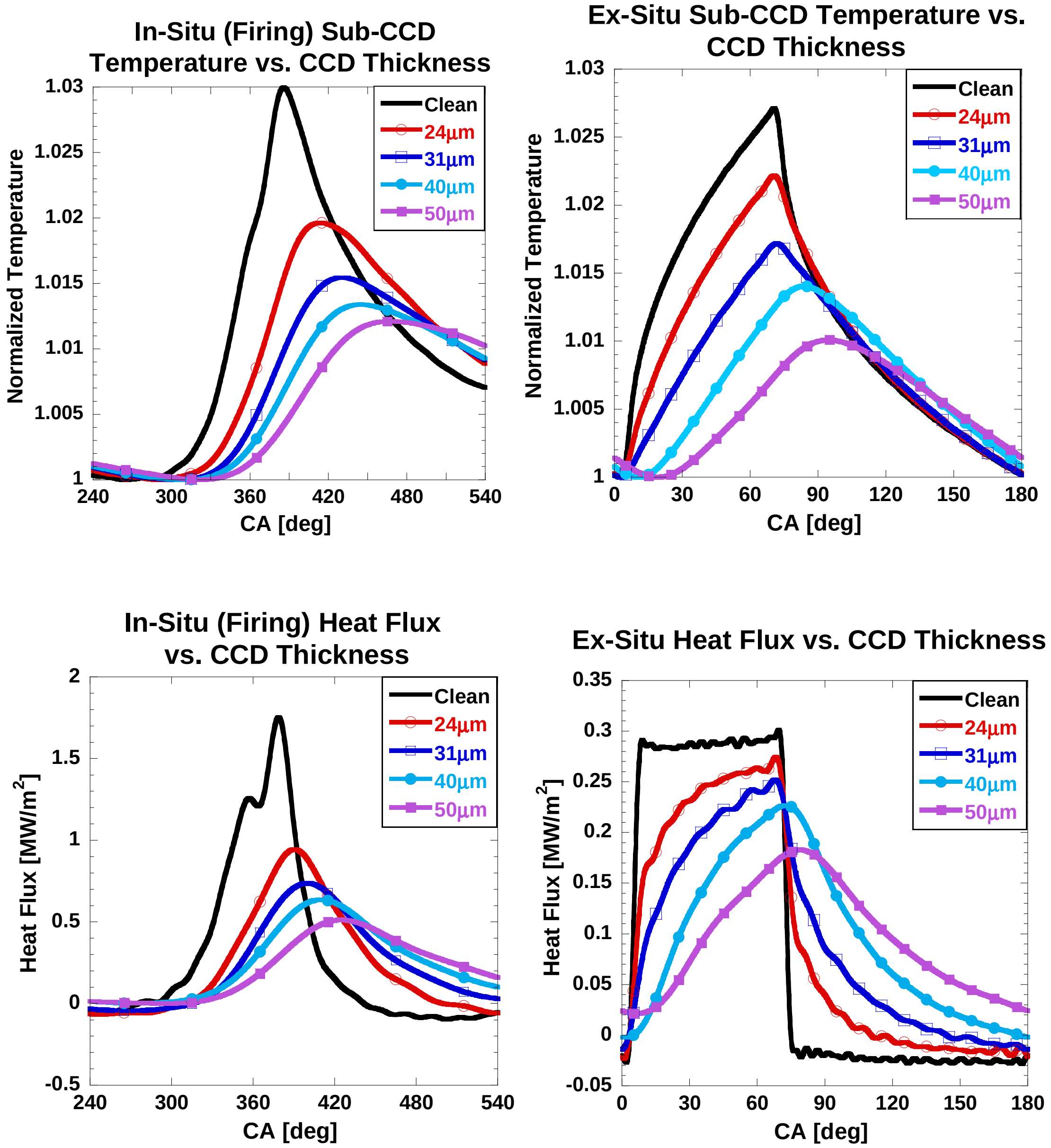

Figure 4.9 – In-situ (firing) and ex-situ temperature and heat flux traces at selected CCD thicknesses illustrating the differences in phasing behavior between ex-situ and in-situ

The ex-situ temperature and heat flux traces undergo a significant transformation in both shape and phase delay that initiates between the 31μm and 40μm cases. Ex-situ temperature traces for CCD less than 30μm qualitatively exhibit no temperature phase delay in the maximum of the temperature signal. For the thinnest case (24μm), the in-situ firing temperature trace experiences a phase delay of 2.29ms while no phase delay was measured ex-situ. The 2.29ms phase delay experienced in-situ should easily be measurable with the worst-case ex-situ temporal resolution of 21μs (corresponding to 0.1 CA resolution at a chopping wheel speed of 800 rpm).

Through analysis of the measured temperature traces, the divergence of the ex-situ and in-situ diffusivity trends has been proven to be a physical phenomenon. However, the ex-situ and in-situ measurement setups have several differences which must be investigated as possible sources of the divergent diffusivity trends. The factors to be investigated in the subsequent sections are: the interaction of compressed air with the CCD morphology, the interaction of fuel with the CCD morphology and the impact of differing heat transfer modes on CCD diffusivity.

4.3 The Effect of Compressed Air on Combustion Chamber Deposit Diffusivity

One difference between the ex-situ and in-situ experimental setups is the role of compressed air. In-situ CCD are exposed to a compressed air environment on the order of 40 bar during firing engine operation while the radiation chamber exposes the CCD to nitrogen at slightly more than atmospheric pressure. Researchers have shown the impact of material porosity on effective thermal properties due to the differences between the substrate material and the substance occupying the pores [93] - [95]. Additionally, gas is known to permeate the porosity of thermal barrier coatings [92]. Based on these precedents, the porous morphology of the CCD could contain trapped compressed air during the in-situ experiments while only containing low pressure gas during ex-situ testing, providing an opportunity for dissimilar diffusivity results.

Equation 4.1 [93] relates the effective thermal conductivity of a porous substance, k_e, with porosity fraction Φ, where k_s is the conductivity of the substrate material and k_p is the conductivity of the material filling the pores.

$$k_e = k_p^{\Phi} k_s^{(1-\Phi)} \tag{4.1}$$

Woodside's equation was used in conjunction with air properties at both 1 bar and 40 bar from the Chemical Engineer's Handbook [104] to generate trends of conductivity versus porosity fraction, Figure 4.10. The absolute substrate conductivity value for HCCI CCD is unknown and was therefore approximated from the work of Nishiwaki [48]. However, this assumed CCD conductivity value merely changes the y-intercept of the conductivity trend. Woodside's equation produces curves which are self similar in shape whose endpoints are fixed by the specified conductivities of the two constituents.

Two different CCD substrate conductivity values are utilized in Figure 4.10, 0.2 and 2.0 W/(mK). Regardless of the value utilized for CCD conductivity in the correlation, filling the CCD porosity with 40 bar compressed air rather than atmospheric air has a maximum of 2.0% impact on the effective CCD conductivity at 99% porosity. However, for more realistic porosity fractions of less than 0.50, the impact of compressed air alters CCD conductivity values less than a single percent.

At first glance, this result may appear contradictory to the work of Rätzer-Scheibe and Schulz who noted as much as a 10% change in the conductivity of yttria stabilized zirconium coatings at different pressures [103]. However, their experiments tested ceramic samples at a much higher temperature, 1100ºC, and altered the pressure from a vacuum to 1bar of argon gas. Thus, their results reflect a change from evacuated pores to pores filled with argon at high temperature rather than two positive pressures with the same substance at a relatively low temperature.

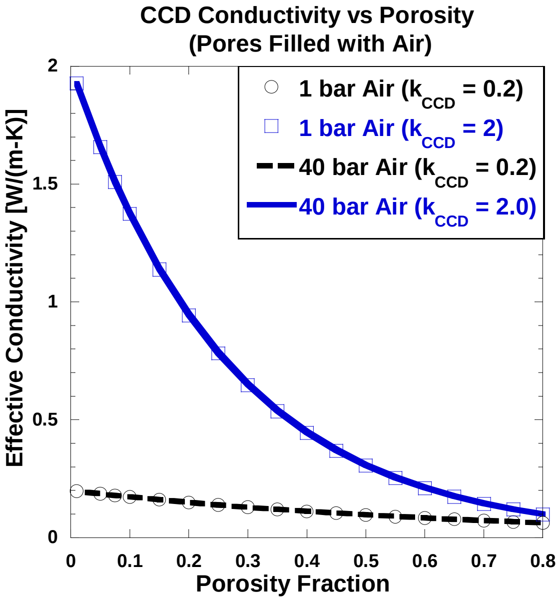

Figure 4.10 – The influence of air filled CCD porosity on effective CCD conductivity

The effective conductivities from Figure 4.10 were used in conjunction with Equation 4.2 to generate trends of effective CCD diffusivity, α_e, versus porosity fraction, Φ, where ρ_p and C_p are the density and heat capacitance of the air filling the pores and ρ_s and C_s are the density and heat capacitance of the CCD substrate, Figure 4.11. The heat capacitance and density for atmospheric and 40 bar air were taken from [104] while the value for $\rho_s C_s$ was calculated from a CCD diffusivity value of 2.0x10^{-7} m^2/s (a value which is within the diffusivity ranges of [11], [48] and [49] as well as the ex-situ results) and the assumed values of k_{CCD} mentioned above.

$$\alpha_e = \frac{k_e}{\left(\Phi\rho_p C_p + (1-\Phi)\rho_s C_s\right)} \qquad (4.2)$$

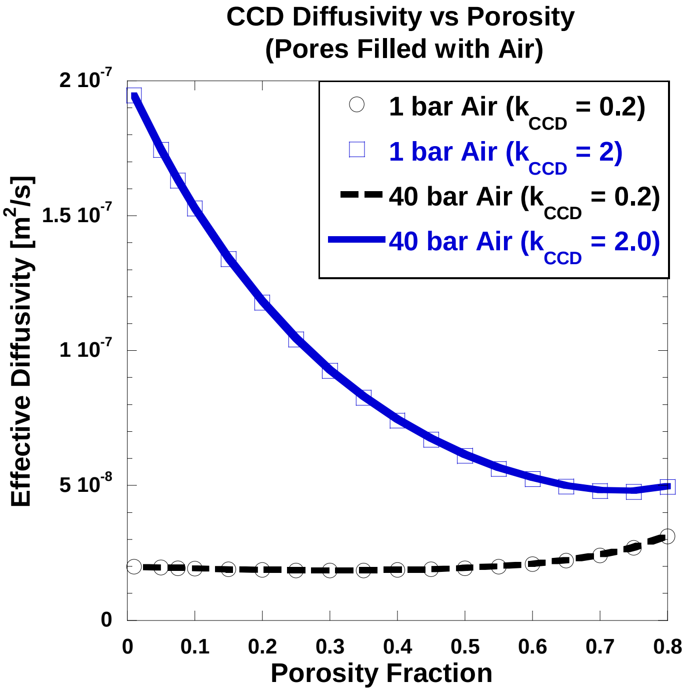

Figure 4.11 – The influence of CCD porosity on effective CCD diffusivity

As with effective conductivity, the effective CCD diffusivity is virtually unaltered by the use of compressed air rather than atmospheric air within the pores. The diffusivity was altered by a maximum of 0.7% across the entire range of porosity fraction. Thus, the pressure differences between the in-situ and ex-situ measurement environments did not create the significant differences between the measured in-situ and ex-situ diffusivity values.

4.4 The Impact of Fuel on Combustion Chamber Deposit Diffusivity

A second point of difference between the in-situ and ex-situ measurement environments is the presence of fuel in-situ. In-situ motoring operation is devoid of fuel, which allows comparisons between in-situ firing and in-situ motoring to indicate the impact of fuel interaction with the CCD morphology on diffusivities calculated in-situ. The impact of fuel can be successfully isolated by this comparison because differences in compression between the motoring and firing in-situ operation fall within the range of pressures examined in the preceding section, and therefore will wield no influence on the comparison of motoring and firing in-situ diffusivities.

Figure 4.12 displays the sub-CCD temperature and heat flux profiles for select thicknesses from the in-situ motoring and in-situ firing data sets. Both in-situ data sets experience trend-wise similarity in the sub-CCD temperature and heat flux response across the entire CCD thickness spectrum.

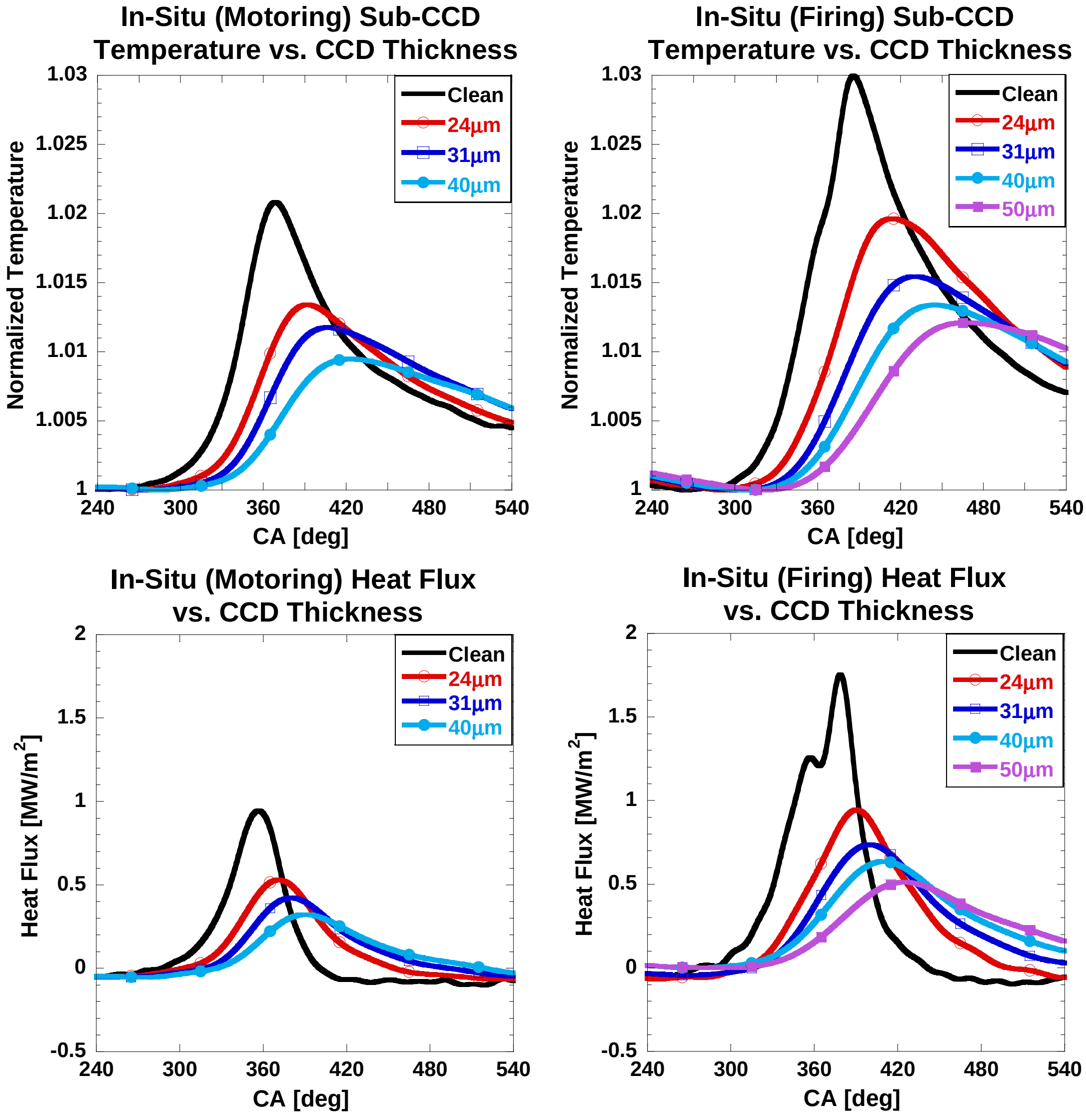

Figure 4.12 – In-situ motoring and in-situ firing temperature and heat flux traces for select CCD thicknesses

As with the in-situ firing operation, the in-situ motoring diffusivities were calculated from ensemble average temperature traces taken during clean operation and subsequent CCD coated operation. The ensemble averages were calculated from 200 individual temperature traces measured during consecutive cycles. Figure 4.13 and Figure 4.14 show the diffusivities calculated during in-situ motoring operation relative to the ex-situ and in-situ firing diffusivity values on logarithmic and linear scales, respectively. The motoring and firing in-situ data sets are overlapping and have power function fits which converge for CCD thicknesses greater than ~45μm. Quantitatively, the difference between the in-situ firing and motoring data averages 7.7%. The maximum difference between the data sets occurs for the thinnest CCD tested and has a magnitude of 20%. The in-situ data, with motoring and firing points combined into one data set, produces a trend which splits the difference between the motoring and firing trends, and is shown in Figure 4.15. The error bars have been removed from Figure 4.15 for visual clarity.

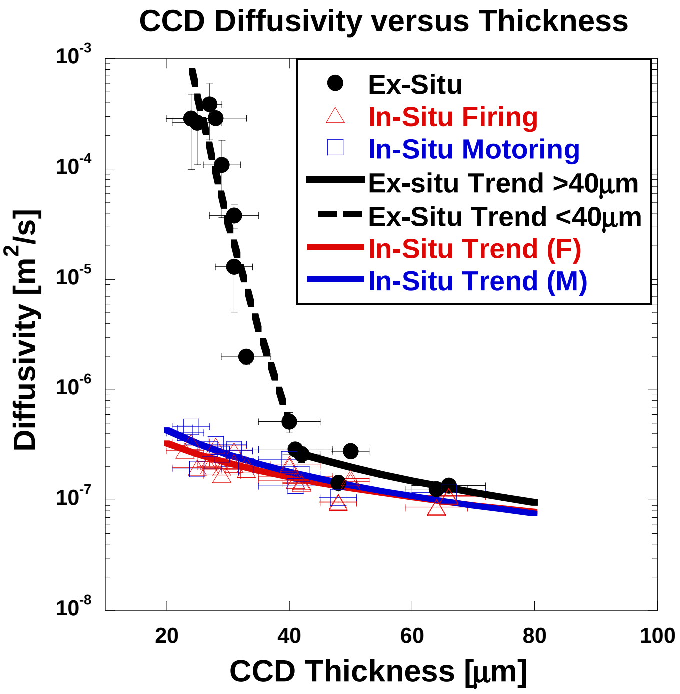

Figure 4.13 – In-situ motoring, in-situ firing and ex-situ diffusivities plotted on a log scale and illustrating the similarity of in-situ motoring and firing data

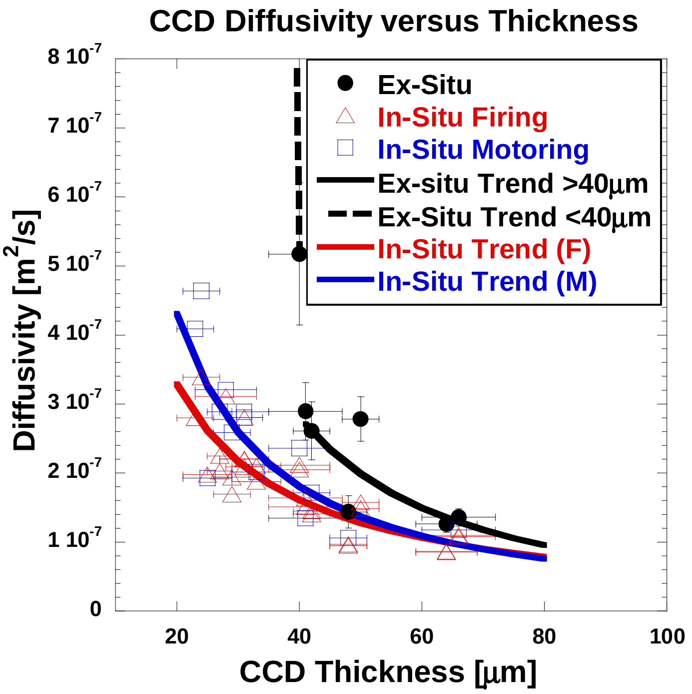

Figure 4.14 – In-situ motoring, in-situ firing and ex-situ diffusivities plotted on a linear scale and zoomed to highlight the similarity of in-situ motoring and firing data

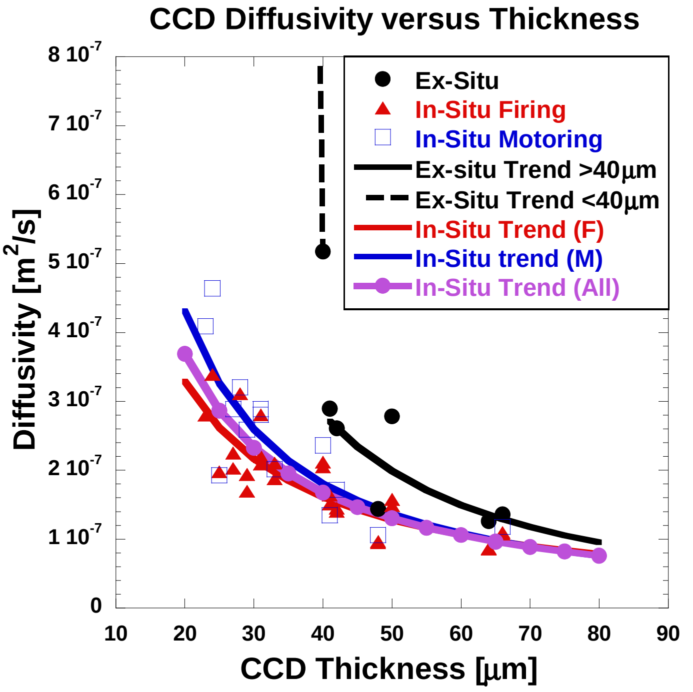

Figure 4.15 – In-situ (all) trend produced through combining both in-situ data sets together produces plotted with the individual data sets

With less than an eight percent difference between the motoring and firing in-situ data, it can be safely stated that the fuel interaction with CCD morphology does not wield a significant impact on CCD diffusivity on the cylinder head probes. Therefore, the difference between diffusivities determined ex-situ and in-situ cannot be attributed to the presence of fuel in-situ.

4.5 The Impact of Heat Transfer Mode on Combustion Chamber Deposit Thermal Diffusivity

The last significant disparity between the in-situ and ex-situ environments is the heat transfer mode used to deliver the heat flux pulse to the cylinder head probes. The ex-situ environment utilizes radiation to deliver the heat flux while in-situ relies on convection and conduction. Differences between in-situ firing and motoring heat transfer modes are assumed to be of little consequence to CCD diffusivity on the cylinder head probes due to the aforementioned similarity of their calculated diffusivities.

4.5.1 Peak Temperature Phase Delay Analysis

In order to facilitate a more productive discussion regarding the impact of heat transfer mode on CCD diffusivity it becomes useful to take a step backward in processing from the diffusivity values. Figure 4.16 shows the measured peak temperature phase delays used to calculate the previously shown ex-situ and in-situ diffusivities. In the time domain, the temperature phase delay has a strong linear correlation to CCD thickness. As with the diffusivities calculated from these phase delays, the firing and motoring in-situ data have linear which overlap. As discussed in the previous section, the two in-situ data sets are taken together and fit with a single trend as shown in Figure 4.17.

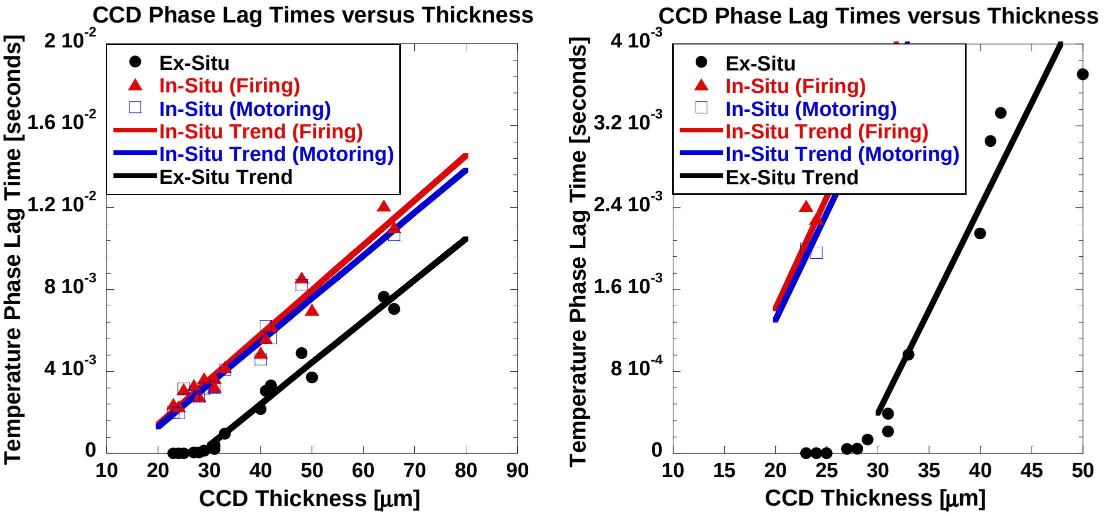

Figure 4.16 – In-situ firing, in-situ motoring and ex-situ peak temperature phase lag times shown at full scale and zoomed for clarity

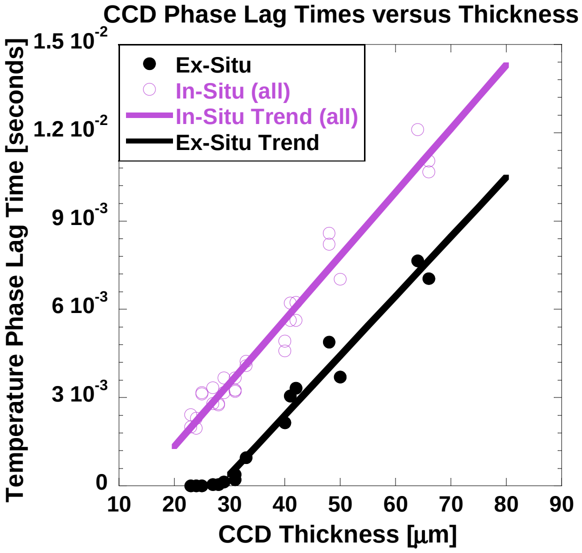

Figure 4.17 – In-situ and ex-situ peak temperature phase lag times with the in-situ motoring and firing data taken together as a single data set

A portion of the ex-situ phase lag data has a linear trend with CCD thickness. This linear portion of the data begins between 30-40µm, which is the same region of CCD thickness where the ex-situ diffusivity trend was noted to have changed significantly. The linear portion of the ex-situ data is very similar in slope but shifted from to the two in-situ trends. The in-situ trend is y=2.16E-4(x)-2.99E-3 and ex-situ linear trend is y=2.02E-4(x)-5.67E-3, where y is sub-CCD phase delay in seconds and x is CCD thickness in micrometers. However, the ex-situ data is non-linear at CCD thicknesses less than 30μm. While the analysis of CCD peak temperature phase delay is similar to that of the CCD diffusivities, the linear nature of the phasing trends better facilitates comparisons in heat flux mode response of the CCD.

4.5.2 Partial Transparency of Combustion Chamber Deposits to Radiation Heat Flux

Semi-transparent response of other substances to the ex-situ radiation pulse has been addressed by this work in earlier chapters. During calibration testing, the impact of transparency was mitigated through the application of a graphite aerosol spray to the surface of the calibration wafers. The aerosol spray is initially wet when applied and quickly dries. Due to concerns that this wet-when-applied aerosol spray could wick into any interconnected porosity network within the CCD and alter diffusivity values measured later during the accumulation process, no graphite was applied to the CCD during the passive conditioning. However, due to the significant difference between ex-situ and in-situ measurements at low CCD thicknesses, additional HCCI operation was conducted to accumulate a CCD layer within the sub 30μm thickness range which exhibited the nonlinear peak temperature phase delay. This additional round of CCD accumulation provided ex-situ measurement points for which the ex-situ CCD diffusivity could be determined first without, and then subsequently with, graphite applied to the surface.

Figure 4.18 shows a comparison of ex-situ temperature and heat flux traces with and without graphite applied to the CCD surface. The applied graphite induces an increase in sub-CCD temperature phase delay indicating a partial transparency of the CCD to the ex-situ radiation pulse. A corresponding phase shift is also apparent in the rise and fall of the heat flux trace. The cumulative heat fluxes for these two cases are within 2.5%, indicating that any change in absorption experienced by the CCD due to the application of graphite is minimal.

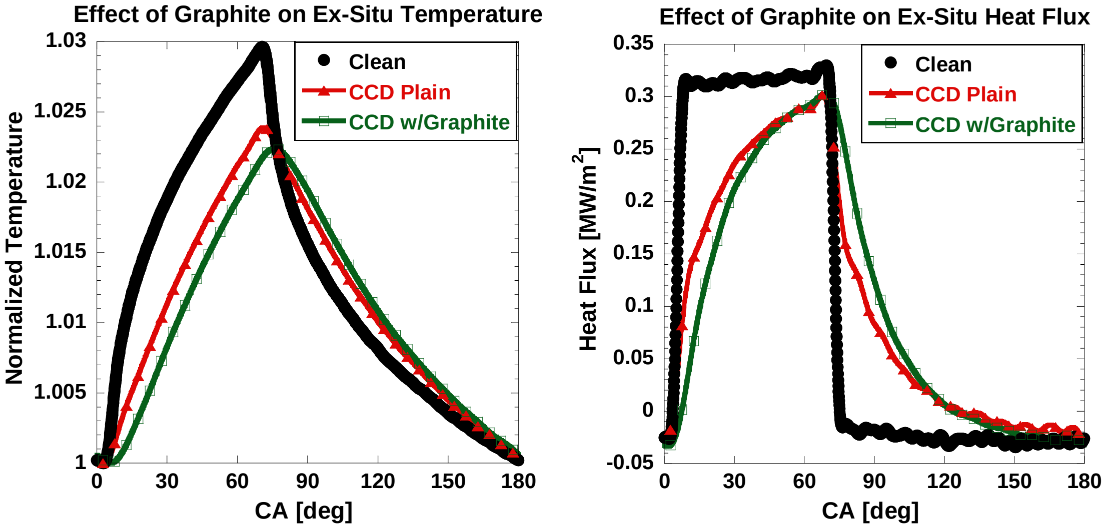

Figure 4.18 – Impact of graphite applied to CCD surface on sub-CCD temperature and heat flux

The magnitude of the phase delay increase is readily apparent when the open and closed diamonds of Figure 4.19 are compared. Minimizing the transparency of CCD to the ex-situ radiation source by applying graphite to the surface has provided a shift towards the in-situ phase delay trend. The application of graphite increased the phase delay of the 24μm CCD sample by 38μs, an increase of 81%, while the 26μm CCD sample saw its phase delay increase by 71μs, an increase of 90%. Thus, the shift in phasing created by minimizing CCD transparency is not constant in magnitude or percentage for this limited sample.

The shift in temperature phasing created via graphite application reduced the diffusivities of the 24μm and 26μm CCD samples by nearly two orders of magnitude (factors of 82 and 87, respectively), but still does not provide the full shift necessary to match these ex-situ points to the in-situ results. The diffusivity reductions can be seen in Figure 4.20.

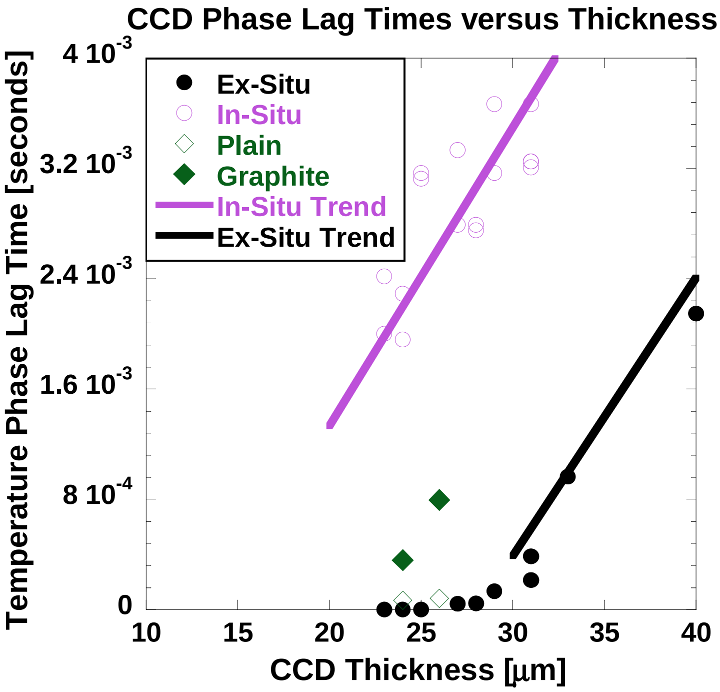

Figure 4.19 – The increase in sub-CCD temperature phase delay caused by minimizing CCD radiation transparency with graphite

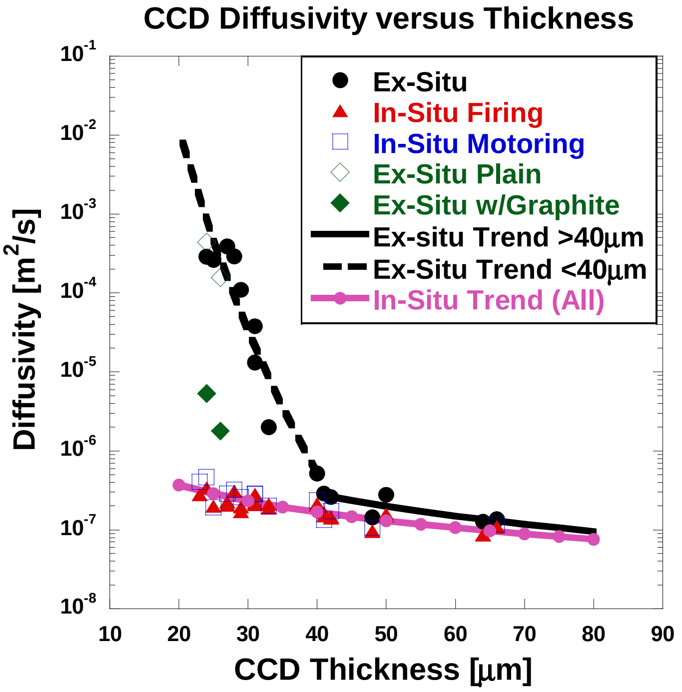

Figure 4.20 – The shift in ex-situ diffusivity caused by minimizing radiation transparency through the application of graphite to the CCD surface

The impact of transparency on sub-CCD temperature phase delay and CCD diffusivity was not constant for the two points tested and may be a function of CCD thickness. However, with the limited graphite coated data, it is difficult to fully quantify the impact of partial radiation transparency on the ex-situ results. In the absence of more results, the impact of transparency was assumed to be a time constant whose magnitude was set to the average of the two points tested, 50μs. This time constant was added to the ex-situ CCD temperature phase lag across the entire CCD thickness spectrum, producing a shift in the sub-CCD temperature phase and CCD diffusivity trends which are shown in Figure 4.21 and Figure 4.22, respectively. While the application of graphite provides additional temperature phase delay indicating that transparency plays a role in the difference between ex-situ and in-situ results it is clear that other factors are still influencing the ex-situ results.

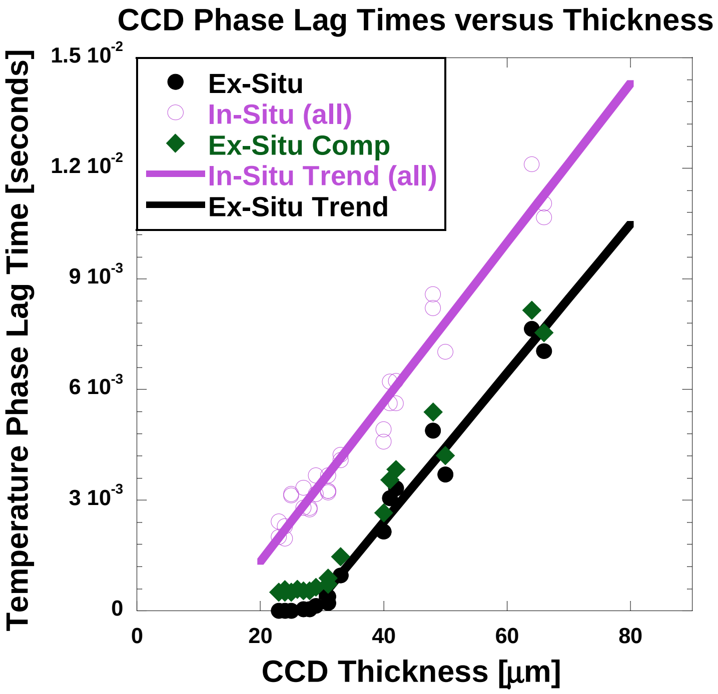

Figure 4.21 – Temperature phase lag with constant impact of transparency applied to ex-situ results

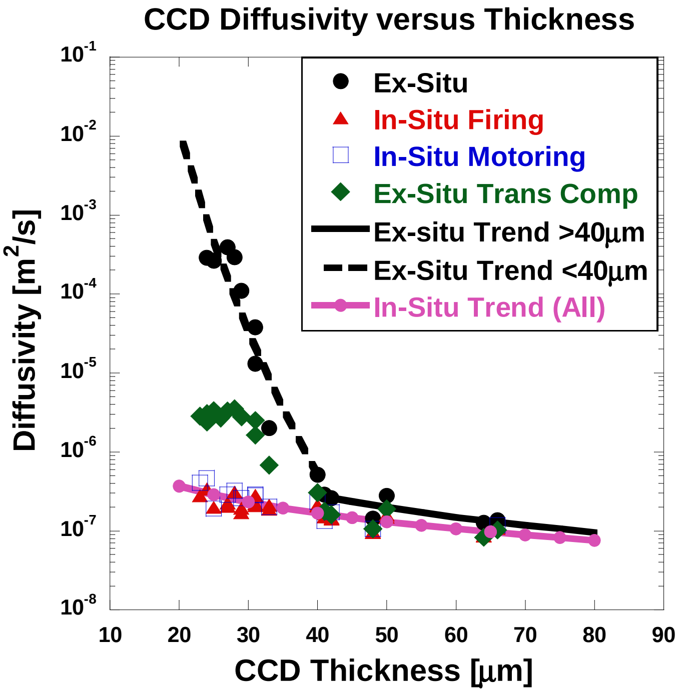

Figure 4.22 – CCD diffusivities illustrating the impact of the transparency compensating temperature phasing shift on the ex-situ results

4.5.3 Penetration of Radiation into the Morphology of Combustion Chamber Deposits

The discussion presented earlier in this chapter utilized Figure 4.3 and surmised that gaps between the initial clumps of CCD were small enough to not influence the measured CCD thickness. However, these gaps provided a line of sight directly through the CCD to the temperature measurement surface of the heat flux probes as shown in Figure 4.23.

The insensitivity of sub-CCD temperature phase delay to CCD thickness for CCD less than 30µm indicates that a portion of the radiation pulse penetrates through the porosity network in a line-of-sight fashion directly to the temperature measurement surface. Contrarily, the in-situ results report a phase delay for these same CCD layers. This confirms that the length scale of the convection currents within the chamber is larger than the maximum gap width of 1.27mm as previously determined from the physical dimensions of the Fischer Dualscope. Thus, because the in-situ convection cannot penetrate into the gaps, the CCD appear as a solid wall.

Convection is driven by flow and temperature gradients which have both been shown to have length scales large enough to prohibit penetration into the CCD gaps through the experimental findings of other researchers [105], [106]. The investigation of Dronniou and Dec focused on HCCI thermal stratification and revealed cold pockets within the combustion chamber near TDC on the millimeter scale [105]. Funk et al. determined that mixing lengths within a combustion chamber were greater than 4.0mm although they suggested that mixing could occur down to the scale of ~1.0mm [106].

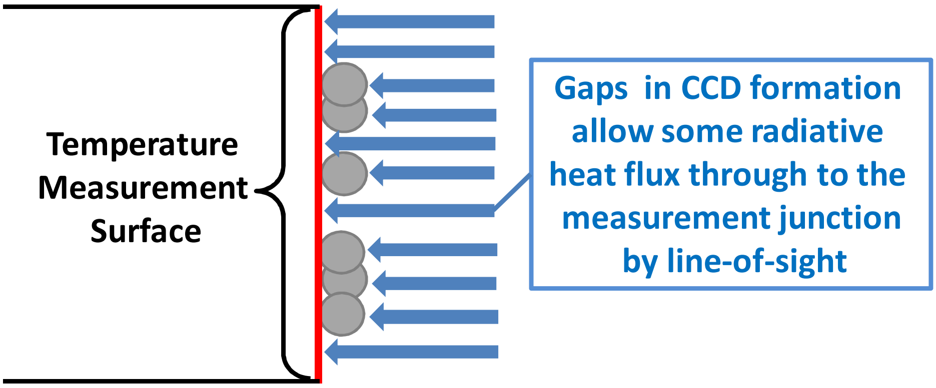

Figure 4.23 – Influence of initial CCD gaps on radiation pulse

As CCD continue to accumulate, some of the line-of-sight pathways, which previously extended straight to the temperature measurement surface, have now been blocked, Figure 4.24. The measured ex-situ sub-CCD temperature traces and their corresponding sub-CCD temperature phasing remain insensitive to the increased CCD accumulation through thicknesses of ~30µm, indicating that some gaps in CCD formation continue to provide direct pathways for radiation to reach the temperature measurement surface. Although some of the line-of-sight pathways no longer extend directly through the CCD to the temperature measurement surface, they still provide avenues which allow some of the ex-situ radiation to penetrate part of the way through the CCD thickness.

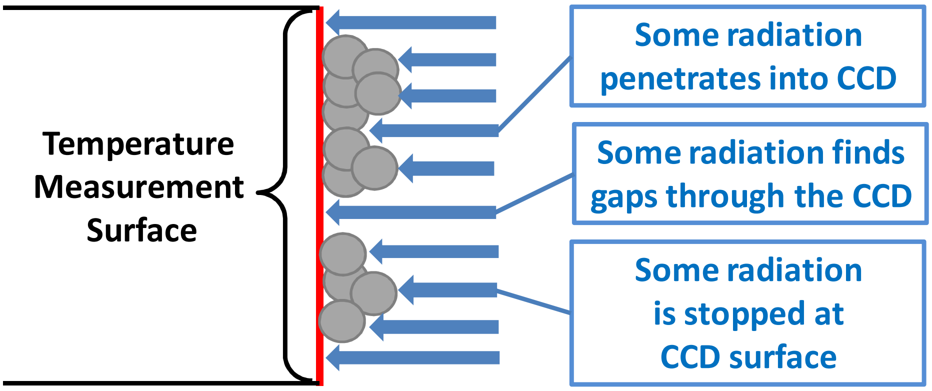

Figure 4.24 – CCD accumulation schematic for thicknesses less than ~30µm illustrating the continued impact of the sparse CCD distribution

The change in ex-situ sub-CCD temperature phase delay behavior that occurs at CCD thicknesses between 30 and 40µm in Figure 4.16 can be attributed to the elimination of all gaps which provide a direct path through the entire thickness of the CCD. Qualitative examination of Figure 4.1 and Figure 4.2 reinforce this conclusion as the circular outline of the temperature measurement surface is no longer visible in this range. Additionally, the ex-situ sub-CCD temperature phase delay becomes sensitive to CCD accumulation in this thickness range and begins its linear relationship with CCD thickness. With the elimination of these line-of-sight pathways directly to the measurement surface, all of the ex-situ radiation pulse now passes through some thickness of CCD before reaching the measurement surface, Figure 4.25.

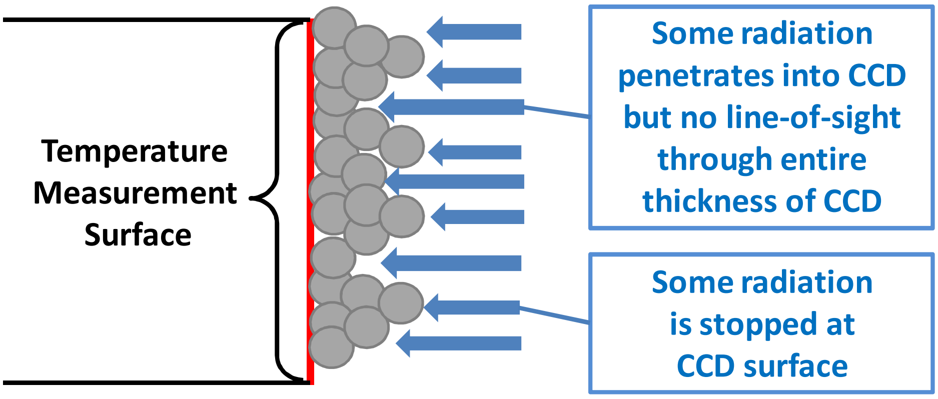

Figure 4.25 – CCD accumulation schematic for thicknesses from 30-40µm where the entire temperature measurement surface is now coated with CCD

As CCD accumulate to thicknesses greater than 40µm, some ex-situ radiation finds the gaps in the surface of the CCD layer and penetrates partially through the thickness, Figure 4.26. Due to the linear nature of the ex-situ temperature phase delay in this CCD thickness range, shown in Figure 4.16, the effect of radiation penetration is assumed to be constant versus thicknesses.

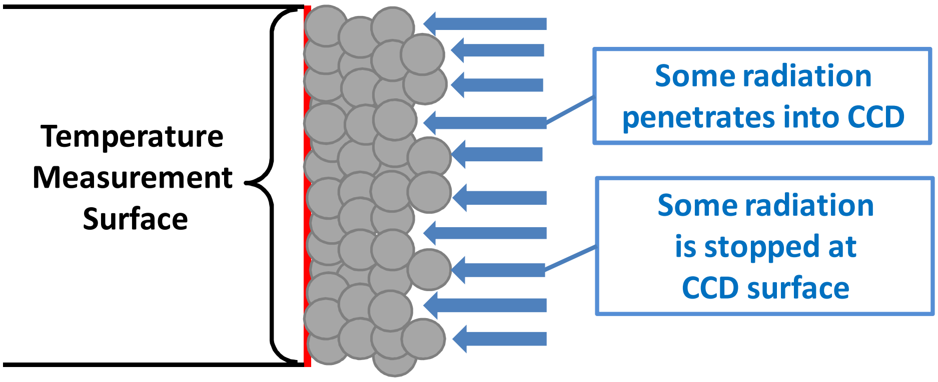

Figure 4.26 – CCD accumulation schematic for thicknesses >40µm exhibiting the penetration of radiation into the porosity of the CCD

To quantify the penetration of the ex-situ heat flux pulse into the porosity network of CCD, the linear portion (>30µm) of the transparency compensated ex-situ phase delay data is shifted to match the in-situ phase delay trend. The average thickness separating the ex-situ data from the in-situ trend was found to be 13µm. The shifted ex-situ phase delay curve is shown in Figure 4.27 and the impact of shifting the curve on the ex-situ diffusivity trend in shown in Figure 4.28. This shift establishes the penetration of the radiation pulse into a relatively thick, full coverage CCD layer at 13µm.

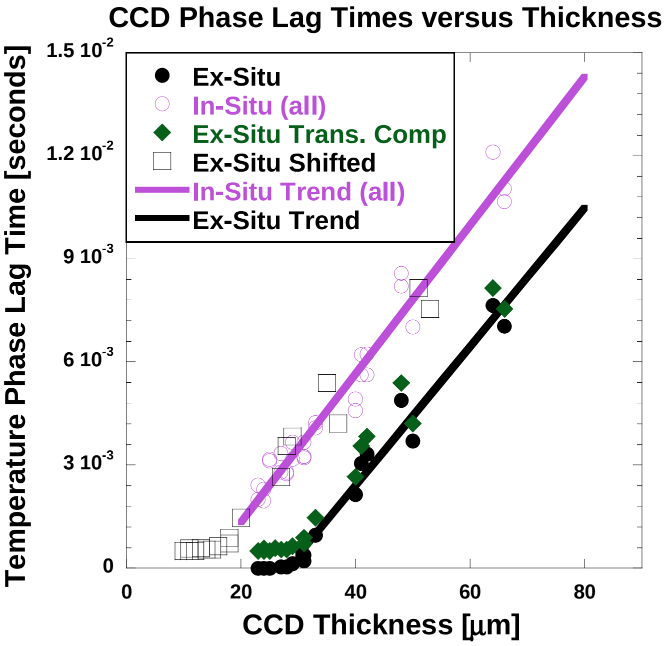

Figure 4.27 – Shifting the ex-situ phase delay curve to quantify the penetration of radiation into the CCD

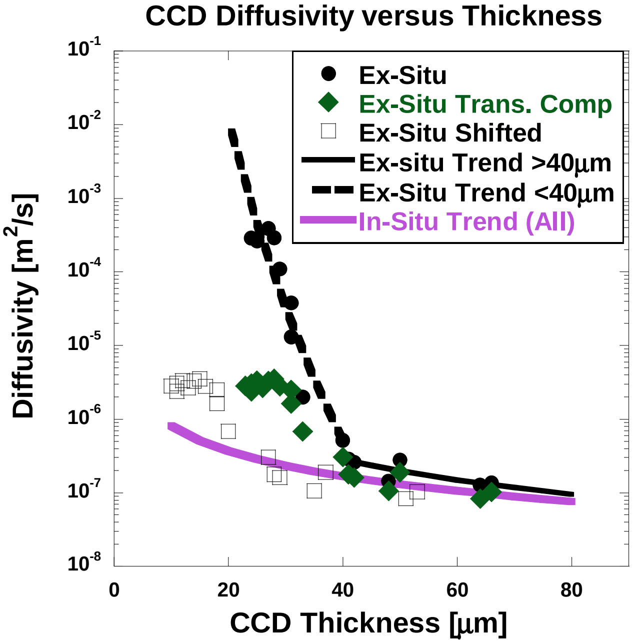

Figure 4.28 – Effect of Shifting the Ex-Situ Phase Delay on the Ex-Situ Diffusivity Data

The length units accompanying this radiation penetration shift can be misleading. The 13µm shift of the ex-situ phase delay data encompasses the impact of both the number of pores present on the surface of the CCD and the depth of those pores, which, taken together, represent the effective porosity of the CCD layer. The radiation penetration shift signifies the thickness of CCD whose phase lag has been negated by the penetration of radiation into the effective porosity of the CCD during ex-situ testing. Deeming this shift a “radiation penetration factor” and tracking it for both CCD and thermal barrier coatings gives an indication of the effective porosity of each substance as seen by the combustion chamber gases. In addition, since the radiation penetration factor was determined by comparing the CCD response to radiation relative to convection, it lends itself toward application in the diesel combustion industry both as an indicator of CCD porosity and in quantifying the amount of radiation heat transfer present in-situ.

The shape of the ex-situ sub-CCD temperature phasing trend was unaltered by the application of the constant radiation penetration factor. The radiation penetration factor only compensates the ex-situ data for the penetration of radiation into a CCD layer having no line-of-sight pathways directly to the temperature measurement surface. It is the sparse nature of the CCD accumulation that provides these line-of-sight pathways and creates the nonlinear shape in the ex-situ sub-CCD phase delay trend for CCD less than 30μm. Compensating for the varying temperature measurement surface area exposed directly to the ex-situ radiation pulse during the initial stages of CCD accumulation (<30μm) has the potential to linearize this portion of the ex-situ trend, but is beyond the scope of this work.

4.6 CCD Diffusivity Conclusions and Contributions

The ex-situ diffusivity data was shown to shift trends in the CCD thickness range of 30-40 micrometers. The ex-situ and in-situ CCD peak temperature phase delay and diffusivity data sets were found to differ significantly for CCD thinner than 30μm.

Analytical investigation showed that CCD diffusivity was not influenced by the pressure differences between the in-situ and ex-situ environments. Because compressed air was proven a non-factor in the determination of CCD diffusivity, in-situ firing and in-situ motoring operation differ only by the presence of fuel.

In-situ firing and motoring results differed by an average of 7%, proving that there was virtually no impact of fuel on CCD diffusivity for the cylinder head probe samples tested. However, it is important to note that these two probe locations are not significantly wetted by the fuel spray. CCD in the bowl, which are exposed directly to the fuel spray and subsequent fuel wetting/pooling, may exhibit different characteristics. Furthermore, the similarity of the in-situ firing and motoring diffusivities provides evidence that radiation is not a significant source of heat transfer during HCCI combustion.

CCD exhibited a partial transparency to the ex-situ radiation pulse, but minimization of this effect through the application of a graphite opacity layer did not fully eliminate the differences between ex-situ and in-situ diffusivity values. The impact of transparency was assumed constant for this work. The transparency impact could not be conclusively proven constant due to the small sample size and limited CCD thickness range of those samples.

The CCD allow penetration of the ex-situ radiation pulse due line-of-sight pathways in their accumulated structure. These pathways were provided by both the porosity of the CCD layer and gaps in the sparse distribution of CCD during accumulation.

During initial CCD accumulation, the pathways and gaps can extend straight to the temperature measurement junction of the heat flux probe, reducing ex-situ phase delays and creating high ex-situ diffusivities for CCD less than 30 micrometers. The convection heat transfer which dominates motoring conditions and HCCI firing operation cannot penetrate into these pathways and simply impinges on the CCD surface. Thus, the in-situ heat flux must traverse the entire thickness of the CCD layer while the ex-situ radiation heat flux experiences the resistance of either a reduced thickness of CCD or no

CCD depending on the area coverage of CCD on the temperature measurement surface. This results in longer sub-CCD phase delays in-situ than ex-situ and the accompanying disparity in diffusivity results. Determining the spatial coverage of the CCD on the temperature measurement surface during the initial stages of CCD accumulation could be used to eliminate the difference between ex-situ and in-situ results for this range of CCD thickness, but is beyond the scope of this study.

As CCD accumulation continues past 40μm, the temperature measurement surface becomes completely covered with CCD. In this thickness regime, the line-of-sight pathways penetrate only part way into the CCD thickness. This again allows some of the radiation pulse to experience the thermal resistance of only a portion of the CCD thickness, but now all of the radiation pulse experiences at least some resistance due to the CCD.

The radiation penetration factor was developed to quantify the impact radiation penetration into a CCD layer with full spatial coverage of the temperature measurement surface. The factor is calculated by shifting the ex-situ sub-CCD phase delay trend to match the in-situ trend. The CCD formed during this study had a radiation penetration factor of 13 micrometers.

The radiation penetration factor encompasses the number of exposed pores and the depth of those pores and can be viewed as an effective porosity measurement. Because the radiation penetration factor is generated by comparing the CCD response to radiation versus convection, it becomes a useful tool to quantify the relative amounts of each heat transfer mode in combustion concepts like diesel which experience significant radiation heat transfer [16]. Additionally, comparing radiation penetration factors between CCD formed under different operating conditions or with different fuels can provide substantial insight into the formation behavior and morphology of the CCD layers. The factor can also be used as a basis for comparing the porosity of CCD to that of different thermal barrier coatings.

CHAPTER 5

DIFFUSIVITY OF THE MAGNESIUM ZIRCONATE THERMAL BARRIER COATING

The thermal properties of flame sprayed ceramics are difficult to quantify. Vendors release a wealth of information about the substrate material and little of the final construct. The final properties of the coating are dependent upon several application variables (amount of coating applied per spray pass, angle of the spray gun to the object, translational speed of each pass, etc). This chapter will focus on determining the thermal diffusivity of the flame sprayed thermal barrier coating, TBC, to allow comparisons between the TBC and CCD. Later chapters of this investigation will address the impacts of the TBC on HCCI combustion and CCD accumulation.

Flame sprayed TBC are known to undergo changes to their thermal properties due to heat cycling and subsequent sintering/densification of the coating [107]-[109]. However, the temperatures necessary to influence the structure of a zirconium-based TBC are above 1100ºC, and the TBC must be exposed to those temperatures for a period of hours [107], [108]. The magnesium zirconate, MgZr, coating used in this study neither reaches the 1100ºC threshold temperature nor sustains that temperature for appropriate time periods to succumb to sintering effects.

The MgZr coating was composed of 76% Zirconium Oxide with 24% Magnesium Oxide infused to stabilize the crystalline structure. The MgZr was chosen for its low conductivity value, ~1.5 W/(m-K) [110]. A TBC thickness of 100μm was selected based on the piston CCD thicknesses observed in previous work [12]. To avoid complications arising from the extreme difference in thermal expansion coefficients between the substrate material and the MgZr coating, a ~50μm stress relief coating of a nickel alloy was applied beneath the MgZr. The nickel alloy was 75% nickel with the balance composed of aluminum, chrome and yttrium and had a thermal conductivity value near 60W/(m-K).

In order to quantify the thermal properties of the final MgZr coating, a heat flux probe was coated with both the 150μm MgZr and nickel alloy stress relief layer used on the piston. The total thickness of the MgZr-Ni construct measured 210μm. Additionally, a second heat flux probe was coated with just the nickel stress relief layer so that the properties of the nickel layer could be calculated and the relative impact of the nickel layer on the final construct studied. The thickness of the nickel alloy layer was measured to be 60μm. The MgZr-Ni and Ni alloy probes are shown in Figure 5.1.

Figure 5.1 – Heat flux probes coated with MgZr with a nickel sub-layer (left) and the nickel layer alone (right)

5.1 Radiation Transparency of the Magnesium Zirconate Coating

Figure 5.2 shows the ex-situ temperature and heat flux traces for the MgZr coated heat flux probe. No measurable sub-TBC phase delay is present, suggesting that the MgZr layer is semi-transparent and therefore allowing the radiation pulse to pass directly through the sample. The semi-transparent behavior of similar zirconium coatings has been noted by other researchers [97]-[99].

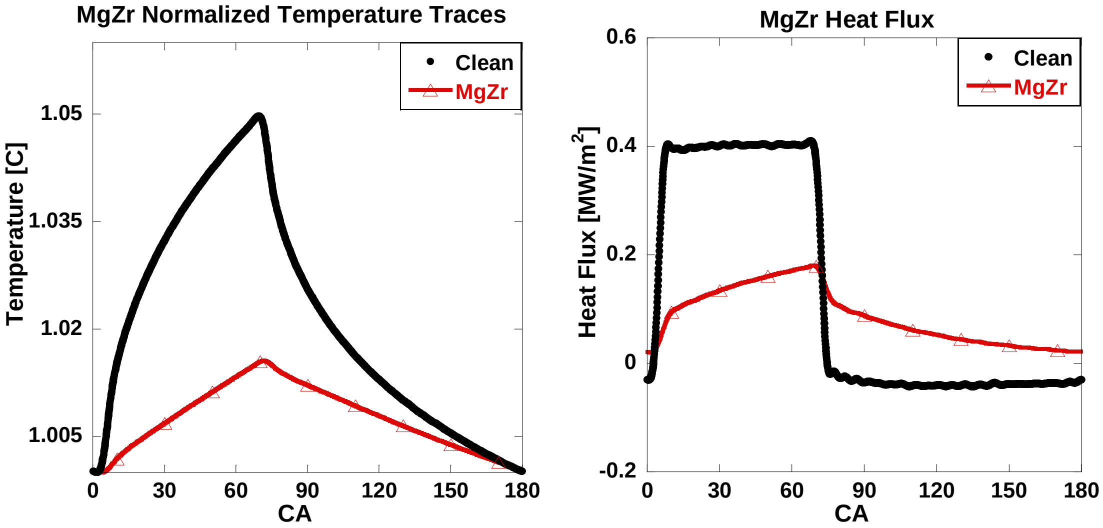

Figure 5.2 – Sub-MgZr temperature and heat flux profiles exhibiting radiation transparency

Graphite aerosol was applied to the surface of the MgZr heat flux probe to mitigate the transparency effect. Figure 5.3 shows the sub-MgZr temperature and heat flux traces with graphite applied to the surface. A distinct phase delay is now present in the temperature trace, which can be used to calculate the diffusivity of the conglomerate MgZr-Ni coating.

The ex-situ diffusivity of the MgZr-Ni coating was calculated, Figure 5.4. Each MgZr data point represents the average of 400 individually calculated diffusivities. There are three data points plotted for each chopping wheel speed. The conglomerate MgZr-Ni diffusivity is similar to that of monolithic zirconium and is greater than any CCD diffusivity calculated from the cylinder head probes in-situ from this work and in [11].

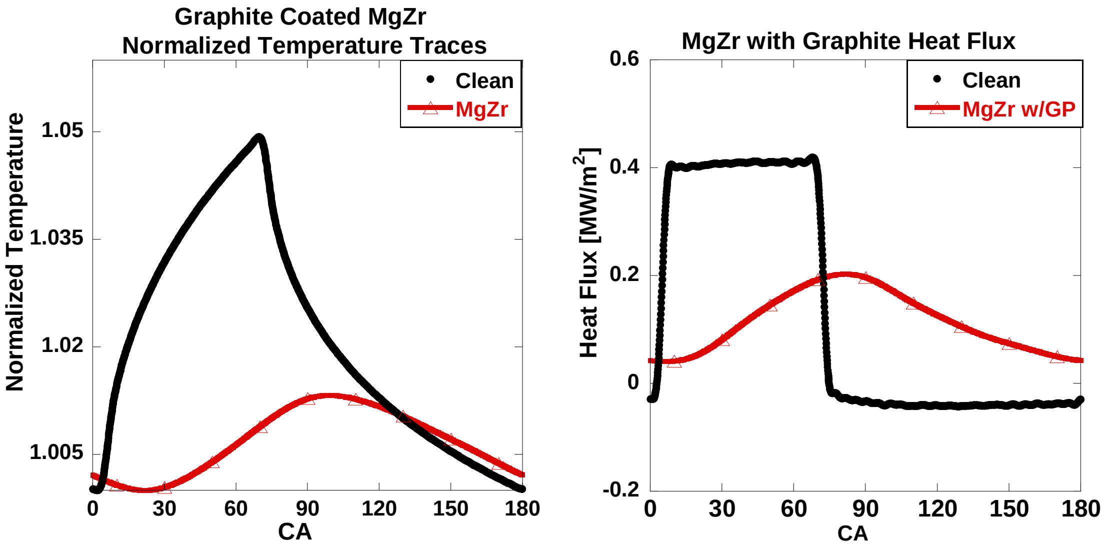

Figure 5.3 – Sub-MgZr temperature and heat flux profiles with graphite applied to minimize transparency

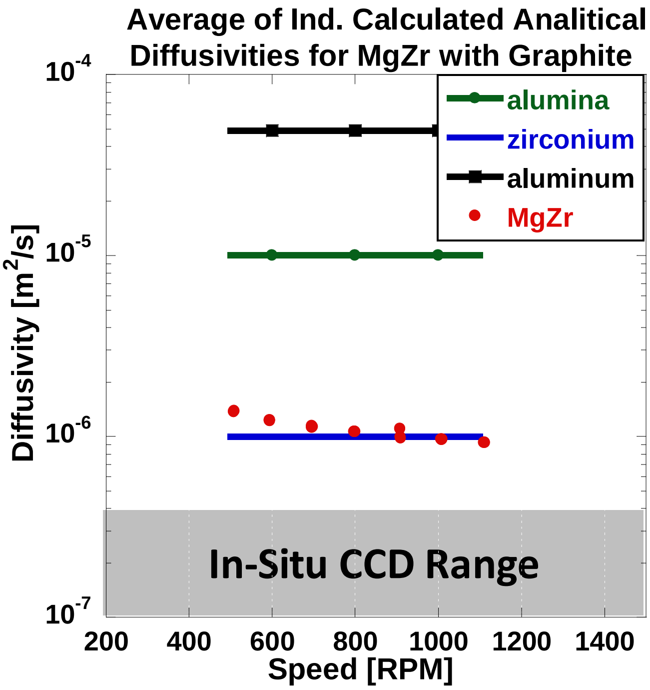

Figure 5.4 – MgZr ex-situ diffusivity calculated using the combined thickness of both the MgZr and Ni alloy coatings

5.2 Removing the Impact of the Nickel Alloy Stress Relief Layer

To isolate the properties of the MgZr, the heat flux probe coated with only the nickel alloy was tested ex-situ with graphite applied to its surface, Figure 5.5. The measured temperature phase delay induced by the nickel alloy is approximately one percent of the total phase delay measured for the MgZr-Ni conglomerate and is therefore negligible.

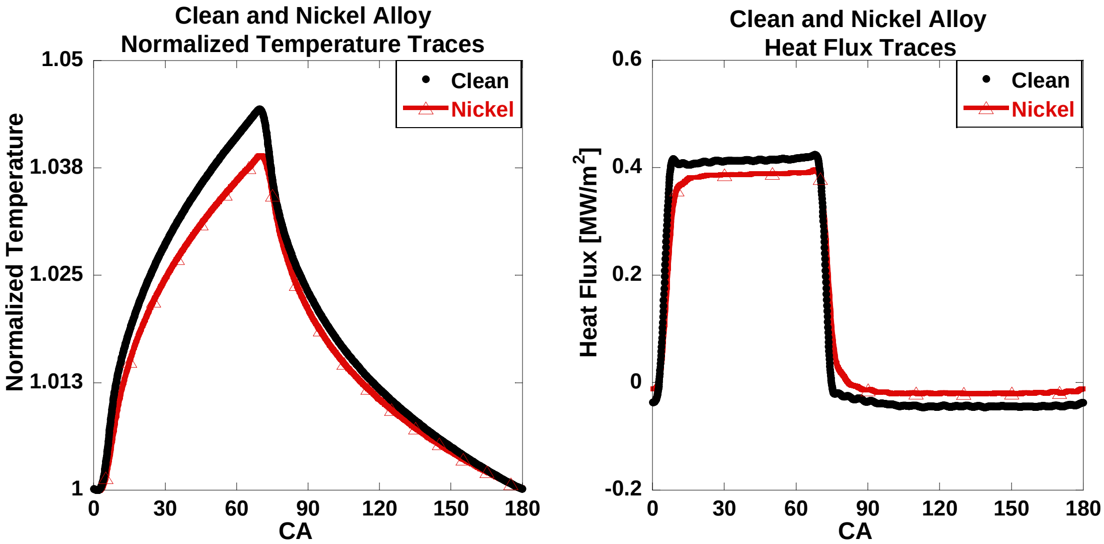

Figure 5.5 – Sub-nickel alloy temperature and heat flux traces illustrating the negligible impact of the nickel alloy stress relief layer on the sub-TBC phased delay

Subtraction of the nickel alloy’s 60μm thickness from the total thickness of the MgZr-Ni conglomerate effectively removed the impact of the nickel layer from the diffusivity analysis. This thickness subtraction produced an isolated MgZr diffusivity trend, “MgZr 150μm” in Figure 5.6, lower than that of the MgZr-Ni conglomerate.

To further validate the negligible impact of the nickel alloy layer on the calculated MgZr diffusivity, both the temperature phase delay and the thickness of the nickel layer were removed from the overall phase delay and thickness of the MgZr-Ni conglomerate during diffusivity calculations, respectively. The results of this exercise are represented by the “MgZr phased” trend in Figure 5.6. The MgZr diffusivity produced with this technique was within a percent of the MgZr diffusivity calculated without accounting for the phase delay impact of the nickel alloy. This exercise proved that simply subtracting the nickel thickness from the conglomerate thickness effectively isolated the diffusivity of the MgZr layer. Overall, the average ex-situ MgZr diffusivity when isolated from the nickel sub-layer was determined to be 5.7x10^{-7}m^2/s.

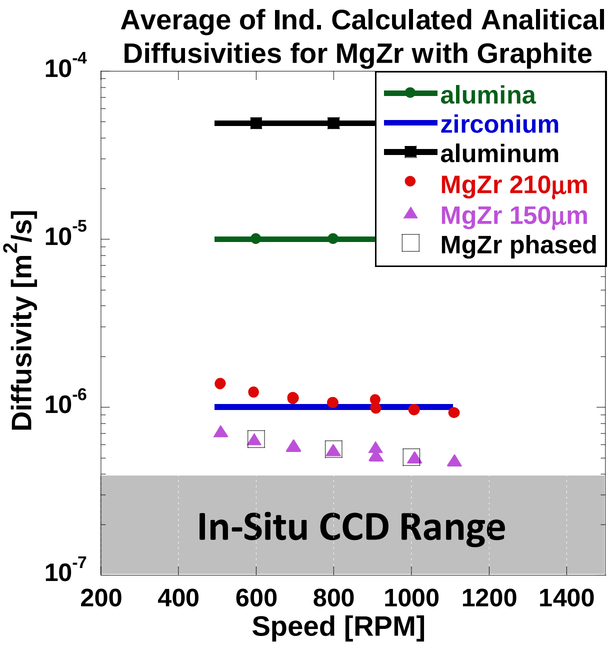

Figure 5.6 – Isolation of the MgZr diffusivity by removing the impact of the nickel alloy sub-layer

5.3 The Impact of Fuel on Magnesium Zirconate Diffusivity

Flame sprayed coatings are considered a series of overlapping splats [101] with gas permeable porosity [92]. However, the previous chapter analytically eliminated the penetration of the porosity network by air of pressures varying from 1-40bar as a cause for the discrepancies between ex-situ and in-situ diffusivities. With the elimination of compressed air effects, the presence of fuel during firing operation is the only factor remaining that differentiates the in-situ firing and motoring conditions.

MgZr diffusivities were calculated during both in-situ firing and in-situ motoring operation. To maintain consistency with the ex-situ results, aerosol graphite was applied to the MgZr prior to the in-situ testing. The response of a clean cylinder head heat flux probe was then compared to that of the graphite coated MgZr coated probe prior to any CCD accumulation. Combustion phasing was matched for the clean probe and MgZr probe in-situ cases on an ensemble basis. However, the clean heat flux probe and the MgZr coated probe could not occupy the same location within the combustion chamber at the same time. Therefore, the clean and MgZr coated probe data used to determine the temperature phase delay of the MgZr were from separate 200 cycle measurements. For these reasons, the temperature traces utilized for the in-situ diffusivity calculations were ensemble averages of 200 individual cycle temperature traces.

A comparison of the diffusivities collected during the three diffusivity measurement methods is shown in Figure 5.7. The ex-situ MgZr diffusivity is the average of the diffusivities calculated from 8400 individually heat flux pulses and the corresponding error bar represents their standard deviation. The in-situ results are singular diffusivity values calculated from ensemble averaged temperature traces, so their error bars have been omitted. The firing and motoring in-situ diffusivity values are 47% and 48% of the ex-situ diffusivity value, respectively.

Due to the similarity of in-situ firing and in-situ motoring MgZr diffusivities, it can be concluded that the interaction of fuel with the MgZr coating does not impact the in-situ MgZr diffusivity. Fuel interactions with the MgZr morphology are removed from culpability for the difference between ex-situ and in-situ diffusivities.

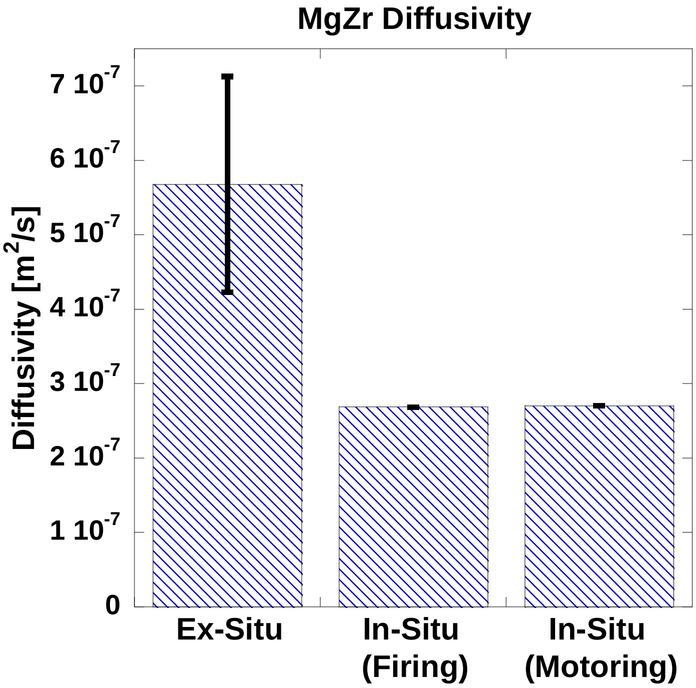

Figure 5.7 – MgZr diffusivities determined during ex-situ, in-situ firing and in-situ motoring operation showing the close agreement between the two in-situ results

5.4 Penetration of Radiation Heat Flux into the Magnesium Zirconate Coating

A factor which could create the discrepancy between ex-situ and in-situ results is the penetration of the ex-situ radiation pulse into the MgZr coating, as previously discovered for CCD. Conceptually, the MgZr coating morphology is similar to the CCD layer. Figure 5.8 displays a theoretical sketch of the MgZr coating with graphite applied to its surface. The flame spray process deposits layers of sputtered ceramic material which build upon each other to create the final coating.

As with thick CCD, the MgZr layer contains porosity which allows a portion of the radiation pulse to penetrate into the MgZr coating. Accordingly, a portion of the radiative heat flux experiences the delay of the entire MgZr thickness, and some radiation traverses a lesser MgZr thickness. The porosity allows light and radiation to penetrate, but the convective heat transfer experienced in-situ cannot, creating the discrepancy between ex-situ and in-situ diffusivities.

The aerosol graphite applied to minimize radiation transparency is represented in Figure 5.8 as a thin layer of particles coating the total surface area of the MgZr layer. The total surface area is the cross sectional area of the layer and the additional surface area provided by the accessible pores. The conceptual representation of the aerosol graphite as particles of much smaller size than the MgZr porosity is reinforced by the minimal influence of the graphite coating on the measured sample thickness, as presented earlier in this work. Even if the graphite were to partially fill the pores of the MgZr layer, the conductivity of graphite powder is orders of magnitude greater than the MgZr (ranging from 161–209 W/mK [111] and [112]), and the thickness of the graphite is orders of magnitude less than the MgZr thickness. Thus, the graphite would only negligibly impact the measured temperature phase delay.

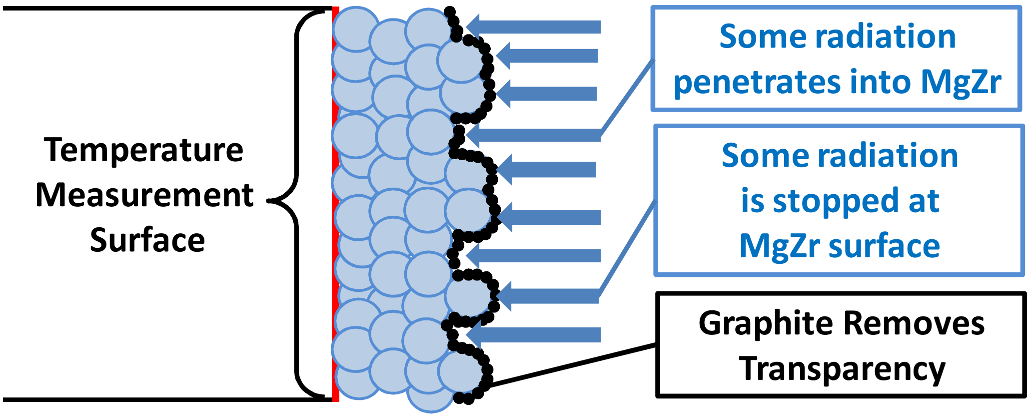

Figure 5.8 – Conceptual diagram of the MgZr coating illustrating the penetration of radiation into the surface porosity

With CCD, a radiation penetration factor was found by transposing the ex-situ phase delay data onto the in-situ trendline of phase delay versus thickness. Similarly, subtracting 32µm from the MgZr thickness allows the ex-situ diffusivity results to coincide with the in-situ average. This establishes the MgZr radiation penetration factor as 32μm. However, there are only one ex-situ and two in-situ data points for the MgZr study, an admittedly small sample.

5.5 Porosity of the Magnesium Zirconate Coating

The 32μm radiation penetration factor for MgZr is 2.5 times higher than the 13μm factor calculated for CCD. The radiation penetration factor represents the sample thickness which has been negated by penetration of the radiation pulse into the effective porosity of the coating. If the depth of the CCD and MgZr pores is the same, then the ratio of the two radiation penetration factors shows that the MgZr has 2.5 times more of those pores present. Conversely, if the quantity of pores on the MgZr and CCD surfaces is the same, then the line-of-sight depth of the MgZr pores must be 2.5 times greater. These two scenarios use the radiation penetration factor to define constraints on the possibilities for the porosity of the MgZr and CCD. In this manner, the ratio of the radiation penetration factors is an effective measure of the relative impact of porosity for the two materials.

5.6 Conclusions and Contributions from the Magnesium Zirconate Diffusivity Determination

It was determined that the nickel alloy stress relief layer has a negligible impact on the sub-TBC temperature phasing. The nickel thickness was subtracted from that of the MgZr-Ni conglomerate to determine the thermal diffusivity of just the MgZr.

MgZr was found to be partially transparent to the ex-situ radiation pulse. Application of a graphite opacity layer minimized the transparency and allowed an ex-situ diffusivity determination.

The ex-situ MgZr diffusivity value was approximately twice the magnitude of the values determined in-situ. In-situ motoring and firing MgZr diffusivities were within one percent of each other showing that fuel-MgZr interaction plays a negligible role in MgZr diffusivity determination.

Due to the flame spray process, MgZr has line-of-sight pathways, which allow some of the radiation pulse to penetrate into the MgZr thickness and increase the MgZr diffusivity value by reducing the sub-MgZr phase delay. The radiation penetration factor for MgZr was determined to be 32µm, nearly 2.5 times that of CCD. This implies that MgZr has an effective porosity 2.5 greater than CCD.

CHAPTER 6

THE IMPACT OF A MAGNESIUM ZIRCONATE COATED PISTON ON CCD ACCUMULATION AND HCCI OPERATION

The ability of accumulated CCD to act as a thermal barrier and impact HCCI operability limits has been previously established [12] and [13]. The CCD provided a downward shift in the load-based HCCI operational range and allowed the utilization of HCCI combustion at low load points where the relative efficiency benefits of HCCI were at a maximum over the use of a severely throttled, stoichiometric, spark-ignited charge.

Since CCD accumulation is dependent upon combustion chamber wall temperature [115], altering the wall temperature through the application of a thermal barrier coating should impact subsequent CCD accumulation, and, in turn, affect the difference in operability limits between clean and conditioned chamber states. If the difference in operability maps between clean and conditioned chamber states can be reduced through the utilization of a thermal barrier coating, TBC, then the variability induced by CCD has effectively been reduced.

This investigation utilizes a piston coated with a flame sprayed magnesium zirconate, MgZr, thermal barrier coating in an attempt to mitigate the operational variability caused by CCD accumulation. The properties of this coating were studied in the previous chapter.

Before the coating and the nickel alloy stress relief layer were applied, an additional 150μm was machined from the piston to maintain compression ratio and preserve the basis of comparison between the baseline metal piston and the MgZr coated piston. Figure 6.1 shows the HCCI piston with the MgZr and nickel alloy layers applied.

Figure 6.1 – Piston coated with 100μm MgZr and an intermediate nickel alloy layer for stress relief

6.1 Impact of a Magnesium Zirconate Coated Piston on Combustion Chamber Deposit Accumulation

Both the metal and MgZr coated pistons were subjected to a cycle of passive conditioning. At the onset of these conditioning runs, the HCCI operability range was established with all combustion chamber components clean. Subsequently, the engine described in Chapter 2 was operated at a constant operating condition (11mg fuel, wide open throttle, 20:1 air:fuel, $T_{coolant} = T_{oil} = 95°C$, $T_{intake} = 90\ °C$) and CCD were allowed to accumulate. The passive conditioning was continued until the combustion advance associated with increasing CCD accumulation ceased. The point where CCD accumulation halted is herein referred to as the “conditioned” chamber state. The operability range was then re-established with the fully conditioned chamber.

6.1.1 Combustion Chamber Deposit Accumulation on the Piston

The engine was disassembled at the culmination of each test to map the CCD accumulation. This accumulation is shown in Figure 6.2. The thicknesses shown are averages of twelve Dualscope measurements at each location. In the case of the MgZr coated piston, the MgZr coating thickness was first mapped with the Dualscope and then subtracted from measurements taken at the conclusion of the passive conditioning cycle to determine the CCD thicknesses.

The qualitative distribution of CCD on the piston is similar regardless of the piston used. The large flat surfaces on the periphery of the piston, the “squish” region, form deposits that are thin compared to those in the bowl. The CCD on the squish region of the MgZr piston are grey in appearance rather than the typically black CCD seen with a metal piston. The bowl deposits in the MgZr case are black with brown color appearing on high spots in the CCD topography and on the exposed edges of flakes in the CCD layer.

In both cases, the bowl experiences thick CCD accumulation with large gradients in thicknesses in the area of spray impingement. (The spray strikes the piston from the center of the left side in this view and progresses downward and to the right across the bowl.) The impingement leaves a spray jet shape in the thick bowl CCD and by eroding away some CCD.

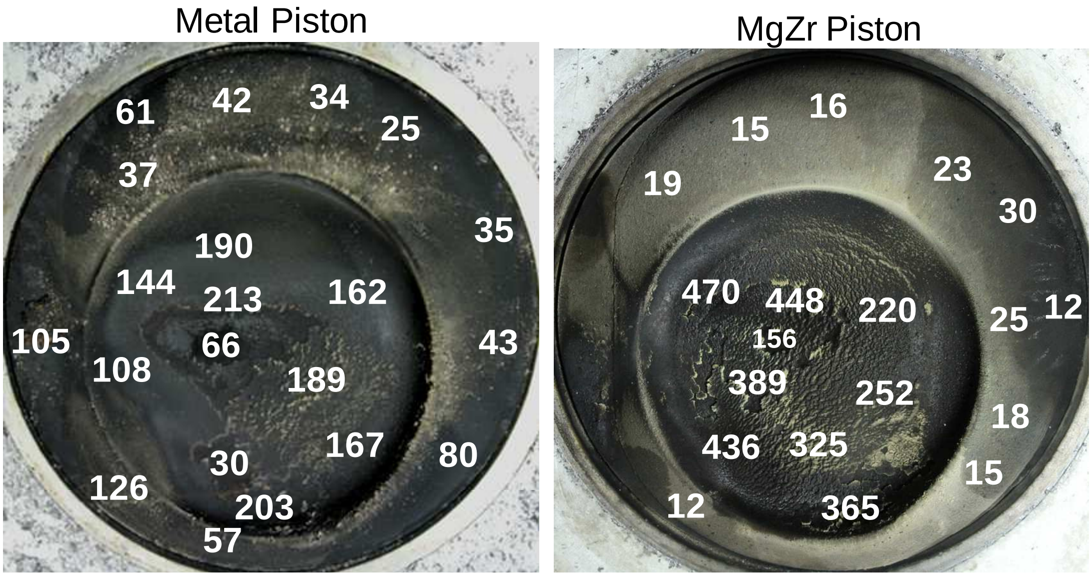

Figure 6.2 – CCD accumulation on metal and MgZr pistons due to passive conditioning (thicknesses in micrometers)

The thick CCD accumulation in the piston bowl is due to the presence of a liquid fuel layer. The presence of liquid fuel layers has been directly correlated to rapid CCD formation by Campbell et al [113]. Where liquid fuel is present, thick CCD can form from either liquid phase auto-oxidation, for temperatures <350ºC, or from supercritical pyrolysis, for temperatures >425ºC [114].

Quantitatively, the two pistons show distinct differences in CCD accumulation. The metal piston has thicknesses on the order of 25-60μm on the periphery while the majority of the bowl surface has 100-200μm of CCD accumulation. This is in stark contrast to the MgZr piston, which accumulates ~50% less CCD on the periphery, 10-30μm, and a far greater CCD thickness in the bowl, 200-450μm.

The periphery “squish” surfaces of the MgZr piston experienced lower CCD accumulation due to increased surface temperature provided by the reduced conductivity and diffusivity of the MgZr relative to aluminum. For more on the impact of increased surface temperature and its propensity to reduce CCD accumulation see the work of Cheng [115] and Nakic [41].

Differences in fuel spray dynamics are speculated to cause the disparity in CCD thickness between the two piston bowls. Surface porosity has been shown to affect local flows and mixing [45], [46]. The MgZr coating has exposed porosity and surface roughness, which can alter the pooling effect of impinging fuel. The roughness of the MgZr slows the fuel momentum as the spray traverses the bowl. The exposed porosity has the potential to trap a greater quantity of fuel than what would have wetted the surface of the smooth metal piston. Thus, the MgZr experiences greater fuel pooling than the metal piston, providing a pathway to greater CCD growth.

6.1.2 Combustion Chamber Deposit Accumulation on the Cylinder Head

The head side CCD accumulation was also affected by the MgZr piston, Figure 6.3. For these photos, the exhaust ports are on the left and the injector is on the right for each case. The CCD thicknesses are an average of twelve Dualscope measurements and are shown in micrometers. The thicknesses in black located slightly off each picture represent CCD thicknesses on features which are into the plane of the picture. The labels “H1” and “H2” denoted the locations of the two cylinder head heat flux probes.

While cylinder head CCD thicknesses on the extreme exhaust side (left) and the beach-like region near the injector are similar between the two cases, all other measurement areas show reduced CCD accumulation due to operation with the MgZr piston. In many instances the reduction of CCD thickness was ~50% and is attributed to the altered fuel dynamics caused by the roughness of the MgZr piston. With more fuel slowed by the MgZr surface roughness and trapped in the porosity of the MgZr piston bowl, the charge equivalence ratio near the cylinder head is leaner, producing less CCD accumulation. For more information regarding the influence of charge equivalence ratio on CCD accumulation see the work of Cheng [40].

As with the piston CCD comparison, the CCD accumulated on the head are greyer in appearance with the MgZr piston than those formed with the metal piston. This difference in color is due to the light penetration behavior of thin CCD as noted earlier in this work.

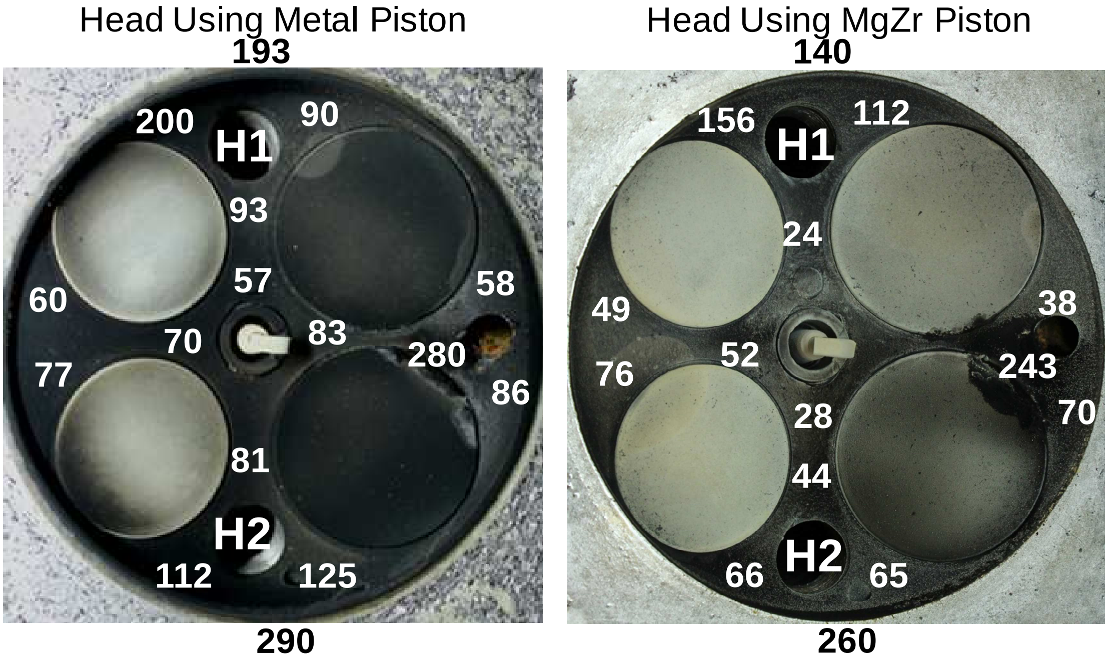

Figure 6.3 – CCD accumulation on the head of the combustion chamber due to passive conditioning tests with metal and MgZr pistons (thicknesses in micrometers)

6.1.3 Combustion Chamber Deposit Accumulation on the Cylinder Head Heat Flux Probes

CCD thicknesses for the head heat flux probes located at H1 and H2 are shown in Figure 6.4. As with the cylinder head CCD thicknesses, Head Probe Location #1 experiences reduced CCD accumulation during passive conditioning with the MgZr piston. The CCD accumulated on Head Probe #1 while operating with the MgZr piston are qualitatively similar to CCD of like thickness accumulated with a metal piston. The outline of the temperature measurement surface is visible through the CCD layer, and the CCD have a grey appearance with yellow-brown topographical features.

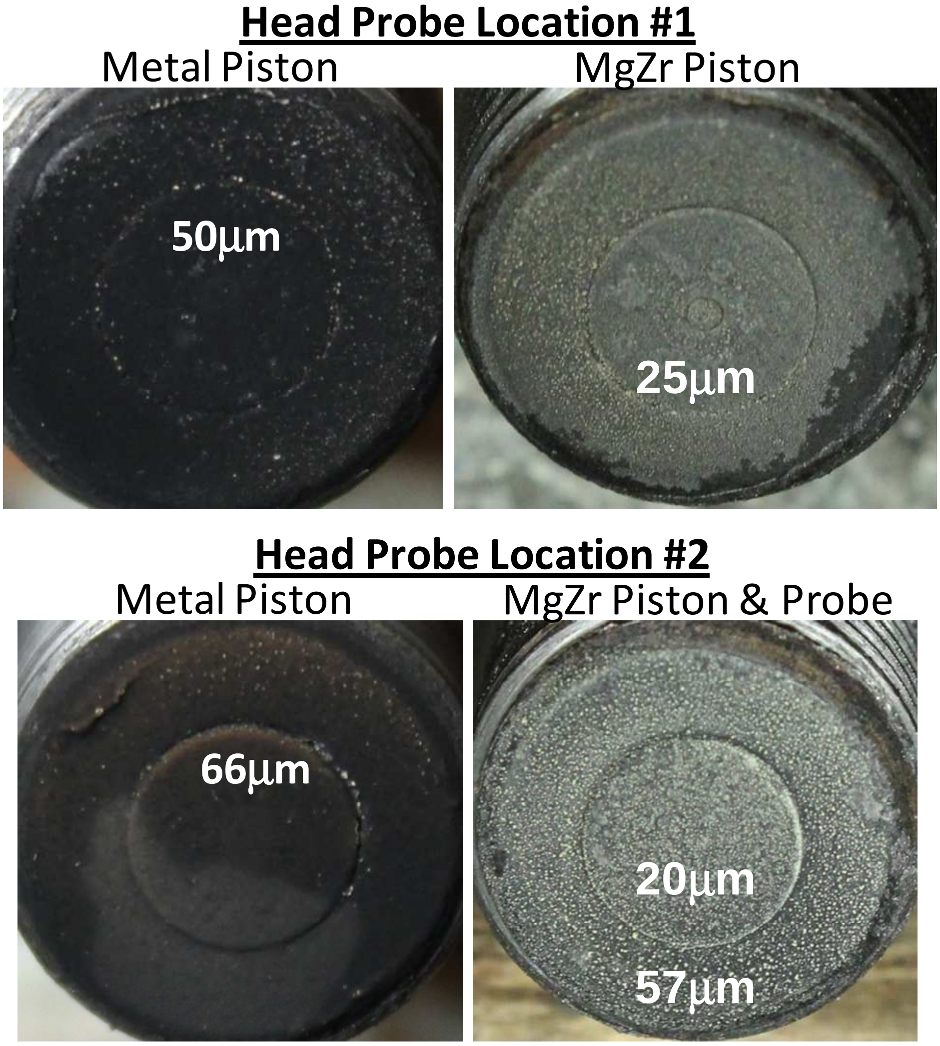

Figure 6.4 – CCD accumulation on the head heat flux probes after passive conditioning tests with metal and MgZr pistons

During operation with the MgZr piston, Head Probe #2 was coated with 150μm of MgZr and 50μm of the stress relieving nickel alloy. Therefore, two thicknesses are reported at this location for the MgZr case: the CCD thickness on the MgZr probe and the CCD thickness on the surrounding mounting sleeve. The MgZr coating applied to Head Probe Location #2 reduced the CCD accumulation by 65% relative to the surrounding mounting sleeve because of the elevated surface temperature of the MgZr.

Qualitatively, the 57μm CCD on the mounting sleeve at Head Probe Location #2 exhibit a greyish appearance with distinct, yellow-brown topographical features, while

CCD of this thickness regime formed with a metal piston are black in color with a smoother topography. This discrepancy in appearance suggests that CCD formed during operation with a MgZr piston were formed from different conditions, reinforcing the hypothesis that the charge is leaner near the cylinder head due to the surface roughness of the MgZr piston. Additional testing will be necessary to prove this hypothesis, which is beyond the scope of this study.

6.2 Impact of the Magnesium Zirconate Coated Piston on HCCI Operation

The MgZr piston affects the CCD accumulation associated with passive conditioning throughout the combustion chamber. Thus, the MgZr piston has the potential to create differences in the HCCI operability range. This section will assess the ability of the MgZr coated piston to reduce the HCCI operational variability imposed by CCD accumulation.

6.2.1 Impact of the Magnesium Zirconate Piston on the Combustion Phasing Variability Induced by Combustion Chamber Deposit Accumulation

Figure 6.5 shows the advance in heat release associated with passive conditioning runs with both the baseline metal combustion chamber and with the MgZr coated piston. The MgZr piston reduces the operational time necessary for the combustion chamber to reach its fully conditioned state from 33 hours to 22 hours. Meanwhile, the amount of combustion advance experienced by the engine during conditioning was reduced by ~39% from 7.5 CA to 4.6 CA.

The rate of phasing change serves as an indication of the engine’s sensitivity to the conditioning process. Mitigating the rate of combustion phasing change associated with CCD accumulation is important to stable HCCI operation in a practical engine. With a 7.5 CA advance over 33 hours, the metal chamber has rate of phasing change of 0.23CA/hour. The MgZr piston slightly reduces this rate of change to 0.21CA/hour.

While this reduction is slight, the impact of the MgZr piston is in the direction of additional operational stability. Combine this with the reduction of CCD induced combustion phasing advance and the MgZr piston proves that thermal barrier coatings have the potential to reduce the variability created by CCD in a practical multi-mode engine.

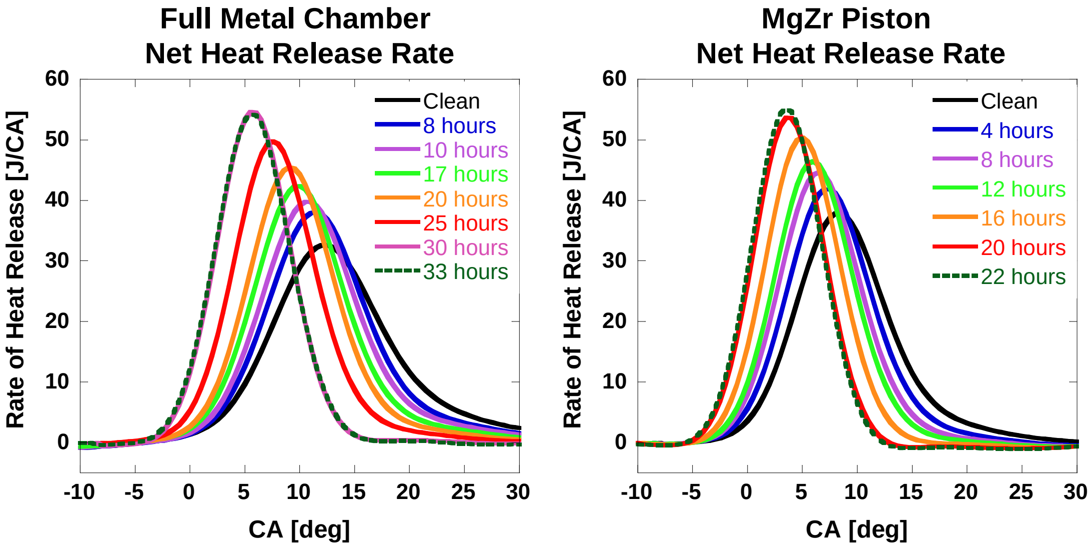

Figure 6.5 – Influence of MgZr piston on net heat release during passive conditioning

Although the MgZr piston creates an advance in combustion phasing, the interaction of the MgZr porosity with the fuel spray increases the combustion duration, Figure 6.6. The midpoint of the mass fraction burn, CA50, is not impacted by the MgZr piston beyond the influence of advancing ignition timing, CA10. However, the combustion duration, CA10-90, is increased by the MgZr piston relative to the metal piston.

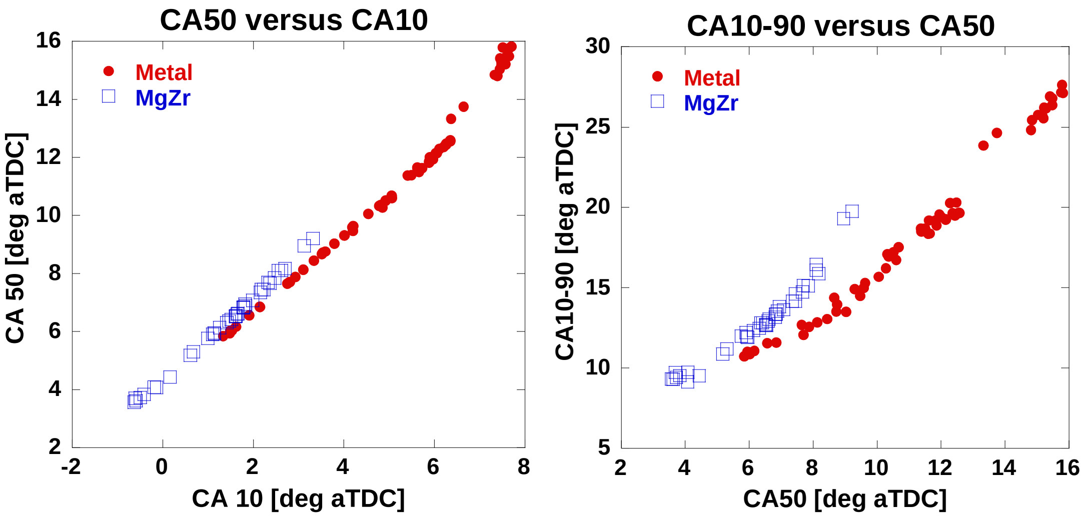

Figure 6.6 – Combustion phasing versus ignition (left) and burn duration versus combustion phasing (right) illustrating the increase in CA50-90 burn duration due to the MgZr piston

Other researchers have implicated the interaction of fuel with the porosity of coated combustion chamber parts as the cause for this increase in combustion duration [45], [46], while analysis earlier in this study has shown that fuel and compressed air interactions with the MgZr porosity do not wield influence over MgZr diffusivity values. However, the heat flux probe sued for that analysis was located on the cylinder head. Therefore, it can only be concluded that any adsorption-desorption interactions between fuel and the MgZr porosity are not present on the cylinder head.

Evidence does suggest that significant interaction between the fuel and MgZr occurs on the piston. The increased fuel pooling within MgZr the bowl caused by interactions between the DI fuel spray and the surface roughness/porosity of the MgZr coating leads to increased CCD accumulation within the MgZr piston bowl. Additionally CCD thicknesses on the cylinder head due are reduced during operation with the MgZr piston. These facts suggest a stratification of equivalence ratio within the combustion chamber due to the surface roughness of the MgZr piston. The compositional stratification of the charge extends the burn duration during operation with the MgZr piston in accordance with the findings of [29] and [30].

6.2.2 Impact of the Magnesium Zirconate Piston on HCCI Operability Limits

HCCI operability is limited at high loads by extreme pressure rise rates. The rate of pressure rise within the cylinder creates pressure waves which, at moderate intensity, create unwanted acoustic noise and, at higher levels, create pressure waves which can damage the engine components [24]. For this investigation, the high load limit is set at a pressure rise rate of 50bar/msec.

The low load limit of HCCI combustion is created by a lack of thermal energy within the combustion chamber. Thermal energy is added to the cylinder by heating the intake air to 90ºC and inducing internal residuals of ~40% supplied by the rebreathing exhaust cams. In spite of these efforts, the coefficient of variance in the engine's indicated mean effective pressure, COV_{IMEP}, eventually reaches levels noticeable by a consumer as load is decreased. For this investigation, the low load limit is established at $COV_{IMEP} = 3.0$.

The shift in operability range created through the accumulation of CCD can be a useful in extending the range of high efficiency HCCI combustion towards low load points of interest in fuel economy evaluation cycles. Figure 6.7 shows the impact of the MgZr piston on the HCCI operability range relative to a full metal combustion chamber in both clean and conditioned states.

The MgZr piston, prior to CCD accumulation, shifts the HCCI operability range toward lower loads and captures much of the load shift gained through passive CCD accumulation in a full metal chamber. As CCD accumulate during operation with the MgZr piston, the HCCI operability range shifts to loads lower than those which are attainable with a conditioned metal piston.

The reduced variability offered by the MgZr piston is qualitatively illustrated by the large overlap of its clean and conditioned operability ranges. The area of overlap is greater with the MgZr piston than with an all metal combustion chamber.

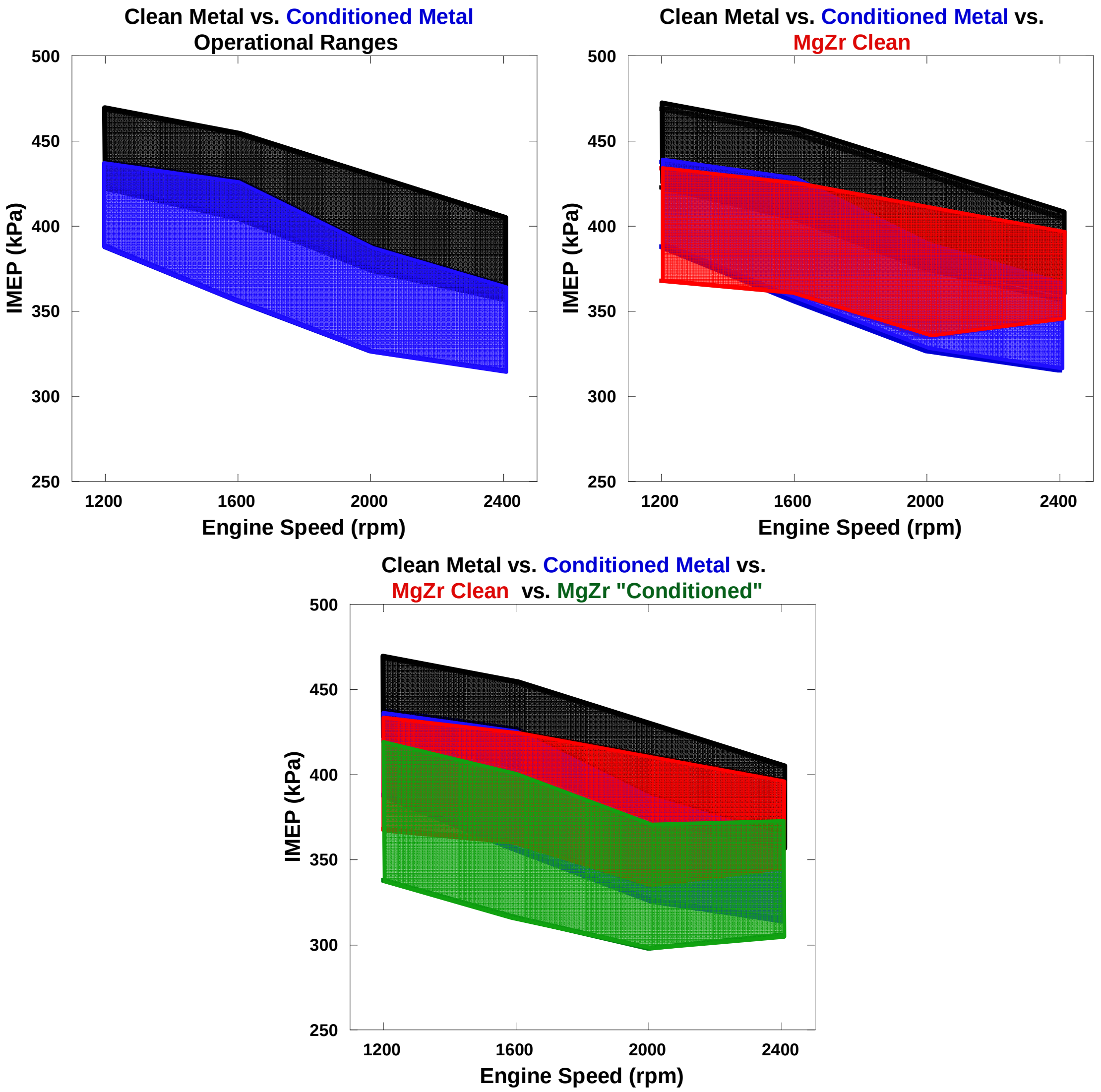

Figure 6.7 – HCCI operability range comparison for metal and MgZr pistons in clean and fully conditioned chamber states

6.3 Conclusions and Contributions of the Magnesium Zirconate Piston Testing

6.3.1 The Impact of a Magnesium Zirconate Coated Piston on Combustion Chamber Deposit Accumulation

The MgZr piston experienced reduced CCD accumulation on the periphery compared to its metal counterpart. However, CCD in the piston bowl were thicker for the

MgZr piston. The MgZr surface roughness and open porosity were speculated to impact the fuel spray during DI spray impingement and increase the amount of fuel pooling within the bowl, creating the measured increase in bowl CCD thickness.

Head side CCD accumulation was also reduced during operation with the MgZr piston. This reduction was attributed to the altered piston bowl fuel dynamics due to the MgZr surface roughness. Theoretically, the increased fuel pooling in the piston bowl created equivalence ratio stratification within the charge. The charge near the cylinder head was leaner with the MgZr piston than with a metal piston, reducing CCD accumulation on the cylinder head.

The MgZr coating on heat flux probe location #2 provided a 65% reduction in CCD accumulation. The 57μm CCD accumulated on the head probe sleeve at location #2 during operation with the MgZr piston had similar qualitative features to CCD of ~30μm formed during operation with a metal piston, providing further evidence of a different head side CCD accumulation process due to the MgZr piston.

6.3.2 The Impact of Magnesium Zirconate Coated Piston on HCCI Operation

Installation of the MgZr piston into a clean combustion chamber shifts the HCCI operability range to lower loads, nearly fully accounting for the difference in operability created by a conditioned metal chamber. The shift in combustion phasing experienced during MgZr piston conditioning was 39% less than the shift in combustion during conditioning of a full metal combustion chamber. In addition, the rate of combustion phasing change due to CCD accumulation was slightly reduced during operation with the MgZr piston. Thus, when compared to operation with all metal combustion chamber components, utilization of the MgZr piston reduced the operational variability of, and increased operational stability during, CCD accumulation.

HCCI combustion duration was extended beyond the impact of combustion phasing by the MgZr piston. Increased fuel pooling within the piston bowl was created by the increased surface roughness and exposed porosity of the MgZr piston. The fuel pooling within the bowl leaned the remaining portions of the charge and induced equivalence ratio stratification, which, in turn, extended the combustion duration.

CHAPTER 7

CONCLUSIONS, CONTRIBUTIONS AND RECOMMENDATIONS FOR FUTURE WORK

This investigation began with refinements to the ex-situ radiation chamber hardware and methodology. Subsequently, an accuracy assessment of the radiation chamber was conducted with materials of known diffusivity.

The thermal diffusivity of CCD formed during HCCI combustion was then determined in-situ and ex-situ. The impacts of fuel-CCD interactions, CCD radiation transparency, compressed air within CCD porosity, and the penetration of radiation into CCD were all characterized by their ability to influence in-situ and ex-situ CCD diffusivity.

A similar characterization was conducted for a flame-sprayed magnesium zirconate thermal barrier coating and led to comparisons between the magnesium zirconate and CCD. The ability of thermal barrier coatings to limit the combustion variability associated with CCD accumulation was studied through a passive conditioning cycle with magnesium zirconate applied to the piston. The impact of the MgZr piston on HCCI operability and CCD accumulation were also determined.

This chapter will summarize the conclusions and contributions of this research and then supply recommendations for future work.

7.1 Summary of Conclusions

7.1.1 Radiation Chamber Development

- The accuracy of the radiation chamber methodology was evaluated by testing wafers with known thermal properties.
    - The diffusivities calculated by the ex-situ radiation chamber were independent of sample thickness.
    - Ex-situ diffusivities exhibited a slight but consistent underprediction for all thicknesses of all materials tested. This underprediction was attributed to contact resistance at the interface of the sample and the temperature measurement surface.

7.1.2 Combustion Chamber Deposit Thermal Diffusivity

- A comparison of diffusivities calculated during in-situ motoring and in-situ firing operation showed that fuel-CCD interactions had a negligible impact on CCD diffusivity for CCD accumulated on the cylinder head heat flux probes.
- CCD exhibited a partial transparency to the ex-situ radiation pulse.
- CCD allowed penetration of the ex-situ radiation pulse due line-of-sight pathways in their accumulated structure. These pathways were provided by both the porosity of the CCD layer and the sparse nature of CCD during initial accumulation.
    - For CCD thicknesses less than 30μm, the sparse nature of initial CCD accumulation allowed radiation to penetrate straight to the temperature measurement junction of the heat flux probe. This produced low ex-situ phase delays and high ex-situ diffusivities.
        - The in-situ convection heat transfer could not penetrate into these pathways, which created the stark difference between ex-situ and in-situ diffusivity results for CCD less than 30μm. The difference between ex-situ and in-situ

    results confirmed that radiation is not a significant heat transfer mode in HCCI combustion.

  - For CCD thicknesses > 30μm, the line-of-sight pathways penetrated only part way into the CCD thickness via open porosity. Thus, some of the radiation pulse experienced the thermal resistance of only a portion of the CCD thickness, reducing measured sub-CCD temperature phasing and increasing ex-situ diffusivities.
  - A radiation penetration factor was defined as the thickness of material whose insulating impact had been negated by radiation penetration. This factor was calculated by shifting the ex-situ phase delay onto the in-situ phase delay trend for CCD thicknesses > 30 μm. The radiation penetration factor represents the effective porosity of the CCD surface.
    - The radiation penetration factor for CCD was 13μm.

7.1.3 Characterization of the Magnesium Zirconate Thermal Barrier Coating

- The nickel alloy stress relief layer beneath the MgZr had a negligible effect on the sub-TBC temperature phasing. The nickel thickness was subtracted from that of the MgZr-Ni conglomerate to isolate the thermal diffusivity of the MgZr.
- MgZr exhibited transparency to the ex-situ radiation pulse.
- In-situ motoring and in-situ firing MgZr diffusivities were within one percent, which proved that fuel-MgZr interaction had a negligible impact on the diffusivity of the MgZr coated probe mounted in the cylinder head.
- MgZr porosity was assumed to supply line-of-sight pathways into the MgZr thickness. The pathways allowed penetration of the radiation pulse into the MgZr thickness and increased the ex-situ diffusivity value by reducing the sub-MgZr phase delay.

  - The radiation penetration factor of MgZr was determined to be 32µm. Thus, the MgZr had 2.5 times the effective porosity of CCD.

7.1.4 The Impact of a Magnesium Zirconate Coated Piston on Combustion Chamber Deposit Accumulation

- The low thermal conductivity and diffusivity of the MgZr coating reduced CCD accumulation on the piston periphery compared to the baseline metal piston due to the elevated surface temperature of the MgZr coating.
  - The MgZr coating on the heat flux probe at location #2 provided a 65% reduction in CCD accumulation due to this effect.
- The surface roughness of the MgZr piston was speculated to interact with the DI fuel spray during bowl impingement, resulting in increased fuel pooling within the piston bowl and producing greater CCD accumulation in the MgZr bowl than in the aluminum piston bowl.
- CCD accumulation on the cylinder head was reduced during operation with the MgZr piston due to the altered fuel dynamics attributed to the surface roughness of the MgZr coating.
  - It was reasoned that increased fuel pooling in the MgZr piston bowl leaned the remaining charge, producing the reduced CCD accumulation on the cylinder head.

7.1.5 Impact of a Magnesium Zirconate Coated Piston on HCCI Operation

- Installation of the MgZr coated piston into a clean combustion chamber shifted the HCCI operability range to lower loads and accounted for much of the shift in operability created by fully conditioning a metal chamber.
- The shift in combustion phasing experienced during conditioning with the MgZr piston was 39% less than the shift experienced with an aluminum piston.

  - The rate of combustion phasing change due to CCD accumulation was reduced during operation with the MgZr piston, adding to the operational stability of a practical engine.
- The increase in burn duration beyond the impact of combustion phasing during MgZr piston operation further supported the hypothesis that porosity induced fuel pooling in the MgZr bowl produced charge stratification.

7.2 Summary of Contributions

This work has developed the methodology and evaluated the accuracy of an ex-situ technique for non-destructive diffusivity determination. The radiation chamber is especially useful when studying fragile coatings, like CCD, and flame sprayed ceramics, whose properties are a function of several application variables.

Fuel-morphology interactions do not have a significant impact on the thermal diffusivity of cylinder head CCD. Additionally, compressed air was eliminated as an influence on CCD diffusivity over the range of pressures and temperatures experienced during HCCI operation. These results imply that porosity does not have an influence beyond its impact on TBC thermal properties simplifying the selection of a TBC to act as a CCD surrogate.

CCD were found to have a partial transparency to radiation heat flux. This information is also useful in the selection of an adequate CCD surrogate as many TBC exhibit transparency to radiation.

The impact of the initially sparse CCD accumulation process was noted for the first time as all previous CCD diffusivity results were measured under the influence of in-situ convection heat transfer. In-situ convection did not penetrate through the gaps in CCD accumulation to the temperature measurement surface, so all previous results were oblivious to the sparse area coverage of the CCD. This sparse formation behavior led to significant insensitivity of the sub-CCD temperature phase delay to the ex-situ radiation pulse and created the nonlinear portion of the ex-situ phase delay versus CCD thickness trend. The fact that in-situ results are insensitive to the porosity and line-of-sight avenues within the CCD layer shows that radiation is not a significant heat transfer mechanism in HCCI combustion.

The radiation penetration factor was developed as a measure of the effective porosity of the CCD or coating in question. The factor is not a direct measure of porosity, but rather a measure of the total impact of the exposed pores. The radiation penetration factor can only be determined by comparing the response of the substance to radiation and convection heat transfer modes, and therefore, represents a newly-developed, unique capability.

Comparing the radiation penetration factors of prospective TBC to CCD will allow for a more intelligent TBC selection/design process. In addition, determination of the radiation penetration factor for substances of known porosity could calibrate this factor and result in absolute measurements of effective porosity for coatings.

Speculation surrounding the impact of MgZr surface roughness on fuel pooling and charge stratification implicated TBC surface roughness as an important design consideration. The charge stratification hypothesis was supported by the impact of the MgZr piston on CCD accumulation throughout the combustion chamber and the increase of HCCI burn duration beyond the influence of combustion phasing during MgZr piston operation. Therefore, it can be reasoned that the TBC surface roughness influenced both the final conditioned state of the chamber and the operational variability imposed by the conditioning process.

Overall, thermal barrier coatings were shown to provide a useful shift in the HCCI operating regime toward lower loads where the fuel economy benefit of HCCI over traditional spark ignition combustion is at a maximum. Additionally, the MgZr coated showed the potential of TBC to reduced the operational variability imposed by CCD accumulation.

7.3 Recommendations for Future Work

The thermal properties of CCD subjected to fuel wetting/pooling may be impacted by the fuel. Current diffusivity testing was conducted with CCD accumulated on the cylinder head, which were not directly wetted by fuel. Ex-situ testing with CCD wetted with fuel could shed insight into this potential behavior. Additionally, testing of CCD from the piston bowl could shed light on this potential effect.

The sparse nature of initial CCD accumulation can be quantified with a luminosity study. As CCD accumulate, in-situ and ex-situ diffusivity measurements should be taken in the manner described in this study. However, while removed from the chamber, the CCD covered probes could be bombarded by a light source of known intensity. The luminosity reflecting back from the steel temperature measurement surface through the CCD could then be quantified and compared to a clean baseline probe. The sparse CCD accumulation could thereby be represented as a spatial coverage area fraction. Additionally, this testing could quantify the line-of-sight penetration depth of various substances.

Further investigation into the impacts of TBC surface roughness on fuel pooling and subsequent charge stratification/leaning should be conducted. A piston with the MgZr coating applied only to the periphery should be subjected to a passive conditioning study. Comparing the subsequent CCD accumulation and operability ranges of that piston to the full coverage MgZr results of this work will verify the impact of the MgZr roughness on fuel pooling and charge stratification. Passive conditioning of the current MgZr piston with a fully premixed injection strategy could also provide a valuable comparison to isolate the impact of coating surface roughness on fuel pooling and charge stratification. Additionally, optical studies could be used to quantify the stratification of the fuel charge associated with pistons of different surface roughness.

Developing an ex-situ test for CCD and TBC conductivity will significantly improve the selection of an appropriate TBC to act as a CCD surrogate. Thermal conductivity has been shown to have a significant impact on the TBC surface temperature swing seen by the combustion gases [13]. In addition, the conductivity value could be used to pinpoint the porosity fraction of the coating through use of the Woodside correlation [93].

The penetration of ex-situ radiation into the CCD layer may pose a significant challenge to conductivity measurements as the hottest portion of the sample will be subsurface. Therefore, determining the CCD surface temperature optically by measuring the emitted radiation from the CCD sample could be complicated. If the line-of-sight pathways that allow radiation penetration into the sample also allow radiation to emit from within the depth of the sample, radiation penetration may have a significant impact on the infrared detection of material surface temperature.

BIBLIOGRAPHY

[1] Institute for the Analysis of Global Security, www.iags.org/futureofoil.html

[2] Wood, J.H., Long, G.R., and Morehouse, D.F., “Long-Term World Oil Supply Scenarios: The Future is Neither as Bleak or Rosy as Some Assert”, Energy Information Administration of the Department of Energy, April, 2003, http://www.netl.doe.gov/energy-analyses/pubs/EIA_LongTermOilSupply.pdf

[3] LaHood, R., and Jackson, L.P., “2017-2025 Model year Light-Duty Vehicle GHG Emissions and CAFÉ Standards: Supplemental Notice of Intent”, Environmental Protection Agency, National Highway Traffic Safety Administration, July 29, 2011

[4] Stanglmaier, R. H., Roberts, C. E., “Homogeneous Charge Compression Ignition (HCCI): Benefits, Compromises, and Future Engine Applications”, SAE 1999-01-3682, 1999.

[5] Olsson, J.-O., Tunestål, P., and Johansson, B., “Closed-Loop Control of an HCCI Engine”, SAE 2001-01-1031, 2001

[6] Yamamoto, S., Satou, T., and Ikuta, M., “Feasibility Study of Two-stage Hybrid Combustion in Gasoline Direct Injection Engines”, SAE 2002-01-0113, 2002

[7] Hiraya, K., Hasegawa, K., Urushihara, T., Iiyama, A., and Itoh, T., “A Study on Gasoline Fueled Compression Ignition Engine ~A Trial of Operation Region Expansion~”, SAE 2002-01-0416, 2002

[8] Najt, P., and Foster, D., “Compression Ignited Homogeneous Charge”, University of Wisconsin-Madison, SAE 830264, 1983

[9] Zheng, J., yang, W., Miller, D. L., and Cernansky, N. P., “A Skeletal Chemical Kinetic Model for the HCCI Combustion Process”, SAE 2002-01-0423, 2002

[10] Flowers, D., Aceves, S., Smith, R., Torres, J., Girard, J., and Dibble, R., "HCCI in a CFR Engine: Experiments and Detailed Kinetic Modeling", SAE 2000-01-0328, 2000

[11] Güralp, O., Hoffman, M., Assanis, D., Filipi, Z., Kuo, T.-W., Najt, P., Rask, R., "Thermal Characterization of Combustion Chamber Deposits on the HCCI Engine Piston and Cylinder Head Using Instantaneous Temperature Measurements", SAE 2009-01-0668, 2009.

[12] Güralp, O.A., Hoffman, M.A., Assanis, D., and Filipi, Z., "Characterizing the Effect of Combustion Chamber Deposits on a Gasoline HCCI Engine", SAE 2006-01-3277, 2006

[13] Güralp, O.A., "The Effect of Combustion Chamber Deposits on Heat Transfer and Combustion in a Homogeneous Charge Compression Ignition Engine", PhD Dissertation, University of Michigan Department of Mechanical Engineering, 2008

[14] Jacobs, T., Bohac, S., Assanis, D., and Szymkowicz, P., "Lean and Rich Premixed Compression Ignition Combustion in a Light-Duty Diesel", SAE 2005-01-0166, 2005

[15] Epping, K., Aceves, S., Bechtold, R., and Dec, J., "The Potential of HCCI Combustion for High Efficiency and Low Emissions", SAE 2002-01-1923, 2002

[16] Heywood, J.B., Internal Combustion Engine Fundamentals, McGraw-Hill, New York, 1988.

[17] Dec, J. E., Sjöberg, M., "Isolating the Effects of Fuel Chemistry on Combustion Phasing in an HCCI Engine and the Potential of Fuel Stratification for Ignition Control", SAE 2004-01-0557, 2004

[18] Onishi, S., Jo, S. H., Shoda, K., Jo, P. D., and kato, S., “Active Thermo-Atmosphere Combustion (ATAC) – A New Combustion Process for Internal Combustion Engine”, SAE 790501, 1979

[19] Glassman, I., Combustion, Third Edition, Academic Press, San Diego, 1996

[20] Aoyama, T., Hattori, Y., Mizuta, J., and Sato, Y., “An Experimental Study on Premixed-Charge Compression Ignition Gasoline Engine”, SAE 960081, 1996

[21] Ishibashi, Y., and Asai, M., “Improving the Exhaust Emissions of Two-Stroke Engines by Applying the Activated Radical Combustion”, SAE 960742, 1996

[22] Kimura, S., Aoki, O., Ogawa, H., Muranaka, S., and Enomoto, Y., “New Combustion Concept for Ultra-Clean and High-Efficiency Small DI Diesel Engines”, SAE 1999-01-3681, 1999

[23] Walter, B., and Gatellier, B., “Development of the High Power NADI Concept Using Dual Mode Diesel Combustion to Achieve Zero NO_x and Particulate Emissions”, SAE 2002-01-1744, 2002

[24] Eng, J.A., “Characterization of Pressure Waves in HCCI Combustion”, SAE 2002-01-2859, 2002

[25] Christensen, M., Johansson, B., “Influence of Mixture Quality on Homogeneous Charge Compression Ignition”, SAE 982454, 1998

[26] Kaneko, N., Ando, H., Ogawa, H., Miyamoto, N., “Expansion of the Operating Range With In-Cylinder Water Injection in a Premixed Charge Compression Ignition Engine”, SAE 2002-01-1743, 2002

[27] Allen, J., and Law, D., “Variable Valve Actuated Controlled Auto-Ignition: Speed Loads Maps and Strategic Regimes of Operation”, SAE 2002-01-0422, 2002

[28] Sjöberg, M., Dec, J. E., Cernansky, N. P., “Potential of Thermal Stratification and Combustion Retard for Reducing Pressure-Rise Rates in HCCI Engines, Based on Multi-Zone Modeling and Experiments”, SAE 2005-01-0113, 2005

[29] Krasselt, J., Foster, D., Ghandhi, J., Herold, R., Reuss, D., and Najt, P., “Investigations into the Effects of Thermal and Compositional Stratification on HCCI Combustion – Part I: Metal Engine Results”, SAE 2009-01-1105, 2009

[30] Herold, R. E., Krasselt, J. M., Foster, D. E., Ghandhi, J. B., Reuss, D. L., and Najt, P. M., “Investigations into the Effects of Thermal and Compositional Stratification on HCCI Combustion – Part II: Optical Engine Results”, SAE 2009-01-1106, 2009

[31] Martinez-Frias, J., Aceves, S. M., Flowers, D., Smith, J. R., and Dibble, R., “HCCI Engine Control by Thermal Management”, SAE 2000-01-2869, 2000

[32] Christensen, M., and Johansson, B., “Supercharged Homogeneous Charge Compression Ignition (HCCI) with Exhaust Gas Recirculation and Pilot Fuel”, SAE 2000-01-1835, 2000

[33] Milovanovic, N., Blundell, D., Pearson, R., Turner, J., and Chen, R., “Enlarging the Operational Range of a Gasoline HCCI Engine by Controlling the Coolant Temperature”, 2005-01-0157, 2005

[34] Christensen, M., Johansson, B., and Einewall, P., “Homogeneous Charge Compression Ignition (HCCI) Using Isooctane, Ethanol and Natural Gas – A Comparison with Spark Ignition Operation”, SAE 972874, 1998

[35] Dec, J.E., Hwang, W., and Sjöberg, M., “An Investigation of Thermal Stratification in HCCI Engines Using Chemiluminescence Imaging”, SAE 2006-01-1518, 2006

[36] Sjöberg, M., and Dec, J., “Combined Effects of Fuel-Type and Engine Speed on Intake Temperature Requirements and Completeness of Bulk-Gas Reactions for HCCI Combustion”, SAE 2003-01-3173, 2003

[37] Iida, M., Aroonsrisopon, T., Hayashi, M., Foster, D., and Martin, J., "The Effect of Intake Air Temperature, Compression Ratio, and Coolant Temperature on the Start of Heat Release in an HCCI Engine", SAE 2001-01-1889/4278, 2001

[38] Aroonsrisopon, T., Foster, D., Morikawa, T., and Iida, M., "Comparison of HCCI Operating Ranges for Combinations of Intake Temperature, Engine Speed and Fuel Composition", SAE 2002-01-1924, 2002

[39] Chang, J., Filipi, Z., Assanis, D., Kuo, T-W., Najt, P., and Rask, R., "Characterizing the Thermal Sensitivity of a Gasoline Homogeneous Charge Compression Ignition Engine With Measurements of Instantaneous Wall Temperature and Heat Flux", International Journal of Engine Research Vol 6, IMechE, 2005.

[40] Cheng, S., Kim, C., "Effect of Engine Operating Parameters on Engine Combustion Chamber Deposits." SAE 902108, 1990.

[41] Nakic, D.J., Assanis, D.N., White, R.A., "Effect of Elevated Piston Temperature on Combustion Chamber Deposit Growth," SAE 940948, 1994.

[42] Kalghatgi, G.T., McDonald. C.R., Hopwood, A.B., "An Experimental Study of Combustion Chamber Deposits and Their Effects in a Spark-Ignition Engine," SAE 950680, 1995.

[43] Ishii, H., Emi M., Yamada, Y., Kiruma, S., Shimano, K., and Enomoto, Y., "Heat Loss to the Combustion Chamber Wall with Deposit Adhering to the Wall Surface in DI Diesel Engine", SAE 2001-01-1811/4231

[44] LaVigne, P.A., Anderson, C.L., Prakash, C., "Unsteady heat Transfer and Fluid Flow in Porous Combustion Chamber Deposits," SAE 860241, 1986.

[45] Tree, D.R., Wiczynski, P.D., Yonushonis, T.M., "Experimental Results on the Effect of Piston Surface Roughness and Porosity on Diesel Engine Combustion," SAE 960036, 1996.

[46] Tree, D. R., Oren, D. C., Yonushonis, T. M., Wiczynski, P. D., “Experimental Measurements on the Effect of Insulated Pistons on Engine Performance and Heat Transfer”, SAE 960317, 1996.

[47] Dronniou, N., Dec, J., “Investigating the Development of Thermal Stratification from the Near-Wall Regions to the Bulk-Gas in an HCCI Engine with Planar Imaging Thermometry”, SAE 2012-01-1111, 2012

[48] Nishiwaki, K., Hafnan, M., “The Determination of Thermal Properties of Engine Combustion Chamber Deposits”, SAE 2000-01-1215

[49] Hopwood, A.B., Chynoweth, S., and Kalghatgi, G.T., “A Technique to Measure Thermal Diffusivity and Thickness of Combustion Chamber Deposits In-Situ”, SAE 982590

[50] Assanis, D.N., “The Effect of Thin Ceramic Coatings on Petrol Engine Performance and Emissions”, Int. Journal of Vehicle Design, vol. 13, no. 4, 1992, pages 378 – 387.

[51] Assanis, D., Wiese, K., “The Effects of Ceramic Coatings on Diesel Engine Performance and Exhaust Emissions,” SAE 910460, 1991.

[52] Kamo, R., Assanis, D.N., Bryzik, W., “Thin Thermal Barrier Coatings for Engines”, SAE 890143, 1989.

[53] Hultqvist, A., Christensen, M., Johnasson, B., “The Application of Ceramic and Catalytic Coatings to Reduce the Unburned Hydrocarbon Emission from a Homogeneous Charge Compression Ignition Engine”, SAE 2000-01-1833, 2000.

[54] Haenel, P., Kleeberg, H., Tomazic, and Dolan, S., “Investigation Regarding the Influence of a Catalytic Combustion Chamber Coating on Gasoline Combustion Characteristics, Emission Formation and Engine Efficiency”, SAE 2012-01-1097, 2012

[55] Taylor, R.E., Wang, X., Xu, X., “Thermophysical Properties of Thermal Barrier Coatings”, Surface and Coatings Technology 120-121 (1999) 89-95

[56] Parker, W.J., Jenkins, R.J., Butler, C.P., and Abbott, G.L., “Flash Method of Determining thermal Diffusivity, Heat Capacity, and Thermal Conductivity”, Journal of Applied Physics, Volume 32, Number 9, September, 1961.

[57] Taylor, R., “Construction of Apparatus for Heat Pulse Thermal Diffusivity Measurements from 300-3000K”, J. Phys. E: Sci. Instrum., Vol. 13, 1980.

[58] Cezairliyan, A., Baba, T., and Taylor, R., “A High-Temperature Laser-Pulse Thermal Diffusivity Apparatus”, International Journal of Thermophysics, Vol 15, No. 2, 1994.

[59] Kim, S.W., and Taylor, R.E., “Estimation of Thermophysical Properties of a Film Coated on a Substrate Using Pulsed Transient Analysis”, International Journal of Thermophysics, Vol. 14, No. 1, 1993.

[60] Hoffman, M.A., “Design and Implementation of a Dynamic Radiation Chamber to Determine Thermal Properties of HCCI CCD and Thermal Barrier Coatings”, MSE Dissertation, University of Michigan, 2008.

[61] Cahill, D.G., “Thermal Conductivity Measurement form 30 to 750 K: The 3ω Method”, Rev. Sci. Instrum., 61 (2), February 1990.

[62] Rosencwaig, A., Gersho, A., “Theory of the Photoacoustic Effect with Solids”, Journal of Applied Physics, Vol. 47, No. 1, January 1976.

[63] Antou, G., Hlawka, F., Cornet, A., Becker, C., Ruch, D., and Riche, A., “In Situ Laser Remelted Thermal Barrier Coatings: Thermophysical Properties”, Surface & Coatings Technology, 200 (2006) 6062-6072

[64] Zhang, J., and Desai, V., “Determining Thermal Conductivity of Plasma Sprayed TBC by Electrochemical Impedance Spectroscopy”, Surface & Coatings Technology, 190 (2005) 90-97.

[65] Lu, T.J., Levi, C.G., Wadley, H.N.G., and Evans, A.G., “Distributed Porosity as a Control Parameter for Oxide Thermal Barriers Made by Physical Vapor Deposition”, J. of Am. Ceram. Soc., 84 [12] 2937 – 46 (2001).

[66] Stevostianov, I., Kachanov, M., “Plasma-Sprayed Ceramic Coatings: Anisotropic Elastic and Conductive Properties in Relation to the Microstructure; Cross-Property Correlations”, Materials Science and Engineering, A297 (2001) 235-243.

[67] Sevostianov, I., Kachanov, M., “Anisotropic Thermal Conductivities of Plasma-Sprayed Thermal Barrier Coatings in Relation to the Microstructure”, Journal of Thermal Spray Technology, Volume 9(4), December, 2000.

[68] Chang, K., Babajimopoulos, A., Lavoie, G.A., Filipi, Z.S., Assanis, D.N., “Analysis of Load and Speed Transitions in an HCCI Engine Using 1-D Cycle Simulation and Thermal Networks”, SAE 2006-01-1087, 2006.

[69] Chang, J., “Thermal Characterization and Heat Transfer Study of a Gasoline Homogeneous Charge Compression Ignition Engine via Measurements of Instantaneous Wall Temperature and Heat Flux in the Combustion Chamber”, PhD Dissertation, 2004, University of Michigan Department of Mechanical Engineering

[70] Fox Thermal Instruments, Inc., 399 Reservation Road, Marina, CA 93933, http://www.foxthermalinstruments.com/pdf/ft2/FT2%20Datasheet.pdf

[71] ETAS Inc., 3021 Miller Road, Ann Arbor, MI 48103 http://www.etas.com/en/products/la4-technical_data.php

[72] Lee, C.S., “Characterization of a Single Cylinder Direct Injection Spark Ignition Engine and Comparison with Single Cylinder Port Fuel Injection SI Engine,” M.S. Thesis, University of Michigan, Ann Arbor, 2001

[73] Randolph, A. L., “Recommendation of Revised Corporate-Standard Equations for Exhaust Gas Analysis”, GM Research Report EN-506, Sept. 11, 1992

[74] Horiba Instruments Incorporated, 5900 Hines Drive, Ann Arbor, MI 48108, http://www.horiba.com/automotive-test-systems/products/emission-measurement-systems/analytical-systems/standard-emissions/details/mexa-7000-version-3-930/

[75] Medtherm Bulletin, Medtherm Corporation, Huntsville, Al, Bulletin 500.

[76] Fischer Technology, Inc, http://www.verniersales.com/Probe%20Catolog.pdf

[77] Kistler Instrument Corp., 75 John Glenn Drive, Amhearst, NY 14228, http://www.kistler.com/mediaaccess/65.204e-03.99.pdf

[78] Gatowski, J.A., Balles, E.N., Chun, K.M., Nelson, F.E., Ekchian, J.A., Heywood, J.B., “Heat Release Analysis of Engine Pressure Data,” SAE841359, 1984.

[79] Chang, J., Güralp, O., Filipi, Z., Assanis, D., Kuo, T., Najt, P., Rask, R., “New Heat Transfer Correlation for an HCCI Engine Derived from Measurements of Instantaneous Surface Heat Flux,” SAE 2004-01-2996, 2004

[80] The Temperature Handbook, Vol.29, Omega Engineering Inc, 1995

[81] Giberson, R.C., and Walker, J.P., "Reaction of Nuclear Graphite with Water Vapor - Part 1: Effect of Hydrogen and Water Vapor Partial Pressures", Battelle Northwest Report, BNSA-181, 1965

[82] Walker, P.L, Rusinko, F., and Austin, L.G., Advances in Catalysis, 11, 123 (1959)

[83] Goldstein, H., “The Reaction of Active Nitrogen with Graphite” Journal of Physical Chemistry, Vol 68, January, 1964

[84] McCaroll, B., McKee, D.W., “The reactivity of graphite surfaces with atoms and molecules of hydrogen, oxygen and nitrogen” Carbon, volume 9, Issue 3, May 1971

[85] Incropera, F., and DeWitt, D., Introduction to Heat Transfer, Fourth Edition, New York, John Wiley & Sons, 2002

[86] Jackson, N.S., Pilley, A.D., and Owen, O.J., "Instantaneous Heat Transfer in a Highly Rated DI Truck Engine", SAE 900692

[87] Gatowski, J., Smith, M., and Alkidas, A., "An Experimental Investigation of Surface Thermometry and Heat Flux", Experimental Thermal and Fluid Science, 1989, 2: 280-292

[88] Insaco Inc., 1365 Canary Road, PO Box 9006, Quakertown, PA 18951-9006 USA, (215) 536-3500

[89] Solidworks Education Edition (2010). SP5.0. COSMOS Material Properties Library

[90] Holman, J.P., (2002) *Heat Transfer* 9th Edition., McGraw-Hill

[91] Aerospace Specification Metals Inc. (2011). Al 6061-T6 (who in turn cites The Aluminum Association Inc. from Aluminum Standards and Data 2000)

[92] Fox, A.C., and Clyne, T.W., "Oxygen transport by gas permeation through the zirconia layer in plasma sprayed thermal barrier coatings", Surface and Coatings Technology 184, p 311-321, 2004

[93] Woodside, W., and Messmer, J.H. "Thermal Conductivity of Porous Media II. Consolidated Rocks", J. Appl. Phys. 32, 1699. 1961

[94] Shafiro, B., and Kachanov, M., "Anisotropic Effective Conductivity of Materials with Nonrandomly Oriented Inclusions of Diverse Ellipsoidal Shapes", J. Appl. Phys., 2000, 87(12) p8561-8569

[95] Clyne, T.W., Golosnoy, I.O., Tan, J.C. and Markaki, A.E., "Porous Materials for Thermal Management under Extreme Conditions", Phil. Trans. A Math. Phys. Eng. Sci., 2006, 364(1838), p125-146

[96] FUCHS LUBRITECH Heat Sink Silicone Compound, CHEMPLEX® 1381, Product#30018080020087, 17050 Lathrop Avenue, Harvey, Illinois 60426 http://xa.yimg.com/kq/groups/23188191/2021063673/name/thermal+grease-chpx1381.pdf

[97] Mendera, K., “Effectiveness of Plasma Sprayed Coatings for Engine Combustion Chamber”, SAE 2000-01-2982

[98] Merzlikin, V., Timonin, V., Gutierrez Ojeda, M., Sidorov, O., “New Selectively Absorbing and Scattering Heat-Insulating Coatings of the Combustion Chamber for Low-Heat-Rejection Diesel”, SAE 2007-01-1755

[99] Gutierrez Ojeda, M., Merzlikin, V., Sidorov, O., Kalenkov, S., “Regulation of the Combustion Chamber Walls Temperature with Semitransparent Heat Insulating Coatings”, SAE 2007-24-0031

[100] Asbury Carbons, Dry Graphite Aerosol Spray Lubricant, Lubricant & Specialty Products Group, P.O. Box 144, 405 Old Main Street, Asbury, NJ 08802, www.asbury.com

[101] Golosnoy, I. O., Cipitria, A., and Clyne, T. W., “Heat Transfer Through Plasma-Sprayed Thermal Barrier Coatings in Gas Turbines: A Review of Recent Work”, Journal of Thermal Spray Technology, Vol. 18 (5-6) 2009 pp. 809 - 821

[102] Akopov, F. A., Val’yano, G.E., Vorob’ev, A. Yu., Mineev, V. N., Petrov, V. A., Chernyshev, A. P., and Chernyshev, G. P., “Thermal Radiative Properties of Ceramic of Cubic ZrO_2 Stabilized with Y_2O_3 at High Temperatures”, High Temperature, Vol, 39, No. 2, 2001, pp. 244-254

[103] Rätzer-Scheibe, H., and Schulz, U., “The effects of heat treatment and gas atmosphere on the thermal conductivity of APS and EB-PVD PYSZ thermal barrier coatings”, Surface & Coatings Technology, 201, 7880-7888, 2007

[104] Perry. Chemical Engineer’s Handbook: 7th Edition, Table 2-229

[105] Dronniou, N., and Dec, J., “Investigating the Development of Thermal Stratification from the Near-Wall Regions to the Bulk Gas in an HCCI Engine with Planar Imaging Thermometry”, SAE 2012-01-1111

[106] Funk, C., Sick, V., Reuss, D., Dahm, W., “Turbulence Properties of High and Low Swirl In-Cylinder Flows”, SAE 2002-01-2841

[107] Manara, J., Arduini-Schuster, Ratzer-Scheibe, and Schulz, U., “Infrared-optical properties and heat transfer coefficients of semitransparent thermal barrier coatings”, Surface & Coatings Technology 203 (2009) 159-1068

[108] Kakuda, T. R., Limarga, A. M., Bennett, T. D., and Clarke, D. R., “Evolution of thermal properties of EB-PVD 7YSZ thermal barrier coatings with thermal cycling”, Acta Materialia (2009) 2583-2591

[109] Zhu, D., and Miller, R. A., “Sintering and creep behavior of plasma-sprayed zirconia and hafnia-based thermal barrier coatings”, Surface and Coatings Technology 108-109 (1998) 114-120

[110] Flame Spray Coating Co., 33847 Doreka Drive, Fraser, MI 48026

[111] Jefferson, T. B., Witzell, O. W., and Sibbitt, W. L., “Thermal Conductivity of Graphite-Silicone Oil and Graphite-Water Suspensions”, Industrial and Engineering chemistry, Vol. 50, No. 10, 1958

[112] Agari, Y., Ueda, A., and Nagai, S., “Thermal Conductivities of Composites in Several Types of Dispersion Systems”, Journal of Applied Polymer Science, Vol. 42, pp. 1665–1669, 1991

[113] Campbell, S., Lin, S., Jansons, M., and Rhee, K. T., “In-cylinder Liquid Fuel Layers, Cause Unburned Hydrocarbon and Deposit Formation in SI Engines?”, SAE paper 1999-01-3579

[114] Li, J., “Metal Surface Effects on Deposit Formation from Thermally Stressed Jet Fuels and Model Compounds”, PhD Thesis, Pennsylvania State University Department of Materials Science and Engineering, 1998

[115] Cheng, S., “A Physical Mechanism for Deposit Formation in a Combustion Chamber”, SAE paper 941892, 1994